Fully high temperature superconducting (HTS) machine for future electric aircraft

PhD Thesis

Fangjing Weng

Applied Superconductivity Group
Institute for Energy and Environment
Department of Electronic and Electrical Engineering
University of Strathclyde, Glasgow

Sep 1st, 2021

This thesis is the result of the author's original research. It has been composed by the author and has not been previously submitted for examination which has led to the award of a degree.

Signed: Fangjing Weng

Date: 06/09/2021

Acknowledgements

First, I wish to honestly acknowledge my supervisor, Dr Min Zhang, who has provided me with valuable guidance in every research stage and Prof Weijia Yuan for academic support during my PhD.

I would like to thank Prof Graeme Burt, Richard Munro, George Cochrane. I truly appreciate the great work environment they constitute and provide expert technical support throughout my PhD.

I am grateful to all members in applied superconductivity group, especially Dr Yawei Wang, Dr Jie Sheng, Dr Muhammad Zulfiqar Ali and Tian Lan for their continuous support throughout my PhD.

I would like to thank all my friends for their companionship and encouragement.

I would also like to thank the Chinese Scholarship Council for covering my fees during my research. (File No.201908060381)

Last but not least, I especially would like to thank my dear parents for their support and encouragement over the years.

Publication during PhD

1. Weng, F., Zhang, M., Lan, T., Wang, Y., & Yuan, W. (2020). Fully superconducting machine for electric aircraft propulsion: study of AC loss for HTS stator. *Superconductor Science and Technology*.
2. Wang, Y., Weng, F., Li, J., Šouc, J., Gömöry, F., Zou, S., ... & Yuan, W. (2020). No-insulation high temperature superconductor winding technique for electrical aircraft propulsion. *IEEE Transactions on Transportation Electrification*.
3. Weng, F., Zhang, M., Elwakeel, A., Lan, T., Mcneill, N., and Yuan, W. (2021) Transient test and AC loss study of a cryogenic propulsion unit for all electric aircraft. *IEEE Access*.

Paper draft finished, ready to submit to *Superconductor Science and Technology*:

1. Weng, F. Zhang, M., Lan, T., and Yuan, W. Study of multi-filament HTS coil for fully superconducting machine.

Abstract

Because of zero resistance and diamagnetism, superconductors were more than just perfect conductors comparing to conventional conductors. Superconductors have an excellent potential for power applications use; one of the exciting areas is the superconducting machine. After hundreds of years of development, the superconducting machine's researches entered into a new era since high-temperature superconductors' discoveries in 1986. Many pioneering works have been done by researchers worldwide. They would push the high-temperature superconducting machine in commercial use for future aircraft, offshore wind generator and all-electric ship propulsion.

For high power applications, superconductors can provide significantly higher current density compared to copper. The superconducting machine's design is more efficient and has potential use in MW-class wind turbines and future electrified aircraft. Furthermore, since 1986 when HTS were discovered, much progress has been made towards making the HTS applications economically feasible due to critical temperature above 77 K. The cost of cryogenic systems significantly decreased by using liquid nitrogen.

In this thesis, the work focus on pushing the HTS machine towards commercialisation use in power applications by focussing on AC loss studies on both rotor and stator of an HTS machine. In an AC machine design, AC loss's Joule heat needs to be accurately identified and minimised. Which can improve the stability of the machine, and also reduce the cost of the cryogenic system.

On the other hand, In rotating electrical machines, AC loss is unavoidable. We must identify the AC losses in both the rotor and stator part, which are the crucial parts in future large-scale machine design.

To this end, in this thesis, the contribution of original new works includes:

1. Developing, validating a 10 kW fully superconducting machine prototype platform to provide a machine environment to measure AC losses of HTS windings.

2. Calorimetrically quantify the electrical HTS stator and provided data for cutting edge AC loss reduction technologies.

3. Characterisation of NI superconducting coils in the machine rotor parts design.

4. More superconducting machine design considering power electronics.

Contents

List of Figures

List of Tables

Glossary of Abbreviations

1G	First Generation HTS
2G	Second Generation HTS
B	Magnetic Flux Density
Bi-2223	$Bi_2Sr_2Ca_2Cu_3O_x$ high temperature superconductor
BSCOO	Bismuth strontium calcium copper oxide superconductor
CC	Coated Conductor
DAQ	Data Acquisition
DPC	Double pancake coil
F	Flow Rate
FEM	Finite element method
GdBCO	$GdBa_2Cu_3O_{7-x}$ high temperature superconductor
L	Inductance
LBCO	Lanthanum Barium Copper Oxide
LHE	Liquid Helium
LN_2	Liquid Nitrogen
I_c	Critical Current
J_c	Current density
LTS	Low-temperature superconductors

H	Magnetic field
HTS	High-temperature superconductors
MMF	Magnetomotive Force
NbTi	Niobium–titanium
NI coil	No-insulation coil
NdFeB	Neodymium Iron Boron Magnets
p	Machine pole pair number
PM	Permanent Magnet
PMSM	Permanent Magnet Synchronous Machine
OCV	Open-circuit Voltage
R	Resistance
SC	Superconductor
SLPM	Standard Litres per Minutes
SM	Synchronous machine
SPC	Single pancake coil
V	Voltage
YBCO	Yttrium barium copper oxide ($YBa_2Cu_3O_{7-x}$)

Chapter 1 Introduction

In 1911, the field of superconductivity began with the discovery of Dutch physicist Heike Kamerlingh Onnes from the University of Leiden. He discovered that the resistance of mercury became zero at 4.2 K in liquid helium. He reported that "*Mercury has passed into a new state, which on account of its extraordinary electrical properties may be called the superconductive state.*" The phenomenon became known as superconductivity. In 1933, German physicists Walther Meissner and Robert Ochsenfeld discovered this phenomenon. They measured the magnetic field distribution outside superconducting tin and lead samples. In the presence of an applied magnetic field, the samples were cooled below their superconducting transition temperature, after which the samples cancelled nearly all interior magnetic fields.

Because of zero resistance and diamagnetism, superconductors were more than just perfect conductors and provided a uniquely defining property of the superconductor state. After hundreds of years of development, superconductivity becomes one of the most exciting areas. Many pioneering works have been done by researchers worldwide and would push superconductivity in commercial use.

1.1 Background

1.1.1 History of superconductivity

Superconductivity began with the discovery by Heike Kamerlingh Onnes in 1911 that mercury had zero electrical resistance at the temperature 4.2 K. Zero resistance which could be applied in the field of power transmission with no losses, or in large magnetic fields, or storage of energy. These applications were not quickly realised because the superconductors become conventional conductors at critical current density or at the critical field. In 1916, Silsbee hypothesised [1] that the critical current for a superconducting wire was equal to that current, which gave the critical field at the wire's surface, which is also called the Silsbee effect. The reason for this behaviour was not made clear until the discovery of the Meissner effect in 1933 [2].

From the 1950s to 1960s, superconductors can operate at higher currents and higher magnetic fields, pushing superconducting magnets to commercial use. These superconductors exhibit two critical fields designated H_{C1} and H_{C2}, which are called type-II superconductors. In 1950, another scientist Emanuel Maxwell discovered the isotope effect [3], which was also independently found by C. Reynolds et al. [4]. These experimental results are essential to explain the mechanism of superconductivity theoretically. The attractive coupling between electrons is through the lattice vibrations (i.e., phonon-mediated).

Until 1986, the highest critical temperature recorded for superconductors was only 23 K. This means liquid helium (4.2 K) had to be used for cooling. It is too expensive and unreliable for commercial use. Consequently, many potential applications were not commercially viable. Thus, scientists had to discover superconductors with higher critical temperatures. All this suddenly changed with the discovery of high-temperature superconductivity (HTS).

In April 1986, Scientists Bednorz and Müller, working at IBM in Zurich, published a paper that indicated the possible existence of superconductivity in a ceramic material: LBCO (Lanthanum Barium Copper Oxide) [5] with a critical temperature of 30 K and shared the 1987 Nobel Prize in physics. La-Ba-Cu-O was the first high temperature superconductor (HTS). Superconductivity in oxides had been known for many years. The discovery resulted from several years of extensive investigations on metal oxides superconducting. The La-Ba-Cu-O system was firstly founded by French scientists [6]. However, the French scientists were not looking for its superconductivity. In 1987, researchers in the University of Tokyo [7] confirmed Müller and Bednorz's findings, which means superconductivity is developing to the era of HTS. The synthesis of rare-earth metal oxides of increasingly higher critical temperature.

Following Bednorz and Müller's work, in 1987, culminating with the Y-Ba-Cu-O (YBCO) discovery was founded by Maw-Kuen Wu et al. with a critical temperature of 93 K [8]. This was a significant breakthrough as the material was superconducting in LN_2 at 77 K. Nitrogen is much cheaper and more abundant than helium. Also, the latent heat of liquid nitrogen is much higher than liquid helium. Thus, liquid nitrogen refrigeration systems are less complicated and much cheaper than systems using liquid helium.

1.1.2 Road map of superconducting machine

Due to significantly higher power density and efficiency than traditional copper-based motors, some superconducting machines have been developed by many research institutions worldwide. Many research institutions have successfully developed some significant machine testing rig or HTS machine prototypes. For the full-size MW-class machine for commercial use, the research progress is slow due to two primary factors: cost and stability. Currently, the HTS tape is still quite expensive for commercial use. Although liquid nitrogen is cheap and can be used for HTS coil testing, the operating temperature usually is below 77 K for commercial use, and cryogenic systems are still costly if the operating temperature is below 77 K. The other factor is stability, HTS material is a ceramic material and very fragile and easy to damage with either coil quench or mechanical shock, therefore, whilst in commercial use, the operating environment is usually complex compared to the lab environment. Thus the progress is slow, and a lack of experience for HTS machines' commercial use. To use HTS machines in engineering, more research is needed to assess future HTS systems' viability [9, 10].

MW-class partial HTS machines with an HTS rotor and a copper stator are estimated to reach 99% efficiency with most stator windings losses, almost 2% higher than a conventional generator of the same rating [9]. Further on, winding losses can be reduced by using the HTS coils in the stator. Fully superconducting machines could achieve very high efficiency by significantly reduce the coil losses in both the rotor and stator windings (>99.5%). Meanwhile, the fully HTS machines also have the potential to increase power density by increasing current density in the stator as well as increasing the magnetic loading in the rotor.

Table 1.1 demonstrates some past superconducting machine demonstrations developed by a variety of research institutes.

Table 1.1. List of notable past superconducting machine demonstrations

Year to reach	Developer	Speed (rpm)	Power rate (kVA)	Conductor type	Cryogenic	Machine characteristic	Efficiency (%)
1978	GE [11]	3600	20 000	NbTi	LHE	Large-turbine generator	99.3
1978	Westinghouse [12]	3600	300 000	NbTi	LHE	The world's first commercial LTS superconducting generator	99.4
1980	GE [13]	7000	20 000	NbTi & Nb3Sn	LHE	High speed generator for airborne	99.5
1987	GE (Alstom) [14]	3000	18	NbTi	LHE	first connected to a industrial grid	
1997	Super-GM (Japan) [15]	3600	78 700	NbTi	LHE	Highest output obtained in 1999	
2001	AMSC [16]	1800	3 725	BSCCO	Neon boil-off	1G HTS machine for inductrial	97.7
2004	Siemens [17, 18]	3600	4 000	1G HTS	Ne-Thermosiphon	Low-speed high-torque HTS machine	98.7
2007	AMSC [19]	120	36 500	unknown	Gaseous He	A famous HTS machine for US NAVY	
2008	GE [20]	10 000	1 300	BSCCO	Neon boil-off	1.3 MW at over 10 000 rpm	98
2020	Kalsi GPS [21]	10	10 000	MgB2	Gaseous He	Bi-2223 in rotor and MgB_2 in stator	98

According to Table 1.1, the world's first commercial superconducting generator was built by Westinghouse in 1978 [12], the LTS material was used to improve the performance of Large-turbine generators. At the same time, some other similar machines were also developed by GE [11] [13], Super-GM (Japan) tested a 70 MVA generator during the 1990s with three different LTS NbTi rotor windings. This is the highest output value obtained at that time [15]. The discovery of HTS in 1986 has the potential to push superconducting machines to lower-cost. The operating temperature of HTS conductors are much higher (between 25 K and 77 K) than LTS (normally 4.2 K), thus the refrigeration-cooling systems are much simplified than the LTS system design, also, another advantage is that the operating temperature range of HTS winding is much wider. As shown in Table 1.1, many full-scale commercial use machines, both low-speed and high-speed, have already been demonstrated using superconducting technology [9].

Many HTS machines have been developed (or developing) using the following configurations, as shown in Table 1.2 [9].

Table 1.2. A range of applications by using superconducting machine

Speed level	Power (MW)	Rotational speed (RPM)	Application
Ultra-low	10 - 15	10 - 15	Wind generator
Low	1 - 36.5	100 - 250	Navy
Medium	1 - 10	1800 – 3600	Industrial
High	1 - 50	7k – 30 k	Aerospace

Currently, some research goals for the commercial use of HTS machines has been achieved. However, further progress is still needed in these aspects:

- Kilometre-level HTS tape length usage
- AC losses reduction technology
- Improving the Ic characteristics in higher operating temperature
- Improving the HTS performance in the complex magnetic field environment
- Coil quench detection and protection
- Reduce the cost in HTS material and the cryogenic systems
- Improve the mechanical behaviour of the HTS coils
- Improve the machine’s structure in engineering

For the following decades, more research in engineering will push the HTS machine in large-scale power to reduce product cost. Larger markets can help reduce the cost of HTS material and cryogenic systems.

1.1.3 Road map of future electrified aircraft

According to IATA’s goals from “Aircraft Technology Roadmap to 2050” [22], new aircraft must be configured to reduce fuel burn and carbon dioxides emissions. For instance, more lean-burn engine technologies, more bio content fuels, and electric propulsion aircraft. Although electricity is not emissions-free now, it can be expected that life-cycle carbon emissions are going down considerably. The electricity can be generated by clean energy to reduce the emissions further. Table 1.3 shows that many aircraft manufacturers with many electric equipment providers focus on electric technologies to provide onboard energy consumption. The electric propulsion concepts are very suitable for application in distributed propulsion architectures. The electric propulsion for aircraft is a revolutionary step in the aviation industry.

Table 1.3. List of electric propulsion projects

Project name	Type	Passengers	Electrical Power	Fuel burn reduction
NASA N3-X [23]	Turboelectric	300	30 MW	Up to 70%
NASA STARC-ABL [24]	Partially turboelectric	154	2-3 MW	7-12%
BOEING SUGAR Freeze [25]	Parallel turboelectric (fuel cell)	154	50 MW	>70%
AIRBUS E-FAN X [26]	Hybrid series	100	4*2MW	

According to different design concepts, the topologies can be mainly described in 6 categories, as Figure 1.1 shows [22].

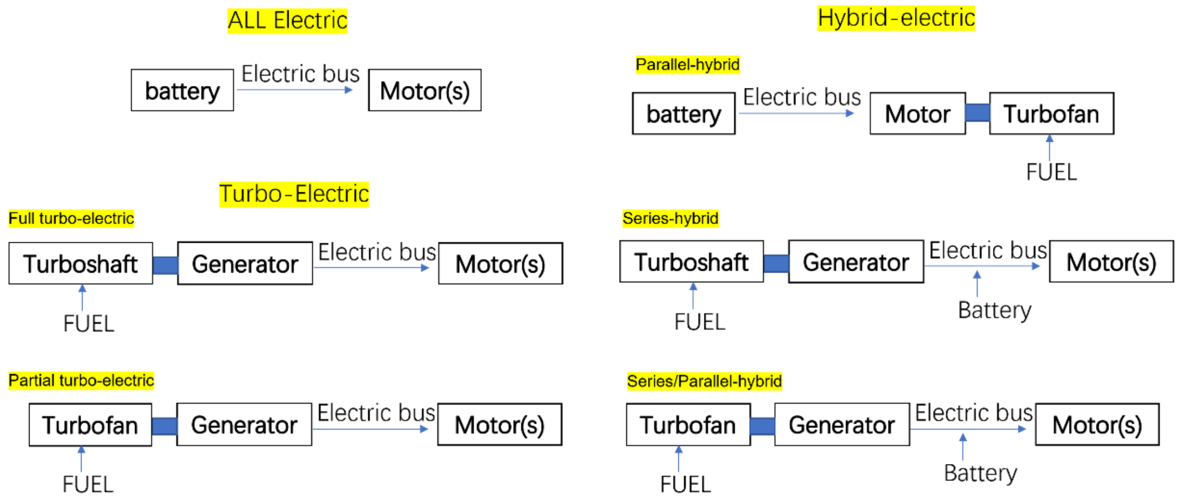

Figure 1.1 Electric propulsion architectures

- ***All-electric systems*** refer to using batteries as the only propulsive source onboard.

- ***Hybrid-electric systems*** refer to using gas turbine engines for propulsion and battery charging, and the batteries also provide the energy needed for propulsion at some stage.
  - Parallel-hybrid: turbine engine and a battery-powered motor are both mounted on a shaft that drives a fan.
  - Series-hybrid: only the electric motors are connected to the fans mechanically. The gas turbine is to drive an electric generator to provide energy. Systems are compatible with distributed propulsion that use multiple propulsion units.
  - Series/Parallel partial hybrid: some fans are driven directly by a gas turbine while electric motors drive other fans. They are using the turbine-driven generator or batteries to drive these motors.
- ***Turbo-electric systems*** use gas turbines as a propulsive power source rather than batteries.
  - Full turbo-electric: turboshaft engines drive electric generators that power inverters and individual DC motors, driving the individual distributed electric fans.
  - Partial turbo-electric: use electric propulsion to provide some of the propulsive power, and the rest is generated by a turbofan driven by a gas turbine.

1.1.4 Why fully superconducting machine for electric aircraft

For electric aircraft applications, NASA has proposed a distributed propulsion concept, which is claimed can reduce fuel burn to 70% [23, 27, 28]. NASA's concept is challenging and requires advanced technology in motors, generators, power cables and energy storage systems. The conventional copper-based machine cannot reach the requirement of the flight-weight machine. It is obviously that superconducting machines hold potential for the extreme reduction in machine size and weight. [9]. Thus, two large superconducting turbogenerators are set at the wing-tip from NASA's design concept and use 15 superconducting motor-driven to provide thrust. The parameters of generators and motors are illustrated in Table 1.4.

Table 1.4 Electrical machine requirement for turboelectric-aircraft design concept [27]

	HTS generators	HTS motors
Number of units	2	15
Power level	22.4 MW (30000 hp)	3 MW (4000 hp)
Weight	1000 Kg	236 Kg
Efficiency (active material)	99.3 %	99 %
Power density	22.4 kW/kg	12.7 kW/kg
Speed (RPM)	6500	4500

The power density of current electrical machines is not high enough for advanced propulsion applications in all-electric aircraft [23, 28-38]. Compared to conventional machines with copper windings, superconducting machines can significantly reduce machine volume and weight. Thus power density can be significantly increased. The latest HTS have high critical currents at relatively high operational temperatures, which can significantly increase the machine power density. Partially HTS machines based on HTS rotors and copper stators have been developed [39, 40]. However, the cold-rotor-warm-stator design previously led to large air gaps, therefore reducing the magnetic field. To fully utilize the advantages of HTS windings, fully HTS machines have been proposed to maximize machine power density for applications [36, 41, 42].

The aerospace sector is actively pursuing revolutionary design concepts toward electric aircraft to further reduce the environmental impact of air travel [30, 32, 43]. Aggressive targets have been set by both the EU and the US to cut aviation emissions [44, 45]. These regulations are the key drivers for aviation manufacturers to design more efficient electric aircraft. Some small electrical aircraft for several passengers have been developed successfully, in which batteries and machines with copper windings are applied. This kind of design is not suitable for future electrical aircraft with more than 100 passengers, due to the low energy density of present battery technology. Then, a more practical hybrid electrical propulsion design is proposed, in which fuel turbines are used to drive generators, power from generators is delivered to several electrical motors, and thus, a distributed electrical propulsion is achieved. This electrical aircraft propulsion design needs a generator/motor with very high power density, which is hard to be achieved by conventional machines with copper windings [46-49]. The latest second-generation high-temperature superconductor (2G HTS) (RE)Ba2Cu3Ox (REBCO) offers a transformative opportunity to develop electrical machines with high power densities because of their current-carrying capability is more than 20 times that of copper [50]. HTS machines have been developed for wind generator, ship propulsion, and energy storage successfully, which show great advantages on high power density, compact structure, and lightweight and thus is a promising candidate for future electrical aircraft propulsion [51].

Therefore, high power density machines at MW-class are needed for future all-electric aircraft. The design of a conventional non-cryogenic motor is 13.2 kW/kg and has 96% efficiency [52]. The HTS machine has a higher power density and higher efficiency due to zero resistance in DC operation. Currently, the majority of HTS machines are designed based on conventional topologies, replacing copper-based windings with superconductor materials. A partially superconducting machine with an HTS rotor and copper-based stator can reach an efficiency of 99%, and most power dissipation is in the conventional copper-based stator windings. A fully superconducting machine using HTS windings in both rotor and stator and have the potential to reach the highest efficiency, as the power dissipation is minimizing in both rotor and stator, the power density can be more than 20 kW/kg [9].

1.2 State-of-art and Motivation

1.2.1 Superconducting machine state-of-art

Consider a synchronous machine due to its high efficiency compared to an induction machine. HTS coils can be used in both stator windings and rotor windings to push the electrical machine toward the high-power density application. As for stator windings, the HTS coils can significantly increase the operating current to increase current density. For rotor windings, HTS coils can considerably reduce the rotor size and weight due to removing the iron core compared with the copper coil or the permanent magnet. The non-iron material's saturation no longer limits the magnetic field strength in the machine air gap. Thus, the strength of the magnetic field can be higher than 1.5 T [9].

- Partially superconducting machine

The partially superconducting machine refers to when replacing the rotor windings with superconducting windings, the armature windings are still conventional copper-based windings. Many industries and research institutes have made good progress as superconducting windings only applied on rotors, the transport current is DC, and the background field is stationary relative to the rotor in the synchronous machine. The partially superconducting machine can achieve a very high power density (99%); however, most power dissipation is in the copper armature windings. HTS windings must be used in stator windings to achieve an even higher power density, and fully superconducting machines need to be developed for future power applications.

- Fully superconducting machine

When superconducting windings are used for both stator and rotor windings, the machine is a fully superconducting machine. The air-cored machine was considered due to no saturation for magnetic flux density in the air. A fully superconducting machine has the potential to attain the highest efficiency as the superconducting windings can minimize the power dissipation in both rotor and stator. However, the stator windings operate in an AC magnetic field and carry AC current. Both magnetisation loss and transport loss exist in the stator windings. In this case, these losses must be evaluated appropriately in machine design.

The development of the superconducting machine is demonstrated in Chapter 1.1.2.

Superconducting windings can be designed with either LTS field windings (NbTi, Nb3Sn, etc.) or HTS field windings (BSCOO, ReBCO). Various standard machine topologies can be used for superconducting machine design: wound-field-synchronous machine, PM synchronous machine, HTS bulk magnet machine, etc. For synchronous machines, topologies can be either axial-flux or radial flux.

Many research institutes develop HTS superconducting windings worldwide due to the benefits of higher operating temperature (e.g. LN_2 temperature). Because HTS coated conductors are difficult to bend or twist, the coils are typically designed as racetrack coils, as shown in Figure 1.2.

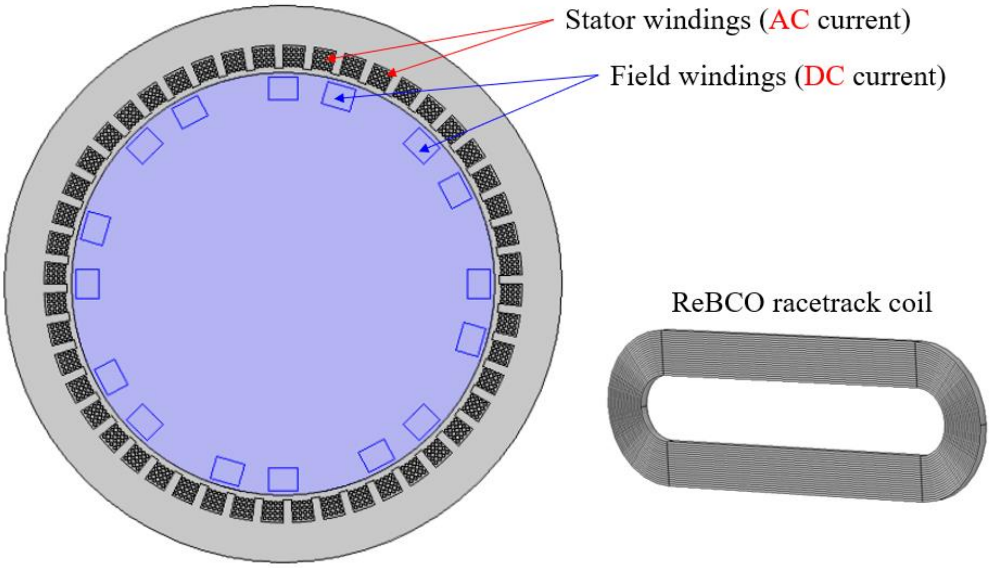

Figure 1.2. Schematic drawing of a fully HTS machine and racetrack coil.

Figure 1.2 demonstrates the winding configuration of a fully HTS machine. Field windings are used to generate the DC magnetic field of the rotor, the current density of HTS coils are significantly higher than conventional copper-based windings. The strength of the magnetic field can be higher than 1.5 T, and the weight can be reduced considerably by removing the iron core of the rotor. Stator windings can consist of HTS racetrack coils to reduce armature's Ohmic losses. In total, the HTS machine can increase the power density above 20 kW/kg (active material only) and increase the machine efficiency above 99.5%. For future electrified aircraft, superconducting machines (generators and motors) up to MW-class are needed to meet high-density and efficiency requirements.

When HTS windings carry a DC current under its critical current and operate below the critical temperature and the critical magnetic field, the AC loss is virtually zero. However, AC losses exist in HTS windings when carrying an AC current or operated in an AC magnetic background field. In machine applications, stator windings carry

AC current and also operate in a rotational magnetic field, in this case, AC loss is a crucial issue in machine design. The joule heat was produced in stator windings and cause the temperature to arise in the stator, and this heat must be fully considered in the cryogenic system. Otherwise, the stator coil has the potential to quench or even damage due to joule heat accumulation. As for the rotor in the synchronous machine, the rotor windings carry a DC current. The rotor speed is synchronous with the speed of the fundamental field generated by stator windings, and the HTS rotor is stationary relative to the fundamental field. However, there are higher-order ripple magnetic fields in the machine environment besides the fundamental field, and the ripple fields are not synchronous to the rotor windings; in this case, AC loss also exists in the rotor windings and the joule heat must be fully considered in machine design. The AC losses, including magnetisation loss, transport loss and total loss, need to be appropriately evaluated and quantified in both stator and rotor in machine design.

1.2.2 Fully superconducting machine design challenges

In a fully superconducting machine, both rotor winding and stator winding are using superconducting materials. Thus, fully superconducting machines are expected to reach a higher efficiency than partially superconducting machines because armature power loss is reduced compared with copper windings. In theory, the ohmic losses are significantly reduced in the stator. However, armature windings are carrying an AC current, and operating in an AC magnetic field. In this case, both transport loss and magnetisation loss exist in HTS armature windings. The AC losses in armature windings is a critical challenge in fully superconducting machine design. Due to the heavy cooling penalty in cryogenic temperature, an HTS wire with lower AC losses must be applied in fully HTS armature windings; otherwise, the size and weight of the cooling system will not be acceptable. Currently, there are no wire technologies available to achieve the feasibility and effectiveness of the HTS stator for commercial use. Some wire concepts, e.g., ROEBEL cable [53] and CORC® cable [54], have been studied by many researchers on feasibility and effectiveness for small-scale applications. The wire technologies for commercial use are not be proven yet [9].

Another critical issue in fully superconducting machine design is the rotor's stability. Typically the insulated coils are applied in the rotor of a superconducting machine. As the rotor is a rotational component, unavoidable mechanical vibration occurs when the rotor rotates, and also, the cryogenic systems for rotating parts are usually complicated. Therefore, when the superconducting coil on the rotor is quenched due to mechanical shock or the lack of cooling power, the coil is very easy to be damaged. In high-field magnets applications, this issue can be solved by applying a no-insulation coil (NI coil). NI coil has excellent mechanical robustness and thermal stability due to the removal of the turn-to-turn insulation field [55-67]. In the case of quench, the current can bypass the quenching point in the NI coil. However, the application of the NI coil on the HTS rotor has not been studied yet. The key challenge is that the electromagnetic environment in a machine is complex. The AC ripple magnetic field will cause magnetisation loss in the NI coil, and the magnetisation loss needs to be appropriately evaluated and quantified in the machine rotor's design.

To sum up, efficiency is an essential parameter in high power density HTS machine design. For HTS coils in the machine, AC losses are critical issues in engineering. Firstly, AC losses provided data for cryogenic systems design, and the cooling power needs to be matched with the machine. Secondly, both magnetisation AC loss and total AC loss need to be identified separately to evaluate the different HTS materials or coil structures properly. These data are essential in large-scale machine design. Finally, high AC losses may cause unavoidable heat inside the coil, cause the temperature to rise over HTS tape's critical temperature, and eventually cause the HTS coil to quench in the weak point or even be damaged totally. Thus, in machine design, a minimised AC loss design need to be considered.

A new HTS machine platform needs to be developed to measure AC losses of the stator windings. This platform provided the AC loss values of the HTS stator coil in a rotational magnetic field machine environment. By using the calorimetric method, both magnetisation AC loss and total AC loss can be identified and measured in this machine.

Then a coil model for the wound rotor design needs to be developed. For conventional electric machines, the air-gap magnetic field is limited by the iron core saturation on the rotor. The following solutions can achieve the higher air-gap magnetic field strength in the machine: increase the field current, and iron core must be removed in the rotor. This act can also significantly reduce machine size and weight. Due to the copper's current density limit, conventional copper-based rotor windings can not reach an appropriate air-gap field without the iron core. However, HTS made it possible to generate a significantly higher air-gap magnetic field without an iron core and only use a small volume of rotor field windings. The DC windings model needs to be developed and validated by experiments, to prove the HTS rotor's design.

The following research stage will carry on AC loss reduction technology to minimise the AC loss in an HTS machine, significantly reducing the cooling systems' cost and increasing machine efficiency. Finally, the fully HTS machine connects with cryogenic power electronics to identify how power electronics influence the coil AC loss.

1.3 The layout of the thesis

Chapter 1 introduces superconductivity and its history. Then introduces the development of superconducting machine and how it works on future electrified aircraft. Also, this part presents the motivation for the whole project.

Chapter 2 explains the fundamental theories of superconductivity. This chapter demonstrates the understanding of different types of superconductors, critical temperature, critical current, and AC loss theory. This chapter also presents the measurement methods for AC losses and the introduction of winding technologies, namely, insulated HTS coils and NI HTS coils.

Chapter 3 introduces the testing platform's design concepts, including the machine setup, calibration, and systems validation. This part presents an axial-flux fully superconducting machine that provides a rotational magnetic field using the calorimetric method. This system can measure either magnetisation AC loss and total loss for a 2G HTS stator coil in a rotational magnetic field. These results offer much data for large-scale superconducting machine design and provide a platform for different types of HTS coils to act further AC loss reduction research.

Chapter 4 presents the circuit network model of the rotor's design using NI coils and how NI coils perform in AC magnetic field environments. This part presents the simulation and experimental results of an NI coil in a background ripple magnetic field, and these results indicated the rotor part performance in a machine environment.

Chapter 5 provided experimental data for different types of HTS stator coils to help identify AC loss reduction. The characteristics of the different ReBCO tapes are tested for machine coil selection. The AC losses of the 2G HTS coil, including transport loss, magnetisation loss and total loss, are studied using electrical method and calorimetric method. In this chapter, a new multi-filament wire is tested to validate the total AC losses reduction in the machine stator. These results can support AC loss researches in the future superconducting machine and all HTS systems design.

Chapter 6 introduces a novel cryogenic propulsion testing platform, including cryogenic electronic parts connected with the superconducting generator. This part demonstrated how cryogenic devices influence the HTS stator coils in both steady test and transient tests. This chapter illustrates the HTS machine characteristics combine with cryogenic power electronic devices, help understand the HTS machine performance in a power application system.

Chapter 7 includes a summary of this thesis and future works.

Chapter 2 Superconductivity

2.1 Characteristics of Superconductors

When a YBCO bulk at 77 K is placed above a NdFeB magnet, the magnetic flux in the YBCO superconducting bulk is discharged from the body, causing a magnetic levitation force, making the YBCO bulk suspended in the air. This effect is the Meissner effect [2]. In 1933, W. Meissner and R. Ochsenfeld discovered that when the superconductor is in a magnetic field, in the non-superconducting state, the magnetic field can pass through the conductor, and the internal magnetic field is not zero, as shown in Figure 2.1. In the superconducting state, the magnetic flux in the superconductor is wholly discharged from the conductor, and the internal magnetic field is zero, that is, the superconductor has complete diamagnetic properties.

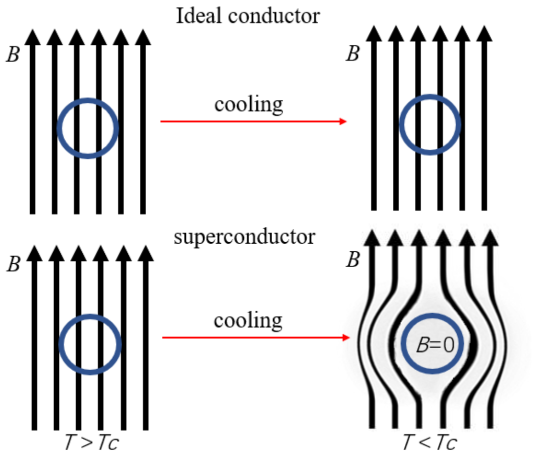

Figure 2.1. Illustration of Meissner Effect under field cooling condition.

Figure 2.1 shows in an ideal conductor, the magnetic flux within the conductor is constant with time, i.e.:

$$\frac{dB}{dt} = 0 \tag{2.1}$$

Whereas superconductor expels the entire magnetic field from its interior, the interior magnetic field is always zero, i.e.:

$$B = \mu_0 (H + M) = 0 \tag{2.2}$$

Thus, in an ideal superconductor:

$$H = -M \tag{2.3}$$

After cooling, the superconductor expels the field from its interior and has a magnetic susceptibility of $\chi = \frac{dB}{dH} = -1$. Thus, the superconductor is determined as ideal diamagnetism as well as ideal conductivity under a critical field.

2.1.1 Superconductors

The superconductors can be classified in different ways. According to their critical temperature, superconductors can be classified as low-T_c superconductors and high-T_c superconductors. Based on magnetisation behaviour, superconductors can be classified as type-I superconductors and type-II superconductors.

All superconducting materials in a superconducting state are affected by three factors: the operating temperature, the current density in the material, and the background magnetic field. As shown in Figure 2.2, the area describes the superconducting region. The superconductor has superconductivity only if the conductor's current density, temperature and magnetic field within this area [68].

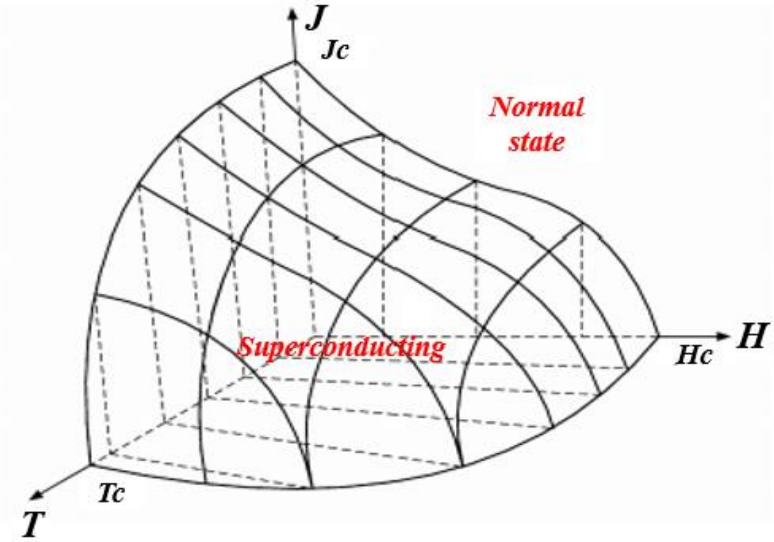

Figure 2.2. Superconductivity defined by temperature, magnetic field and current density.

- Critical temperature (Tc)

The temperature at which the superconductor transforms from the normal state to the superconducting state is called the critical temperature. When the temperature is lower than a certain value, the superconductor begins to show the phenomenon of superconductivity, which is recorded as Tc.

- Critical magnetic field (Hc)

Place the superconductor is in an external magnetic field. When the magnetic field exceeds a certain value, the superconductor will lose its superconductivity. The magnetic field strength that causes the superconductor to lose superconductivity is called the critical magnetic field strength, which is recorded as Hc.

- Critical current density (Jc)

Although superconductors can carry current with zero resistance, their current carrying ability is limited. As the current increases, the superconductor will also lose its superconductivity above a certain current value. The current value at which the superconductor loses its superconductivity is defined as critical current, which is recorded as Jc . With the increase of the carrying current, the superconductor's transition to the normal state is not abrupt. Generally, the critical current is defined based on the terminal voltage of the current-carrying superconductor reaching 1 μV/cm.

When the current is lower than the critical current, the superconductor is in a superconducting state and the resistance is zero; when the current is greater than the critical current, the resistance of the superconductor rises sharply and loses superconducting characteristics.

For high-temperature superconductors, this transition process is smoother than that of low-temperature superconductors. Figure 2.3 shows the typical U-I curves of the 2G HTS tape.

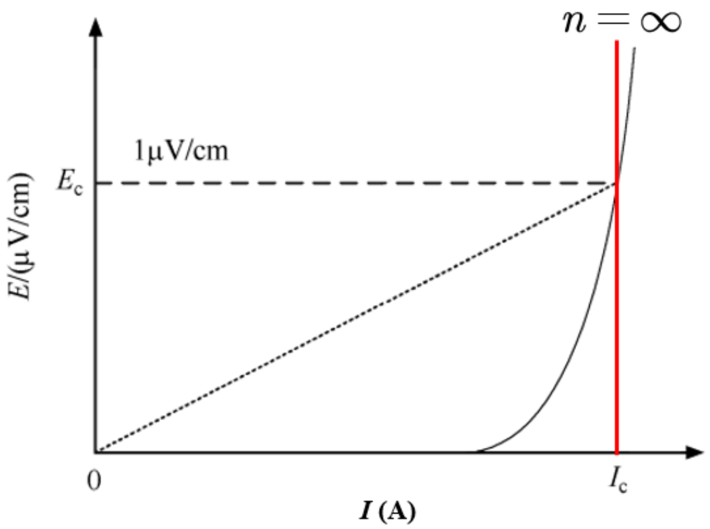

Figure 2.3. U-I curve of the superconductor.

The change of voltage with the current in a superconductor is highly non-linear, for superconductor can be shown in the equation:

$$E = E_0 \left(\frac{I}{I_c} \right)^n \tag{2.4}$$

Where E_0 = 1 μV/cm refers to the critical longitudinal voltage drop across the superconductor, I_c refers to the critical current, n refers to the exponent.

2.1.2 LTS and HTS

In 1911, when Onnes first discovered superconductivity, the critical temperature is only 4.2 K, the cryogenic systems are complex and expensive. Owing to the pursue by researchers, superconductors with higher critical temperatures have been continuously found during the following decades. Figure 2.4 shows some important superconductors until 2015 [69]. In 1986, Lanthanum-barium-copper oxide ceramic (LaBaCuO) was found, and the critical temperature reaches 30 K [5], which is a milestone temperature to classify superconductors. A superconductor is defined as a low-temperature superconductor (LTS) if its critical temperature is below 30 K. Otherwise, it is defined as a high-temperature superconductor (HTS).

LTS usually are metals, alloys, and some compounds, among which NbTi and Nb_3Sn are commonly used. HTS are typically compounds in which copper oxides, such as ReBCO. In this thesis, the HTS will be used due to its critical temperature higher than liquid nitrogen, thus, reducing the cooling equipment cost significantly.

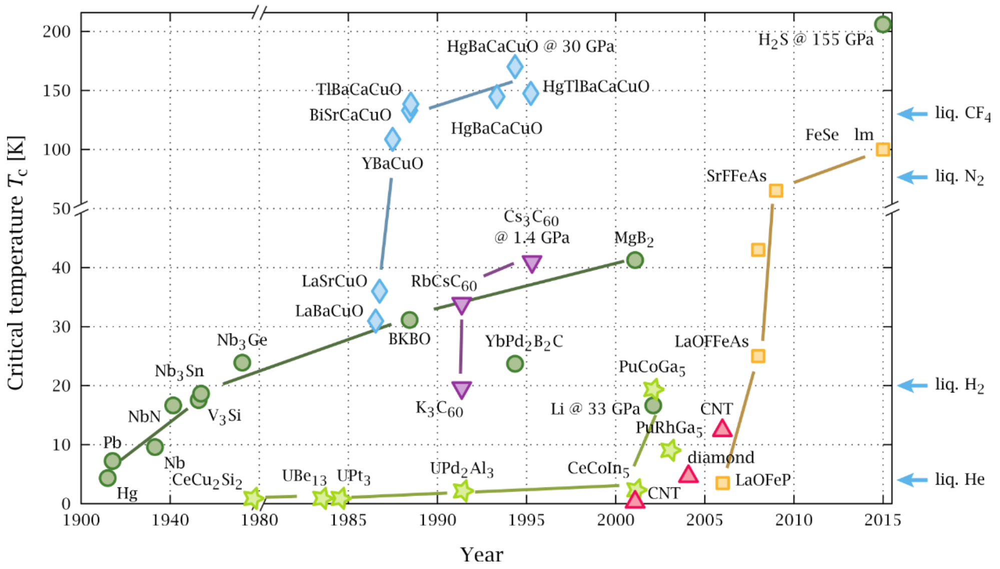

Figure 2.4. The development history of superconductors [69].

2.1.3 Type-I and Type-II superconductors

A superconductor material should have a Meissner state. Nevertheless, different superconductors have different behaviours with the increase of the external background field. Some superconductors only have one critical magnetic field and will directly enter into the normal state. This type of superconductors is called soft superconductors or Type-I superconductors. Some superconductors will enter a mixed state before entering into the normal state. This type of superconductors is called hard superconductors or Type-II superconductors. The schematic phase diagram of Type-I and Type-II superconductors is shown in Figure 2.5. Type-I superconductors only have one critical field, while Type-II superconductors have a lower critical field of H_{C1} and an upper critical field H_{C2}. Type-II superconductors are in Meissner state below lower critical field H_{C1}, normal state above upper critical field H_{C2}, and a mixed state between H_{C1} and H_{C2}.

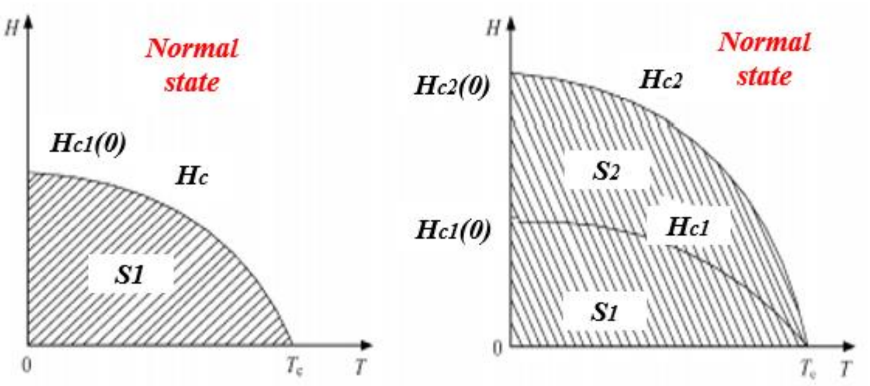

Figure 2.5. Phase diagram of type-I and type-II superconductors.

To be specific, as shown in Figure 2.6 [70], Type-I superconductors remain perfectly diamagnetic below the critical magnetic field (*H*c), and the superconductors enter a normal state suddenly when the external field exceeds *H*c. Type-I superconductors are mainly metals and alloys, such as Hg and Sn. Type-I superconductors cannot be used in high field application due to their low critical magnetic field.

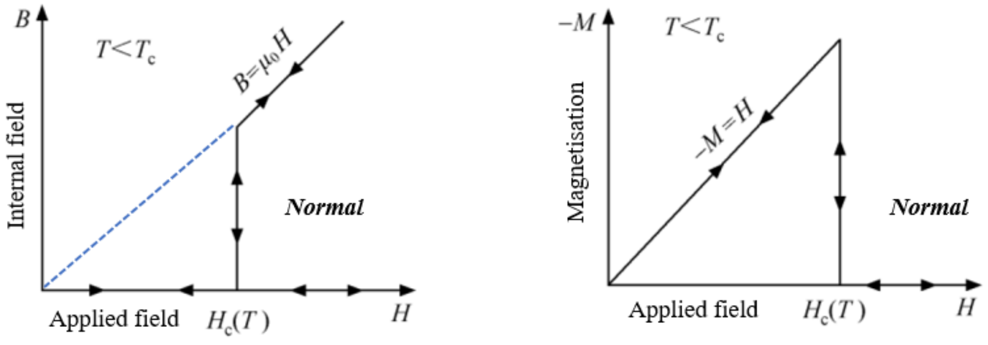

Figure 2.6. The magnetisation characteristics of type-I superconductors.

The magnetisation characteristics of type-II superconductors are shown in Figure 2.7 [70]. Type-II superconductors are in the Meissner state when the external field below H_{C1}. The magnetic field will gradually penetrate from the outer to the inner superconductors when increasing the external field. This state is called a mixed state. In the mixed state, the susceptibility is between -1 to 0. When the external field exceeds

H_{C2}, then the superconductors enter into the normal state. Type-II superconductors usually have a much higher upper critical field than Type-I superconductors. Thus, they are suitable for high-field application [71].

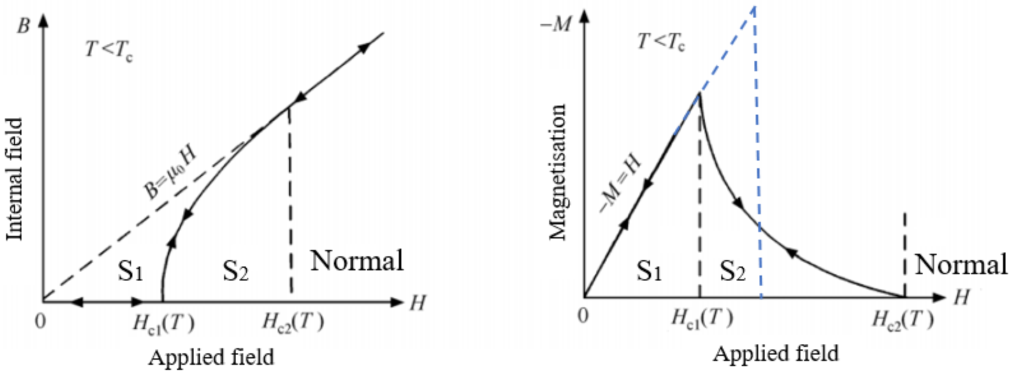

Figure 2.7. The magnetisation characteristics of type-II superconductors.

In 1950 Ginzburg-Landau theory explained the difference between Type-I and Type-II superconductors [72]. The $\lambda(T)$ is called penetration depth and describes the scale in which the external magnetic field $B(0)$ decays to zero inside a superconductor. The $\xi(T)$ is called coherence length and represents the distance between the two super electrons that constitute the Cooper pairs [73]. The Ginzburg-Landau parameter κ is defined in Equation 2.5:

$$\kappa = \frac{\lambda(T)}{\xi(T)} \tag{2.5}$$

As shown in Figure 2.8, superconductors are classified as a Type-I if $\kappa < 1/\sqrt{2}$, if $\kappa > 1/\sqrt{2}$, superconductors are classified as a type II superconductor.

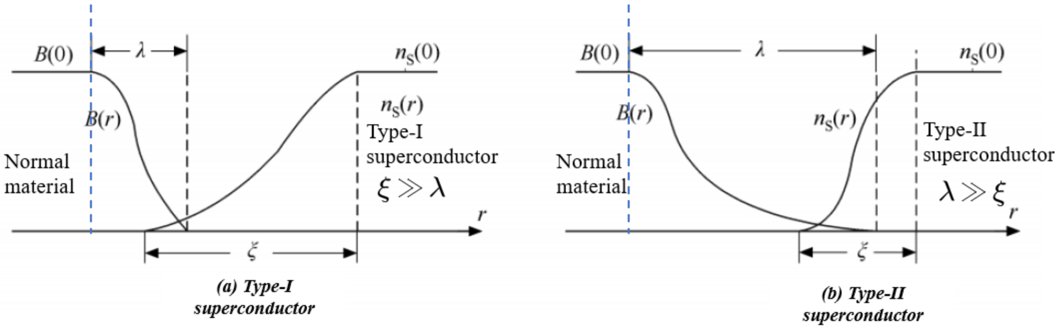

Figure 2.8. Type-I (left) and Type-II (right)

2.2 HTS superconductors

2.2.1 1G HTS and 2G HTS

At present, the typical materials of HTS are BSCCO and ReBCO. Both of their critical temperatures are above the liquid nitrogen temperature (77 K). The development process of BSCCO is earlier than ReBCO, so it is called 1G HTS, and the latter is called the 2G HTS. In recent years, the BSCCO wire manufacturing process has matured, and many superconductor companies worldwide can produce kilometres long wires. In the past decade, researchers have focussed on HTS coils based on BSCCO wire. They have applied them to demonstration projects of many power applications, including superconducting cables, superconducting machines, superconducting fault current limiter (SFCL) and superconducting energy storage (such as SMES).

As shown in Figure 2.9, The 1G HTS needs to use a large amount of silver, accounting for 70%, so its cost is very high. The costly wire affects the large-scale industrial application and commercial use of HTS seriously. Since then, the 2G HTS ReBCO has developed and more mature in manufacturing. ReBCO superconducting tape is generally composed of a base layer, a transition layer, a superconducting layer, and a protective layer [74, 75], as shown in Figure 2.9. It has a higher critical magnetic field and current density than 1G HTS. The main components of 2G HTS are cheap metals such as Hastelloy, stainless steel or copper, and ReBCO thin film. The production process requires only a minimal amount of silver (1 - 3 μm thick) and no other expensive metals. Therefore, compared to the 1G HTS, 2G HTS are expected to reduce tape costs and have commercial prospects significantly.

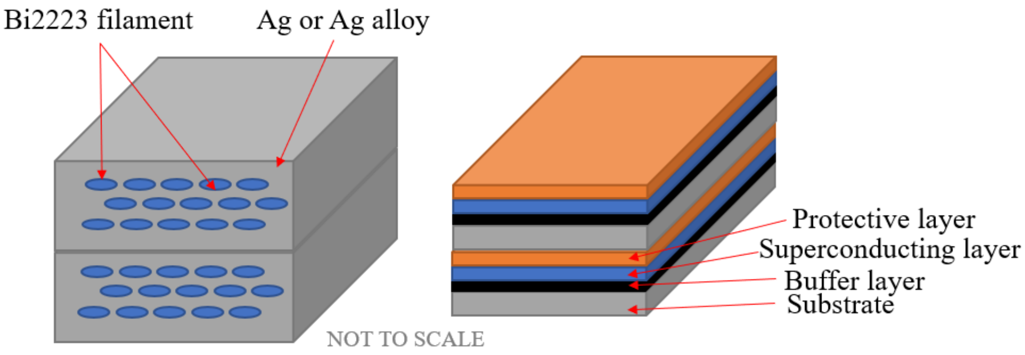

Figure 2.9. Structure of 1G HTS and 2G HTS.

2.2.2 Manufacturing of 2G HTS

At present, many superconductor companies can produce ReBCO superconducting tapes, including SuperPower, AMSC, SuNAM, Shanghai Superconductor, etc. Research on HTS coils based on ReBCO is being carried out simultaneously, which is currently one of the research hotspots in applied superconducting in the world [76-80]. In specific engineering applications, the researchers have done many designs and modelling analyses, trying to replace the copper-based conductors or LTS in the conventional equipment and the LTS superconducting equipment with 2G HTS [67, 76, 81-87].

ReBCO HTS tapes are commercially available by 2G HTS companies and are manufactured as multi-layer, as shown in Figure 2.10. Superconducting tape companies can manufacture tapes over 1 kilometre in length, which benefits large-scale magnet manufacturing [88, 89]. The ReBCO layer in the 2G HTS tape is about 1 µm. The total thickness of the tape is normally less than 100 µm. The stabilizer layer and substrate layer can enhance the tapes' mechanical performance [90].

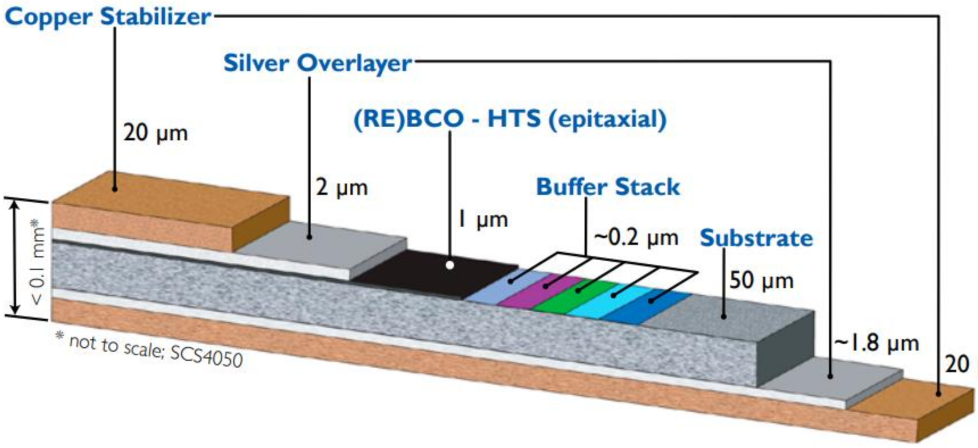

Figure 2.10. REBCO HTS tape from SuperPower® Inc. [91].

2.2.3 Critical current and E-J power law

The superconductors are zero resistance when the applied current is below the critical current, the resistance rises sharply when the applied current is equal to the critical current. In engineering applications, this U-I experimental data has usually fitted the curve with the following equation:

$$U = U_0 l \left(\frac{I}{Ic(\boldsymbol{B},T)} \right)^n \tag{2.6}$$

Where U and I are the voltage and current of the tape, Ic is the critical current, and l is the tape's length. The value of n determines the smoothness of the transition from a superconducting state to a non-superconducting state. The larger the value of n refers to the sharper the transition process. When the value of n approaches infinity, the model is the critical state model. For the 2G HTS material, the n value is usually between 30 to 50. U_0 is a constant, and its value is generally set to 1 μV/cm.

Bean’s model is first proposed as a mathematical model to describe the transition process’s electrical characteristics between the superconducting state and the normal state. In this model, the transition between the superconducting state and the non-superconducting state is stepwise and discontinuous [92]. Then E-J model is described in Equation 2.7 for high-temperature superconductors based on Equation 2.6 [93]:

$$E = E_0 \left(\frac{\boldsymbol{J}}{J_c(\boldsymbol{B},T)} \right)^n \frac{\boldsymbol{J}}{|\boldsymbol{J}|} \tag{2.7}$$

Where E_0 = 1 μV/cm. This equation agrees well with the experimental measurement, and it is very convenient for numerical solution. Thus, this formula is widely used in HTS modelling and engineering practice.

2.2.4 Critical state model and AC losses

The critical state model is an empirical model to describe the phenomena observed in the experiment. The critical state model deals with Type-II superconductors in a mixed state while ignoring the Meissner state. The model assumes that the superconductor’s outer part is in the so-called “critical state” while the interior region is in the “virgin state” for low applied fields or currents. Many models predict the current density and magnetic field in the critical state region, e.g., Bean's model [92, 94]. It assumes that the current density is always constant in the critical state region as J_c, and in the virgin state region, the current density is always zero.

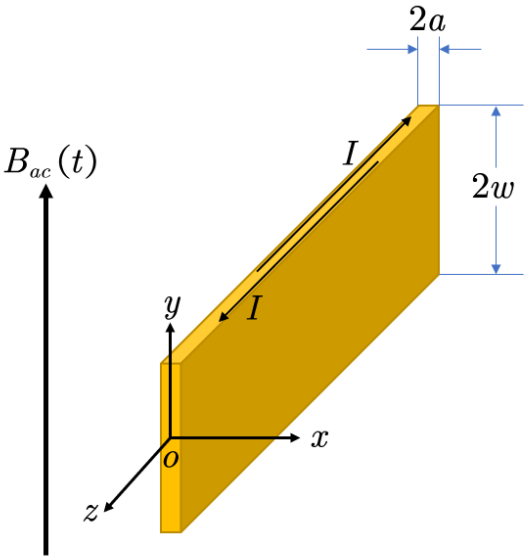

Figure 2.11. Geometry of an infinitely long tape in an external AC magnetic field.

As Figure 2.11 shows, the superconducting tape with thickness and width $2a$ and $2w$ is in an AC magnetic field $B_{ac}(t) = B_0 \sin(\omega t)$, and there is no transport current in HTS tape. The current I refers to the induced current in the superconductor by the AC magnetic field. The magnetic field is along the y axis. The induced currents are along with the $\pm z$ directions.

The magnetic field and current present in a superconductor are described by Ampere's Law:

$$\nabla \times B = \mu_0 J_c \tag{2.8}$$

Which means the field and current are perpendicular to each other at every point. In Figure 2.11, Equation 2.8 is simplified as:

$$\frac{dB}{dx} = \mu_0 J_c \tag{2.9}$$

According to Bean's model, the possible current density values are: 0 and $\pm Jc$. Jc is a constant value in the critical state region and will not be changed with the background magnetic field. In the case of the magnetic field increase, when the magnetic field is a small value below critical field $H^* = J_c a$, when $0 < H_1 < H^*$ as state 1 shown in Figure 2.12, the magnetic field of the position $-x_c$ is zero, indicating that penetration depth of the critical state region is determined by $-x_c = H/J_c$. When the applied field increases continuously until $H_2 = H^*$, as state 2 shown in Figure 2.12, the magnetic field is zero at position 0, indicating that $H = H^*$, the magnetic field thoroughly penetrates the superconductor. When the applied field further increases, $H_3 > H^*$ as state 3 shown in Figure 2.12, the centre's magnetic field is increasing.

In contrast, Figure 2.13 shows the field cooling process. Firstly, the field in the whole superconductor is $H^* = J_c a$. With the decrease of the external field, a current is induced in the outer part of the sample. When the field reduces to zero, a field $H^* = J_c a$ is trapped in the centre of the superconductor.

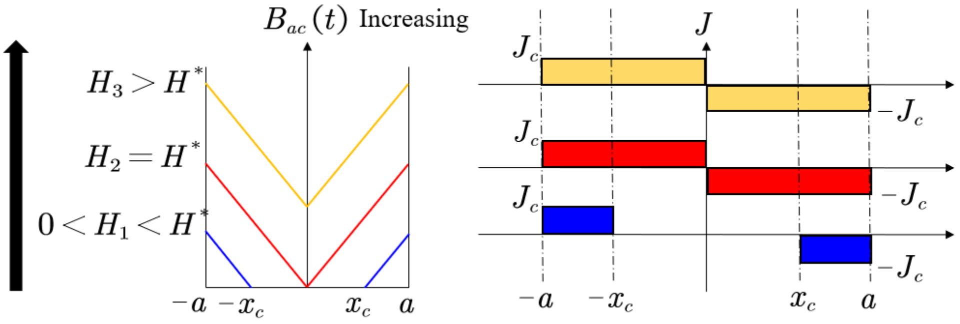

Figure 2.12. Magnetic field and current distribution in a superconductor according to Bean's model.

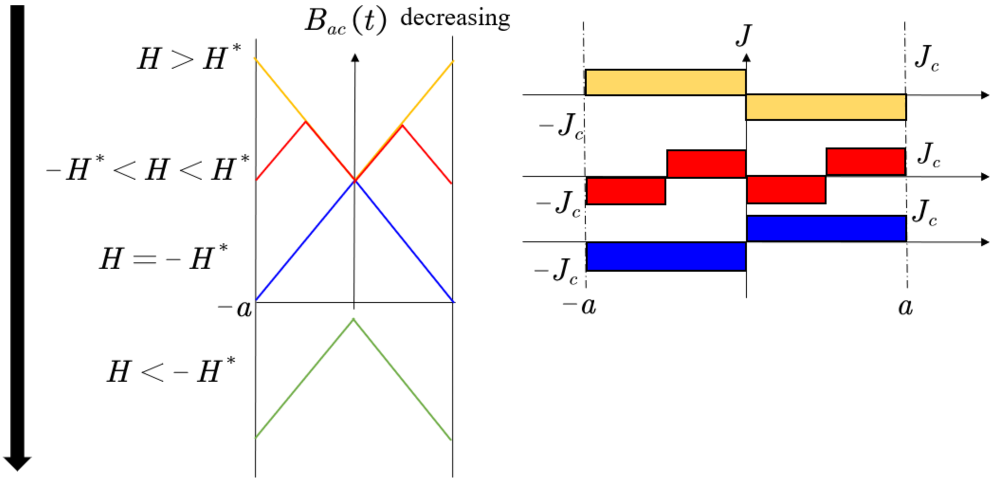

Figure 2.13. A schematic of the magnetic field distribution in a superconducting tape during the change of external magnetic field H, according to Bean's model.

According to the critical state model, when the transport current in a superconductor is DC and/or under a DC magnetic field, the superconductor's AC losses are zero.

However, when the superconductor is carried an AC transport current or under an AC background magnetic field. The magnetic field inside the superconductor will redistribute due to AC transport current or AC external magnetic field. According to Faraday's law, magnetic flux motion inside a superconductor induces an electric field of E. Since the electric field is always in the same direction as the current density J inside the superconductor, there are losses described as:

$$Q = \int_V EJdV \tag{2.10}$$

Where Q is the total loss in the superconductor. V represents the entire superconducting domain. The transport loss is caused by AC current, and the magnetisation loss is caused by an external AC magnetic field [95]. Both of these losses occur when the superconductor is transporting an AC current under an AC magnetic field.

2.3 AC losses in Superconducting machines

2.3.1 AC losses in HTS machine

The majority of HTS machines are designed based on conventional topologies. In this case, the copper-based winding can be replaced with superconductor materials [96]. According to AC loss caused by AC transport loss or external AC magnetic field, the AC losses are categorized into transport loss and magnetisation loss. HTS rotor windings carry a DC current under its critical current and operate in a complex magnetic field, including a fundamental base field and higher-order harmonic field. In this case, the magnetisation loss needs to be focused on rotor design. As for stator windings, the HTS coils carries an AC current and operates in a rotational magnetic field. In this case, both magnetisation loss and transport loss need to be studied. These losses need to be appropriately evaluated and quantified in both stator and rotor in machine design.

To avoid high power dissipation caused by AC loss, the majority of previous research only focuses on the partially superconducting machine and only applied HTS material in rotor windings. In this case, the overall power density is limited due to copper-based windings used in the stator and the iron material's saturation issue. To achieve a goal of 20 kW/kg (active material only) [97], a fully HTS machine must be pushed forward for future power applications, e.g., future electric aircraft [97]. The AC loss of the coil increase when the applied transport current or external field increase. In aircraft applications, high frequency and high transport current are required. Thus, higher power cryogenic power is required. In cryogenic temperature, the power dissipation caused by AC loss become a heavy burden to cryogenic systems [98]. Considering the cost of HTS materials in future power applications, e.g., all-electric aircraft HTS systems including HTS generators and motors, HTS cables, HTS transformers and SFCL (superconducting fault current limiter). As too much silver is used in 1G HTS BSCCO material, 2G HTS material should be applied in all HTS systems to reduce the cost of the material. The AC losses of 2G HTS in HTS machines can be estimated in Table 2.1 [99].

Table 2.1 Estimated heat loads of HTS machines at operating temperature

HTS devices	Power ratings	YBCO material heat load (W)	Operating temperature (K)
Generators	10 – 500 MW	100 – 500	50 – 65
Motors	1 – 10 MW	50 – 200	50 - 65
Cables (per phase per metre)		3 – 5	65 - 80
Transformers	5-100 MVA	50 – 100	60 - 80
SFCL		1000	50 - 80

Therefore, high power cryogenic refrigerators are required to maintain operating temperature to protect HTS devices. However, superconducting devices' operating temperature can be designed varying from 4.2 K to 77 K. The real power of commercially cryogenic refrigerators is much higher than the ideal calculation at cryogenic ambient temperature when cooling power above 100 W. According to Carnot efficiency, an ideal Carnot Specific Power of 2.94 W is required to provide 1 W of refrigeration at 77 K ambient temperature; however, the practical power rating of the cryogenic refrigerator can be up to 20 W. When the ambient temperature reaches 4.2 K, the practical power rating can be 11000 W to provide 1 W of refrigeration [99]. Thus, reducing AC losses in HTS components can significantly reduce the cooling power of cryogenic systems

To solve the issue of high AC losses in stator windings, first of all, the AC losses need to be identified and quantified separately in the stator and then focus on AC loss reduction techniques. A number of researches have been done to identify AC losses in HTS samples or HTS coils. There are three methods to measure the AC losses of coils: electric, magnetic, and calorimetric methods [100]. However, the magnetic method is typically applied in static measurement and for short samples. Thus, to study AC loss in the HTS machine, the electric and calorimetric methods are discussed in detail.

2.3.2 Measurement methods for AC losses

2.3.2.1 Electrical method

The electrical method uses an electrical circuit to measure the AC loss, including cancelling coil method or lock-in amplifier method [101, 102]. Figure 2.14 shows the equivalated circuit of the cancelling coil method.

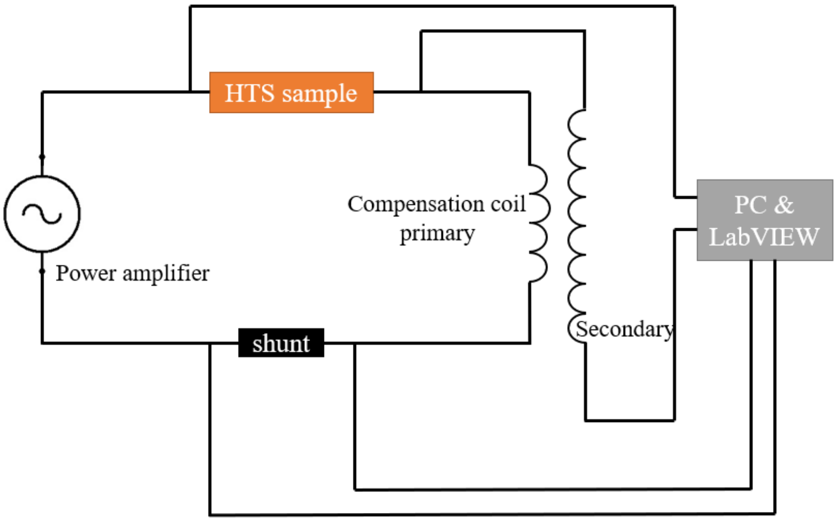

Figure 2.14. Equivalent circuit for the electrical method.

To measure the transport loss of the HTS coil, a compensating coil consists of two coupled coils that can be used to compensate for the coil voltage. The primary coil is wound by a few turns (around 10) of the current cable; the secondary coil is wounded by thin copper wire with a large number of turns (more than 500). By adjusting the relative positions of the primary and secondary windings, the inductance signal from the compensating coil's secondary winding can compensate for the inductive component of the HTS coil's voltage. The transport AC loss can be calculated by:

$$Q = \frac{I_{rms}V_{rms}}{f} \ (Joule/cycle) \tag{2.11}$$

Where f is the frequency of the transport current, I_{rms} is the root-mean-square value of the transport current in the HTS sample, and V_{rms} is the root-mean-square value of the in-phase voltage component from the voltage taps.

A compensation coil (cancelling coil) is used to compensate the voltage signals in-phase with the transport current. The reference signal can be taken from the primary side of the compensation coil by adjusting the cancelling coil's secondary side until the inductive component of the voltage was cancelled. The transport AC loss can be calculated by the purely resistive part using Equation 2.11.

Figure 2.15 demonstrates the AC loss measurement platform based on the electrical method to measure the sample's transport loss.

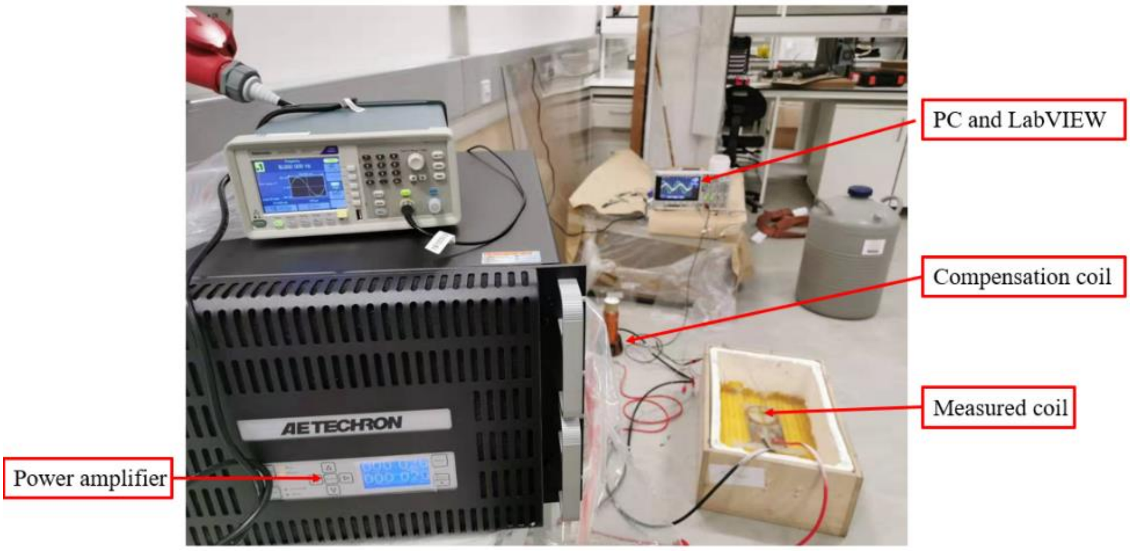

Figure 2.15. Electrical method to measure transport AC loss.

2.3.2.2 Calorimetric method

The AC loss can also be measured by the calorimetric method (the boil-off method) [36, 103-106]. Figure 2.16 illustrate the structure of the boil-off method. The AC losses produce heat in liquid nitrogen, causing liquid nitrogen to evaporate. The latent heat of liquid nitrogen is 199 Joule/gram [107], thus, the flow rate of liquid nitrogen is equal to 0.25 Standard Litre/min/W.

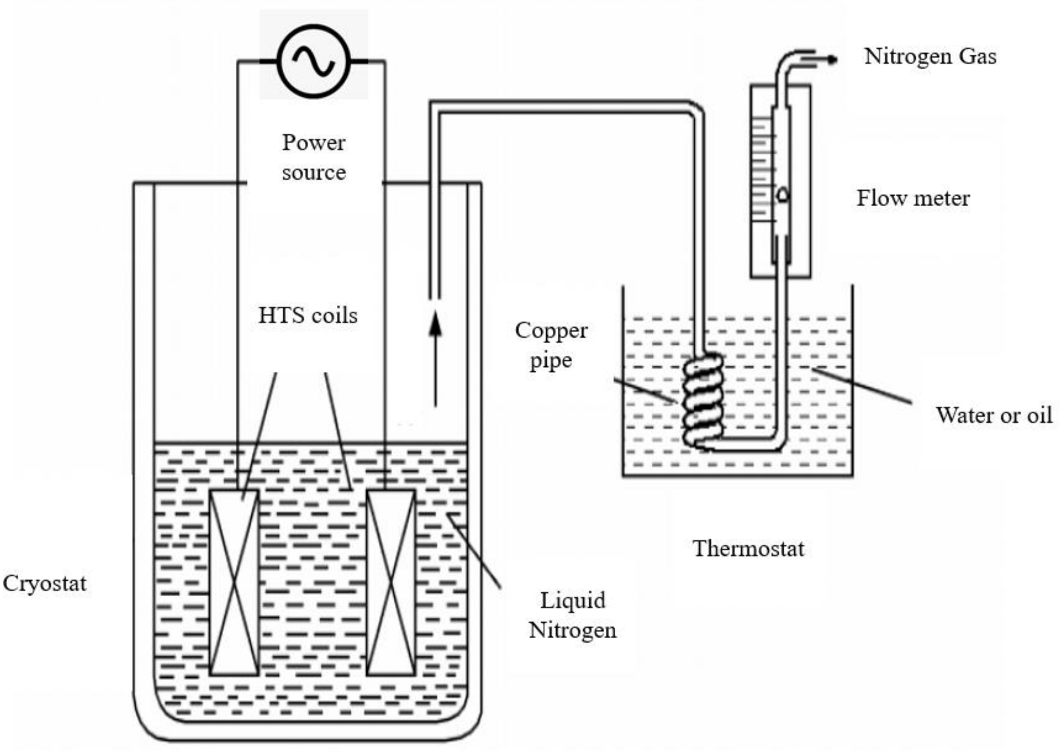

Figure 2.16. Diagram of the boil-off method.

The calorimetric method can be used in any condition of the background AC magnetic field, including magnetisation AC loss, total AC loss, regardless of the phase difference between the AC and background field.

However, the sensitivity and accuracy of the calorimetric method are not as high as the electrical method. In our setup (after calibration), the background flow of the calorimetric method is not as sensitive as the electrical method. A fluctuation of 0.08 SLPM and an unavoidable background flow rate around 1 SLPM is observed in the testing setup.

Table 2.2. Measurement method comparison

	Electrical method	Calorimetric method
Measuring speed	Fast	Slow
Small sample	Suitable	Not suitable
Complex AC magnetic field	Not suitable	Suitable
Magnetisation/Total loss	Cannot measure	Can measure

Table 2.2 shows the comparison between the electrical method and the calorimetric method. The advantages of the electrical measurement method are fast measurement speed and high accuracy, and suitable for the short superconducting sample. Compared with the electrical method. First of all, the calorimetric method has a wide range of applications, and the setup does not require complex electronic circuits and high-precision instruments. It is suitable for any AC magnetic field wave and any direction.

Moreover, the calorimetric method can measure regardless of the AC magnetic field and the AC current phase difference. Secondly, the calibration of the calorimetric method is more accessible than the electrical measurement method. However, the calorimetric method also has its shortcomings. Because the heat and temperature changes are much slower than electromagnetic propagation, the measurement process takes longer. For traditional low-temperature superconductors, liquid helium is usually used as the cooling system. Its latent heat is very low, liquid helium is easy to evaporate, and the thermal measurement method is relatively easy. For HTS, at 77 K liquid nitrogen temperature, the latent heat of liquid helium is large, which is more than 60 times that of liquid helium. Therefore, the calorimetric method is not suitable for short samples. For small superconducting samples, the electromagnetic environment is simple, and it is best to use electrical methods to measure AC loss. If the superconducting sample is large and the electromagnetic environment is complex, it is best to use the thermal method to measure the AC loss.

2.3.3 AC loss reduction techniques in machine design

According to the heavy penalty in cooling systems, the AC loss reduction techniques are needed in fully HTS machine design. The cross-sectional aspect ratio needs to reduce to minimise the magnetisation loss. The typical width of a ReBCO tape is 2-12 mm. The AC loss can be reduced by using a filament structure [108-111]. Consider a Type-II HTS strip with the width of $2w$ and thickness of h subjected to a field applied perpendicular to its face, with an amplitude of H_p, critical current J_c (A/m) flows from the edge, the magnetisation loss per unit per cycle can be calculated as [112-114]:

$$Q = \frac{8\mu_0 {J_c}^2 w^2}{\pi} \left\{ \ln \cosh\left(\frac{\pi H_p}{J_c}\right) - \frac{\pi H_p}{2J_c} \tanh\left(\frac{\pi H_p}{J_c}\right) \right\} \ (J/m/cycle) \qquad (2.12)$$

According to Equation 2.12, the filament method can significantly reduce the magnetisation loss due to loss is proportional to the square of the width of the tape. In machine applications, the windings are operated in a complex electromagnetic environment. Thus the structure of the wire need to be considered as ReBCO is a fragile ceramic material. The new filament wire structure, which is called soldered-stacked-square (3S) wire, has been proposed in [115]. The fundamental idea of 3S wire is to cut the HTS tape into 1 mm width mechanically, and put several 1 mm wire into a stack, and then soldering. This process enables HTS wire to have lower AC loss as well as higher mechanical strength in machine application. The performance of 3S wire in a machine environment is discussed in detail in Chapter 5.4. Several other structures of HTS wire have been developed by some institutes and companies, e.g., ROEBEL cable [53] and CORC® cable [54]. The structure of the ROEBEL and

CORC® cable is shown in Figure 2.17. ROEBEL cables are compact transposed cables due to transposition, and coupling loss is minimised for high current applications to achieve low AC losses. CORC® cable is manufactured by the helical winding of 2G HTS tapes on a round former, and the AC loss can be reduced by narrowing the width and enable the wire more flexible.

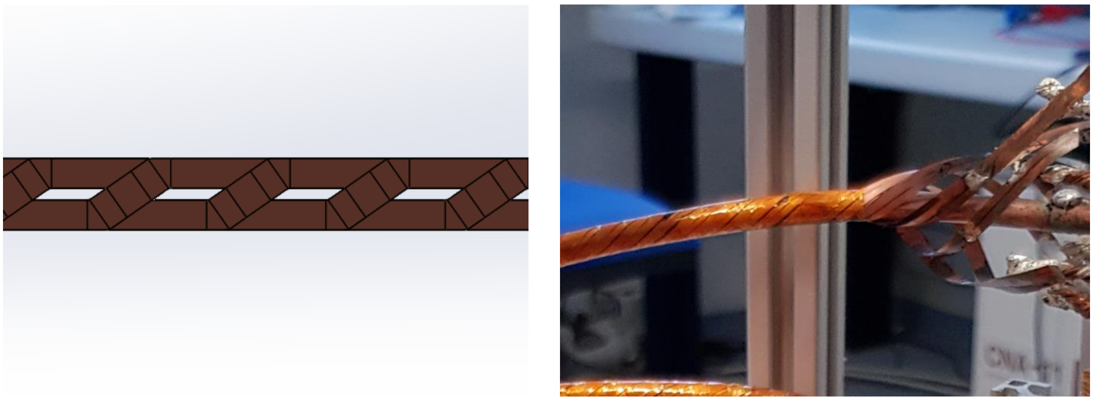

Figure 2.17 Structure of ROEBEL cable (left) and CORC® cable (right).

2.4 Winding techniques in HTS machine: Insulated HTS coils and NI HTS coils

The superconducting machines using HTS coils have always suffered the problem of low thermal stability and quench damages [116-118], which is the greatest challenge for the safety and reliability of superconducting electrical propulsion design. No effective quench detection and protection technique are developed so far for HTS windings because of the low quench propagation velocity of HTS tape [118-122]. Then, an alternative solution, the novel no-insulation (NI) coil technique, was proposed to enhance the thermal stability of HTS windings in electrical machines [59, 60, 67, 123, 124]. No-insulation (NI) coil refers to the partial or complete cancelling of the traditional insulating between turn-to-turn in the superconducting coil. All the current would be carried in the superconducting layer in DC operating conditions due to zero resistance of the superconducting layer. This structure enables the quench current to bypass the quench area, and it can flow between the turns along the contact surface of the turn. Figure 2.18 shows the photo of an insulated coil and an NI coil. In 2010, Hahn and Iwasa of MIT applied NI technology to high temperature superconducting coils for the first time. In a comparative experiment of NI coil and insulated coils based on 1G and 2G HTS tapes, the NI coil withstood an overcurrent of 2.3 times the coil's critical current, and the HTS tape did not suffer irreversible damage [56] to compare with insulated coils. The NI HTS coil has higher thermal stability and self-protection capabilities. Many other research institutions have successfully joined this research field [55-67]. Both the EU and NASA have proposed to develop the NI HTS machines concept for electrical aircraft propulsion [125].

Figure 2.18. Photos of Insulated pancake coil (left) and No-insulation coil (right).

Since the 2G HTS tape is a coated conductor, the tape geometry is suitable for winding NI coils. The 2G HTS tape is better than the 1G HTS; thus, NI HTS coils' research has been mainly carried out based on the 2G HTS tapes. NI coil technology is feasible to use in magnet manufacturing. The first 2G HTS NI HTS coil magnet, which generated a 4 T DC magnetic field, was developed in 2013 [126].

2.4.1 Coil selections in HTS machine

In a superconducting rotor, the magnetic field can be generated by the permanent magnet or the insulated HTS racetrack coil. However, there are some disadvantages for PM or insulated coil. The insulated HTS coil is easy to quench and difficult to protect in real operation. Thus, using NI technology in the rotor quickly became a research hotspot. Using NI coil in HTS machines for electrical aircraft has been widely proposed by researchers. One issue that is worried the most is the NI HTS coil's electromagnetic behaviour in an AC magnetic field environment, since the NI HTS winding technique has always been applied in the DC environment before.

In synchronous machines, the rotational speed of fundamental fields generated by stator windings is the same as the rotor's rotational speed. Thus, the HTS rotor winding is stationary relative to fundamental fields. Besides the fundamental fields, the ripple fields from stators cause by are not synchronous to the rotor windings. The higher-order ripple field in the machine with a small amplitude (mT-class) may be caused by iron materials, electronic components or imbalance power loads. Therefore, the HTS coils on machines' rotors will suffer AC ripple magnetic fields [127].

The magnetisation loss of an NI coil in a 0.45 T magnetic field is demonstrated, as Figure 2.19 shows, the testing platform is shown in detail in Chapter 3, the result indicated that the magnetisation loss of the NI coil is 12.39 Joule/cycle, as Figure 2.20 shows, the coil loss is significant in a large amplitude AC magnetic field. Thus, in machine design, insulated coils must be used in stator windings. NI coil has the potential to be applied to the synchronous machine rotor only. The NI HTS coil's electromagnetic behaviour need to be studied in a small ripple magnetic field. This issue is discussed in Chapter 4 in detail.

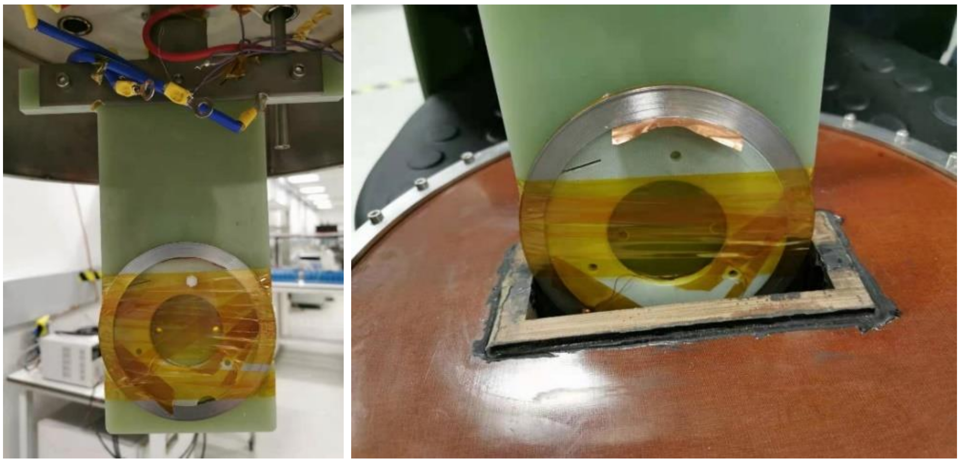

Figure 2.19. NI coil test in a 0.45 T magnetic field.

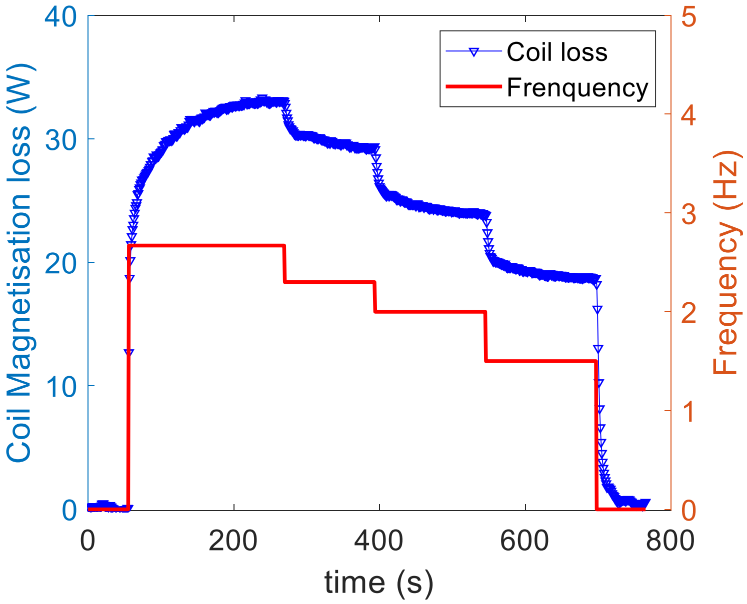

Figure 2.20. Magnetisation loss of a NI coil in 0.45 T rotational magnetic field.

2.4.2 Circuit network model for NI coil

The NI HTS coil is hard to simulate using the FEM directly: first, the current can flow along with any directions inside the NI HTS coil. Thus, a 3D model is required for the FEM simulation, while the HTS tape has a very high aspect ratio (e.g., width 12 mm, thickness 0.25 mm). Thus, it is hard to mesh a 3D HTS coil with many turns. Second, the HTS tape resistance is highly non-linear, which is hard to converge for complicated structure 3D FEM model.

The simulation model study is first developed by Hahn's research team using the circuit equivalent method [60]. The NI coil is equivalent to an *RL* circuit, where the *L* is the inductance of the coil itself, the resistance is equal to the radial resistance when the current flows between the turns, this model is widely used in subsequent studies.

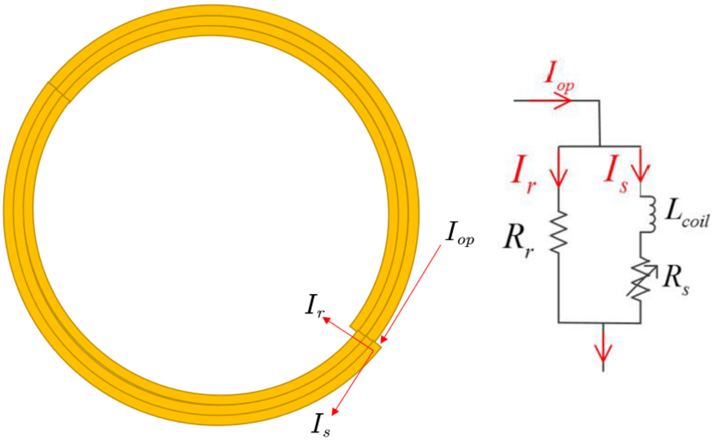

Figure 2.21. Equivalent circuit for NI ReBCO pancake coil.

Figure 2.21 illustrated the equivalent circuit for the NI ReBCO single pancake coil. The whole NI coil is equal to a circuit model, including the coil inductance L_{coil}, radial resistance R_r and azimuthal resistance R_s. Assuming the current is evenly distributed in the coil, R_r refers to resistance from turn to turn contact and resistance between multilayer inside the tape. R_s refers to the resistance along with transport current in the azimuthal direction. When transport current below critical current, all the current would be carried in the superconducting layer with zero resistance, i.e. $R_s = 0$. The governing equation for this model can be described as:

$$\begin{cases} V = L_{coil}\dfrac{dI_s}{dt} + I_s R_s = I_r R_r \\ I_{op} = I_s + I_r \end{cases} \tag{2.13}$$

Where I_{op} refers to the operating current in the coil, it equals the current from the power source. V refers to the coil voltage. This model agreed well with the experiment in a steady-state and described the NI coil's external performance.

However, the above model regards the whole coil as inductance and a non-linear resistance, and the model cannot reveal the current distribution in the coil. These studies cannot clearly illustrate the current distribution, temperature, magnetic field during operating. It is necessary to have a more comprehensive and detailed understanding of its internal electromagnetic characteristics and influencing factors.

Thus, an advanced circuit network model has been proposed. For the first time, this research studied the induced eddy current and loss in the NI HTS coil exposed to ripple background fields. Furthermore, the details are discussed in Chapter 4 [127].

Figure 2.22 illustrates the advanced circuit network model for a NI coil. Each turn of the NI HTS coil is subdivided into several fine arc elements. Each arc element is equivalent to circuit parameters; thus, the whole coil is equal to a circuit network. In Figure 2.22, the coil is subdivided into four arc elements, to present the model clearly. In Chapter 4, the coil is subdivided into 16 arc elements in order to achieve higher accuracy.

The NI HTS coil is modelling using a circuit network model. The external copper coil is coupled to this circuit network model directly using mutual inductance, as shown in

Figure 2.23. The background AC magnetic field is generated by a bigger size copper solenoid coil, and the copper coil is excited by a current source in this model. Thus, the background field is not affected by the NI coil.

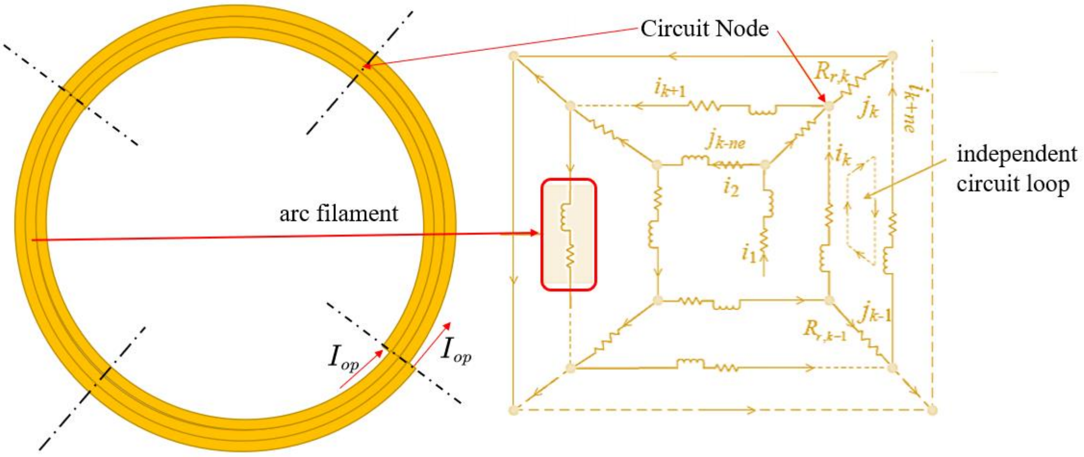

Figure 2.22. Advanced circuit network model for NI coil.

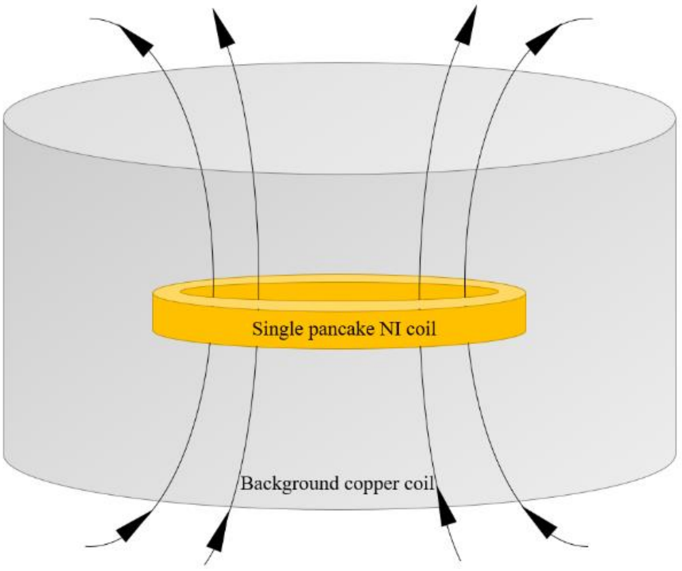

Figure 2.23. Single NI coil in the background AC magnetic field.

2.4.3 Circuit network model validation

The NI coil testing rig is built to validate the circuit network model for the NI coil. The distribution of the eddy current induced in the NI HTS coil is hard to measure directly. However, this induced eddy current generates an opposite magnetic field at the coil centre. The amplitude of this opposite magnetic field is proportional to the eddy current induced by the background AC field, and its frequency is the same as that of the magnetic field. Therefore, this opposite magnetic field can represent the eddy current induced by the background AC field.

Thus, using a hall sensor to measure the centre magnetic flux in the copper solenoid coil with/without the NI coil. The magnetic field generated by the NI coil can be calculated. The simulation model developed is to calculate the current distribution in the NI HTS coil. Suppose the opposite magnetic field from this model agrees well with that from measurements, then it largely validates the model.

In theory, the coil AC loss can be measured with the difference. However, when the induced eddy current is below the critical current, the induced AC loss in the NI HTS coil is very low compared to the loss in the copper coil. The copper coil has many turns in series, and the inductive voltage is very high. Therefore, it is not easy to measure the NI HTS coil’s AC loss with enough accuracy using the calibration-free method, especially when the induced azimuthal current below the critical current.

The Joule loss is generated on the turn-to-turn contact by the induced eddy current. If the eddy current calculated was reliable, the turn-to-turn loss from this model is also reliable. Thus, the platform was mainly built to validate the current distribution and measure the time constant of the NI coil. All the AC loss discussion in Chapter 4 is from the simulation.

Due to the voltage limit of the AC source, the experiment is operated and validated at 40 Hz. Also, the simulation model is a circuit network consists of resistors and inductances, the turn-to-turn resistivity is a constant, the inductance value is a constant, the resistance of the HTS layer is zero when the operating current below critical current. Thus, this model will not be influenced by the frequency and DC component. In Chapter 4's discussions, the AC loss will be discussed from 1 Hz to 1000 Hz. In a real machine, the rotor will be connected with a DC power supply, but base on the superposition theorem, the DC current can be removed. The NI coil will open-circuit in simulation to demonstrate the electromagnetic behaviour clearly.

The NI coil testing rig is illustrated in Figure 2.24. The single pancake NI coil is placed in the centre of the copper solenoid coil to study the coil performance in a uniform AC magnetic background field. The copper coil is connected with an AC current source. The NI coil is connected with a DC current source. Results from simulation and experiments are compared in detail in Chapter 4.

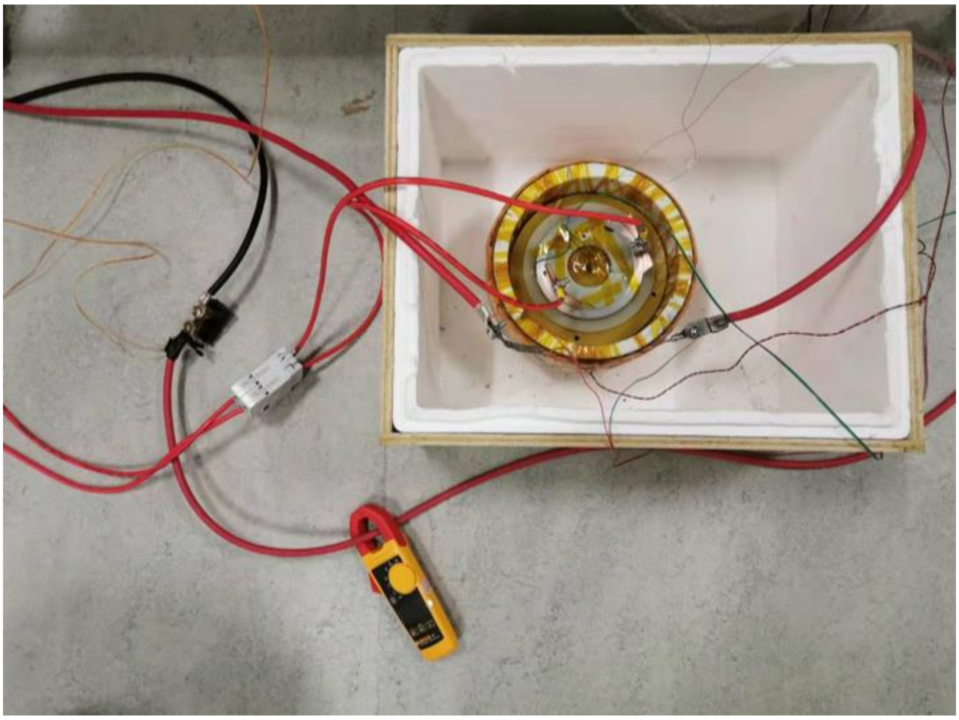

Figure 2.24. NI coil testing in a ripple magnetic field.

2.5 Conclusions

This chapter demonstrates the basic theory of superconductors and a brief introduction of the superconducting machine. The critical issue of HTS material is the AC losses. The methodologies of AC loss measurement are demonstrated in this chapter. Also, winding technologies are discussed in this chapter, including insulated coil and NI coil.

The motivation is to study the coil's performance in the machine environment for a fully superconducting machine. A fully superconducting machine test can be achieved in two parts:

- A permanent magnet machine test rig to study the HTS stator coil in a rotational magnetic field.
- An AC background testing rig to study the rotor coil in an AC ripple field.

These two parts could provide data for stator windings and rotor windings separately and more reasonably in experiments.

The HTS stator testing rig is based on the boil-off method. The testing rig provided a 0.45 T rotational field at a maximum of 10 Hz, and one HTS coil is sitting in a measurement chamber and connected with a flowmeter, allow to measure the nitrogen gas flow rate during the operation, the coil AC loss can be calculated which demonstrated in Chapter 3 in detail. Also this machine can connect with cryogenic power electronics which demonstrated in Chapter 6.

The rotor coil model is developed based on a circuit network model which demonstrated in Chapter 4 in detail.

Chapter 3 HTS machine setup and validation

Fully superconducting machines provide the high-power density required for future electric aircraft propulsion. However, superconducting windings generate AC losses in AC electrical machine environments. These AC losses are difficult to remove at low temperatures, and they add an extra burden to the aircraft cooling system. Due to the heavy cooling penalty, AC losses in the HTS stator are key topics in HTS machine design. To evaluate the AC loss of superconducting stator windings in a rotational machine environment, a novel axial-flux high temperature superconducting (HTS) machine platform was designed and built. The AC loss measurement is based on calorimetrically boiling-off liquid nitrogen. Both total AC loss and magnetisation loss in the HTS stator are measured in a rotational magnetic field condition. This platform is essential to study ways to minimise AC losses in HTS stators in order to maximise the efficiency of fully HTS machines.

3.1 Introduction

In a fully HTS machine, the HTS stator is subjected to a rotational AC magnetic field, as well as an AC transport current. So it generates AC losses, which will potentially increase the size and weight of the machine cooling system. The key challenge of developing a fully HTS machine is to minimise HTS winding AC losses. So far, most of the research on HTS tapes and coils has focused on transport AC loss or magnetisation loss in a uniform magnetic field [100, 101, 113, 128-136]. There are few studies on the AC loss of HTS in a rotational magnetic field [137]. The US Air force proposed to measure the magnetisation loss in a rotational magnetic field generated by a radial type permanent magnet rotor. Nevertheless, the study does not consider the influence of transport currents [36].

Previous studies on the calorimetric method for AC loss measurement of HTS at liquid nitrogen temperature (77 K) have been reported [36, 103-106], including an AC background magnetic field. The system measured the boil-off rate of LN_2. The main advantage of using the calorimetric method is that it can measure the total loss from an HTS coil regardless of the phase difference between the applied current and the background field [138, 139]. There is a lack of measurement systems to study AC loss in rotational machines. Thus, a novel axial flux HTS machine testing platform was designed, built and test to study the AC loss performance of the HTS stator.

This machine platform was firstly designed and developed by Dr Jay Patel at the University of Bath [140], in his research period, he designed and built the machine cryostat, including thermal design, bearing selection and machine manufacturing process, also, a cryogenic rotor was successfully design and built at 77 K, the inner cryostat was also well designed, this machine can provide a rotational magnetic field. In this chapter, the progress is pushed further, including error calibration, machine validating and full system testing. The whole machine environment is effectively evaluated and enable to measure magnetisation loss and total AC loss of the HTS coil in a real-time operating machine. In section 3.2, a novel HTS machine platform is proposed based on the calorimetric method to measure the total AC loss in a rotational magnetic field. Section 3.3 demonstrated the whole system design and setup. Section 3.4 explains system calibration and validation.

3.2 Design concepts of stator coil testing rig

An axial flux testing rig was manufactured and delivered in 2018, including achieving a PM rotor in liquid nitrogen temperature, sealing and bearing test in cryogenic temperature, and the dewar test. The following items are needed to discuss in detail:

- Machine environment evaluation
- Machine testing rig setup
- Systems validation and calibration
- Error discussions

According to the machine structure, the rotor operated in liquid nitrogen. The operating RPM is designed below 300 RPM, considering the limit of the bearings in the cryogenic temperature.

3.2.1 Axial flux machine

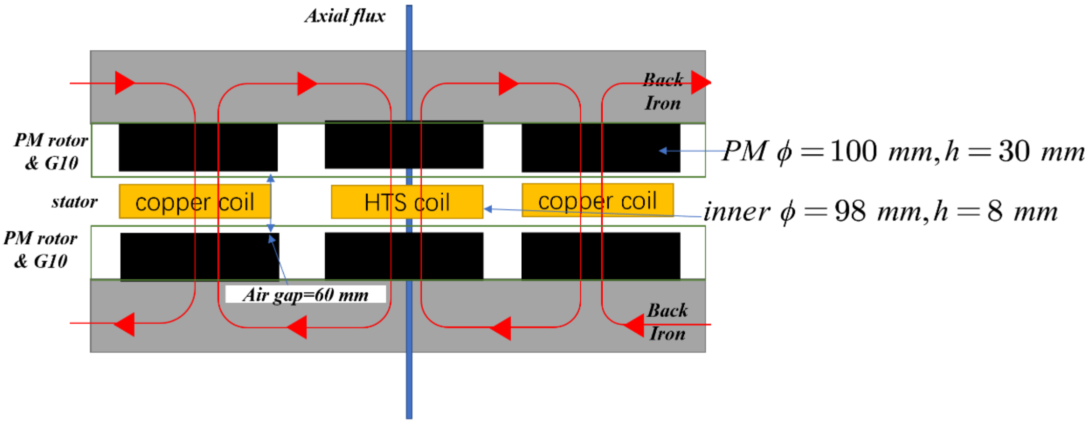

Figure 3.1. Axial flux machine structure.

The testing rig is designed as an axial flux structure to minimise the electromagnetics' influence between the stator coils. It is also easier to place a measurement chamber to separate one coil to study the AC losses. Figure 3.1 shows the structure of the stator and rotor. The permanent magnet was supported by Epoxy and provided an 0.45 T (measured value) magnetic field strength in the 60 mm air gap. The permanent magnets in the rotor were chosen as 8 NdFeB magnets, the diameter is 100 mm and the thickness is 30 mm. This structure enables to sit a measurement chamber made by Tufnol material [140].

3.2.2 Machine environment evaluation

The testing rig's topological structure is shown in Figure 3.2 (left). The testing coil is sitting between the rotor. The evaluation of the electromagnetic environment needs to be discussed in detail before the system's validation. The photo of the machine is demonstrated in Figure 3.2 (right), the outer diameter of the machine is 610 mm and the height is 800 mm. the total weight of the machine is around 400 kg.

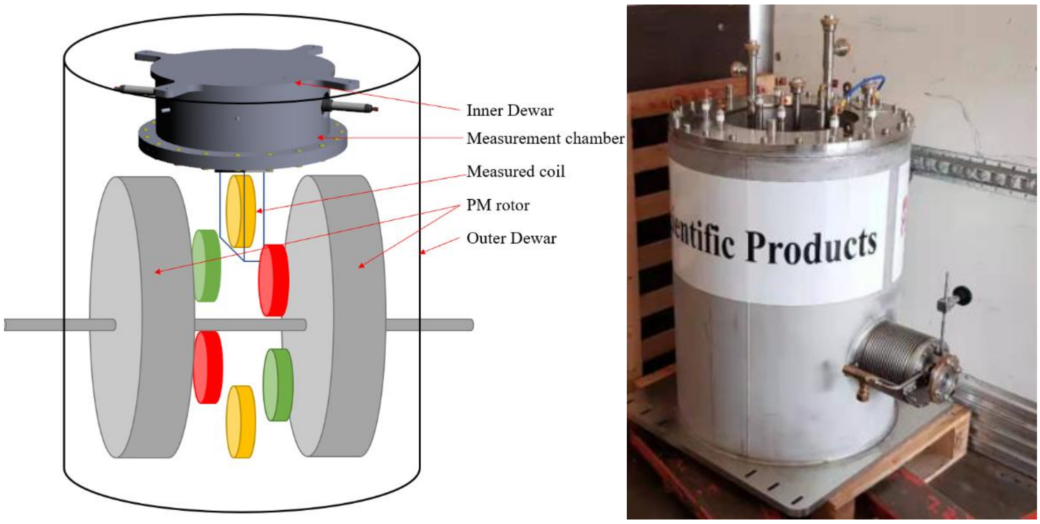

Figure 3.2. Topological structure (left) and figure of the testing machine (right).

3.2.2.1 Rotor magnetic field distribution

Firstly, remove the stator plate, then a Hall sensor array, including six Hall sensors, was inserted into the air gap to measure the rotor field, as shown in Figure 3.3 (left). The distance between the two Hall sensors is 1 cm. Hall sensor NO.0 indicated the centre magnetic field in the coil, and the red circle indicated the position of the stator coil. The measured magnetic flux density shows in Figure 3.3 (right). A peak 0.45 T magnetic flux density was measured.

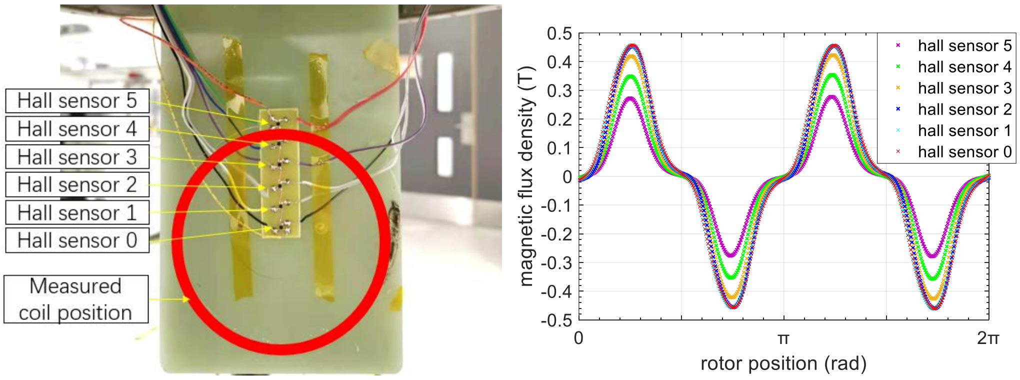

Figure 3.3. Hall sensor array (left) and rotor magnetic field distribution (right).

3.2.2.2 Stator coil magnetic field distribution

The magnetic field generated by the other five stator coils may also influence the measured HTS coil. In this case, the Hall sensor array was set to measure the magnetic field around one stator coil. The inner diameter of the HTS coil is 98 mm and the outer diameter is 103 mm. The copper coil is wound with 16 AWG wire and the total number of turns is 60 (12 turns per layer).

When current is applied in one stator coil, use a set of Hall sensors to measure the magnetic flux density. Figure 3.4 illustrated the measuring results for the magnetic flux density distribution inside one stator coil when applied a DC current of 40 A in the stator coil.

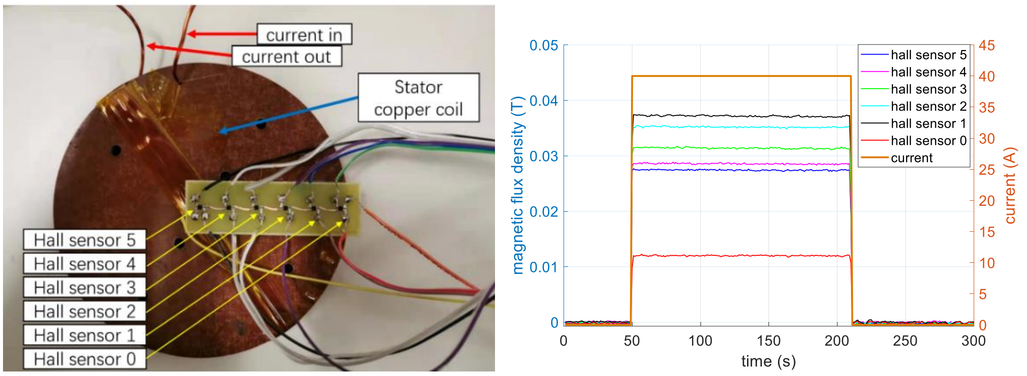

Figure 3.4. The magnetic field distribution for one stator coil (inner).

Figure 3.4 illustrate the measuring result for the magnetic flux density distribution outside the stator coil.

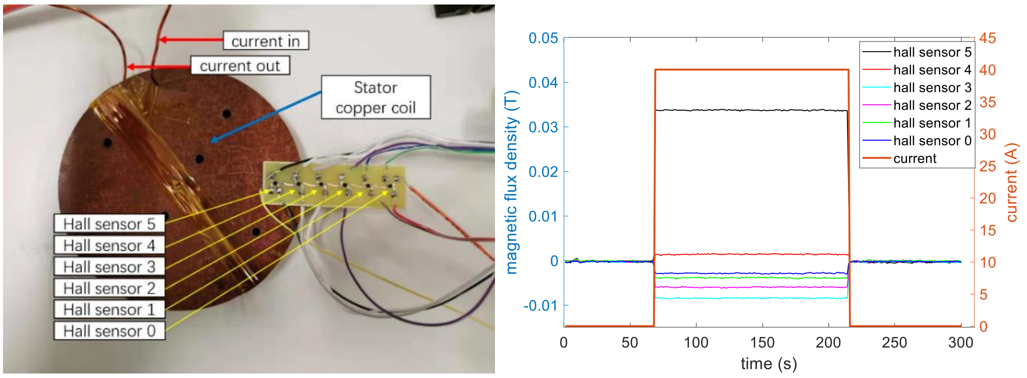

Figure 3.5. The magnetic field distribution for one stator coil (outer).

A COMSOL model was also developed to calculate the coil surface magnetic flux density. As shown in Figure 3.6, the maximum flux density is near the outermost turn of the coil, and the magnetic flux density is less than 0.06 T. The simulation results have a good agreement with the measurement, as shown in Figure 3.7.

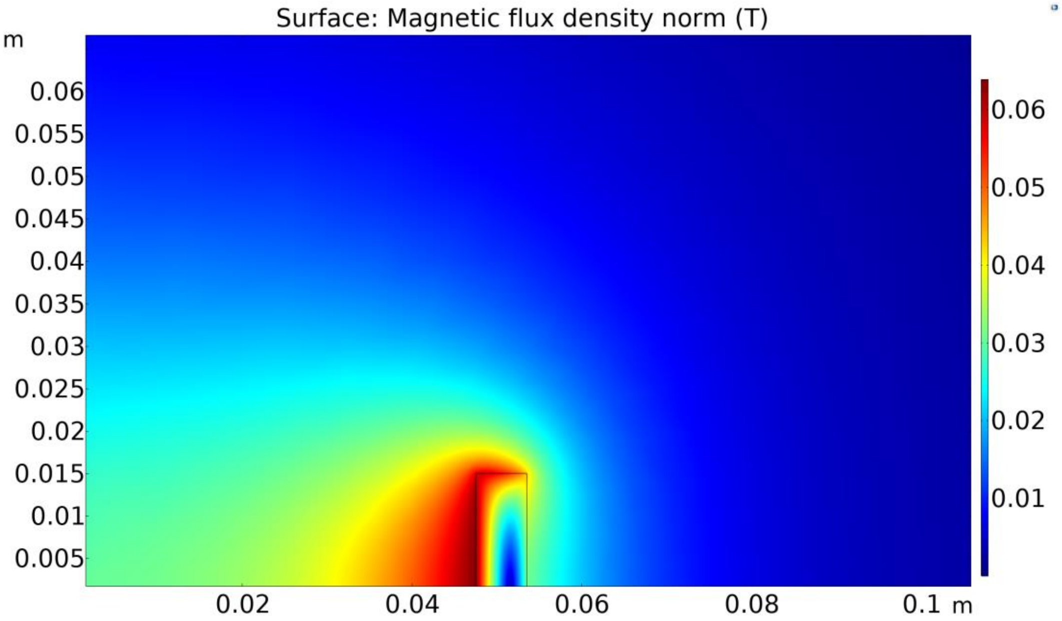

Figure 3.6. The magnetic field distribution simulation.

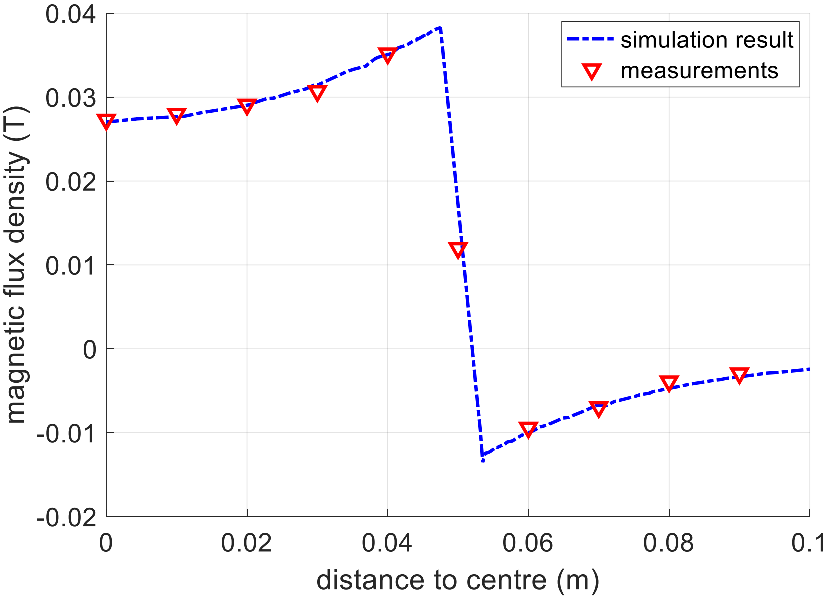

Figure 3.7. Copper coil surface magnetic field simulation results versus measurement.

According to the coil magnetic field distribution results, the measured HTS coil will suffer from the nearby stator coils' AC magnetic field. However, the maximum amplitude is only 0.005 T as shown in Figure 3.8. It is far less than the air-gap flux density of 0.45 T. Thus, in further study, the influence of other stator coils is ignored.

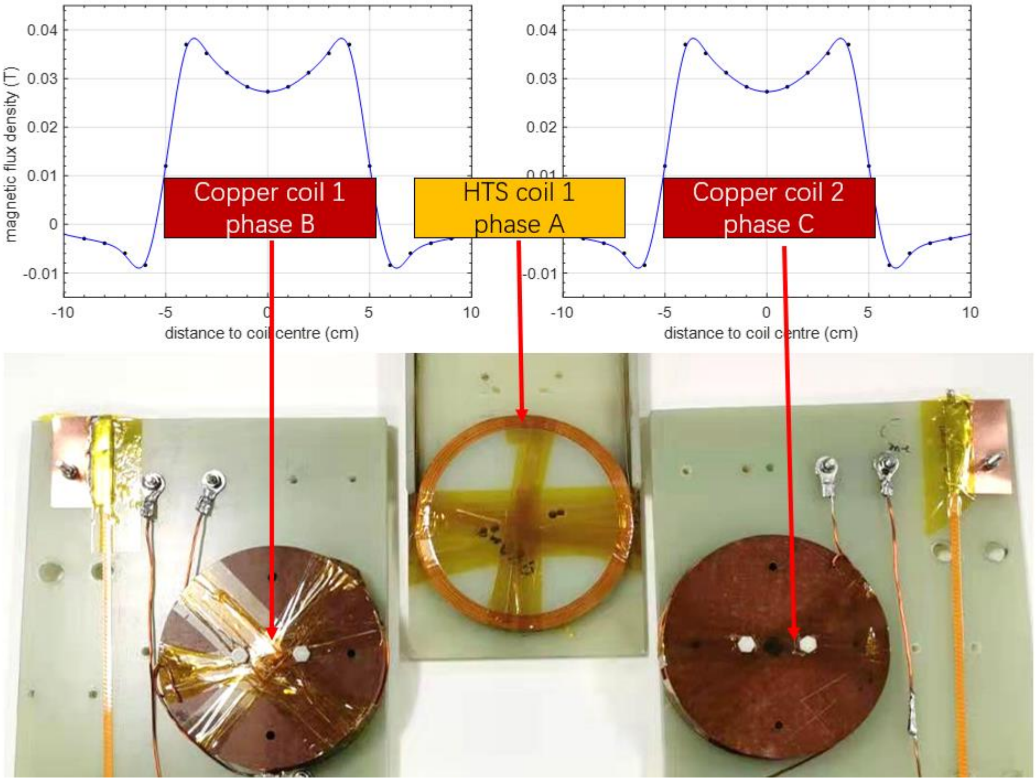

Figure 3.8. Magnetic field distribution in the stator.

3.3 The axial-flux HTS machine platform design

3.3.1 Machine design

To enable the LN_2 boil off measurement inside a rotational machine, we have chosen the axial-flux machine design in order to accommodate a measurement chamber for an HTS stator winding. This machine contains two four-pole permanent magnet rotor discs, two silicon steel back iron and a three-phase HTS stator. Each rotor disc consists of four big NdFeB permanent magnets (100 mm in diameter) sitting on a laminated silicon steel plate. The HTS stator disc is sandwiched between two rotor discs and consists of 6 stator coils, only two coils of phase *A* is made by HTS material as shown in Figure 3.12, phase *B* and phase *C* are made by copper coils with the same diameter. The measurement coil was placed in a separate measurement chamber with liquid nitrogen. The testing platform as shown in Figure 3.9 (left), the outer diameter of the machine is 610 mm and the height is 800 mm. the total weight of the machine is around 400 kg. This machine is driven by a DC motor with a universal joint. Figure 3.9 (right) demonstrates the structure of the stator.

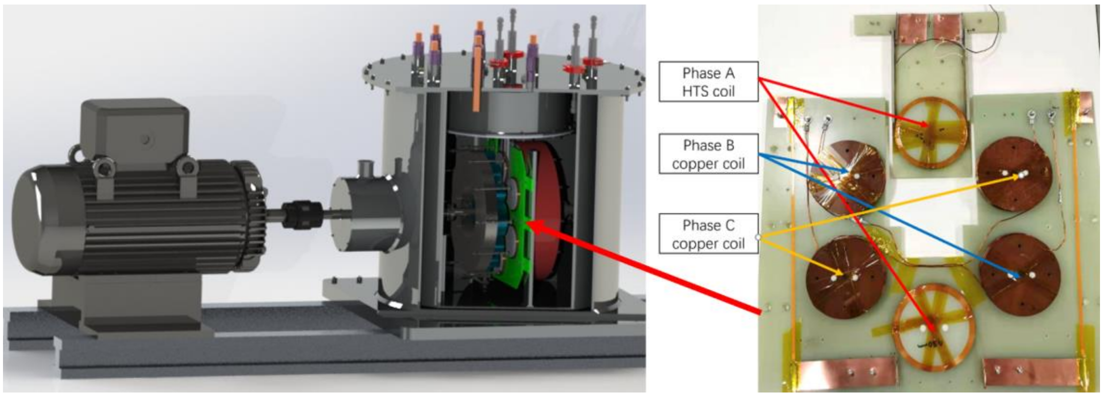

Figure 3.9. Structure of the measurement chamber.

The machine is located in an LN_2 cryostat with a rotational seal. Due to the limitation of the bearings, this machine is designed to operate at a speed of 300 RPM, which means a 10 Hz three-phase voltage output. A hall sensor was placed across the air gap in order to measure the magnetic field in the coil centre, the peak magnetic flux density of 0.45 T was measured in the centre, as shown in Figure 3.10 (a). The phase A voltage was generated by 2 HTS coils, the voltages of phase B and C were generated by copper coils. The peak voltage of HTS is slightly higher due to the inductance difference between HTS material and copper (copper coil inductance = 526.4 μH while HTS coil inductance = 937.4 μH, measured by RLC meter), the inductance difference between HTS coil and copper coil is due to number of turns and geometry difference. By analysing the spectrum of each phase voltage by FFT calculation, only the 3rd harmonic with a small amplitude exists in stator windings due to the magnetic field distribution as well as the non-linear performance of the silicon steel. The 3rd harmonic can be removed by star connection. Thus this machine can provide a good sinusoidal voltage, as shown in Figure 3.10 (b).

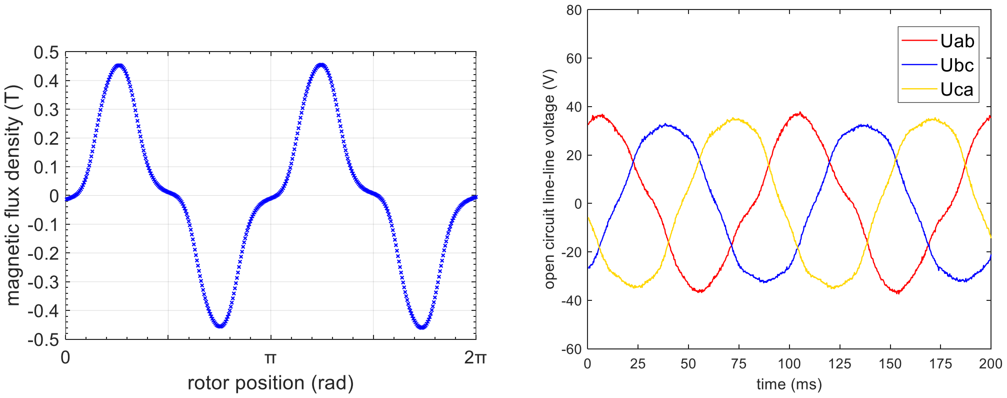

Figure 3.10. (a) Measured magnetic flux field distribution; (b) 3-phase line-line open-circuit voltages.

3.3.2 Cryostat design

A dedicated measurement chamber was designed to measure the boil-off rate of liquid nitrogen coming from the total AC loss of HTS stator coils, as illustrated in Figure 3.11. Only one HTS stator coil is placed in the measurement chamber. It is connected to a flow meter to measure the flow rate of nitrogen gas. The measurement chamber is fully emerged in LN_2 to minimise heat transfer. Both rotor and stator are fully emerged in liquid nitrogen during operation. In an ideal situation, there is no heat transfer between the two chambers. The only conducting component inside the measurement chamber is the HTS stator coil, which makes sure that the boil-off of liquid nitrogen is only due to the total AC loss of the HTS coil.

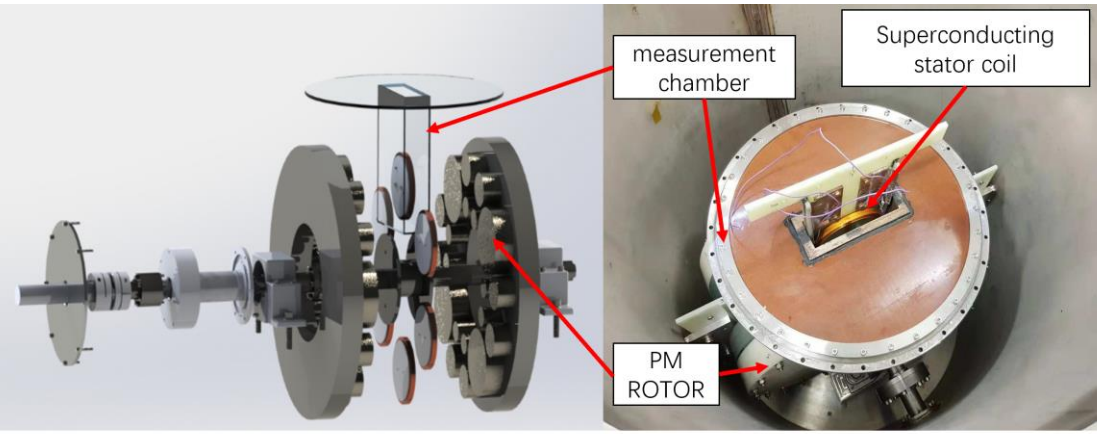

Figure 3.11. Measurement chamber configuration.

The nitrogen gas flow rate is measured by a flow meter (Omega FMA 2710). Theoretically, the latent heat for liquid nitrogen is 160.6 J/mL [107], which equals to

0.25 standard litre per minute for every Watt of power (SLPM/W). Total AC loss of T can be calculated by Equation 3.1 [101].

$$Q = \int_T \frac{F(t)}{K} dt \tag{3.1}$$

Where Q (Joule) is the total heat produced in the measurement chamber for a duration of T, $F(t)$ is the flow rate of nitrogen gas boiled off in the measurement chamber measured by a flow meter. $K = 0.256$ (Litre/min/Watt) is the flow rate constant. When the HTS machine is operated in a steady state with a fixed frequency f, $F(t)$ in Equation 3.1 is simply a constant value with a very small fluctuation. After calibration procedures, we can calculate coil AC loss accordingly. Firstly, measuring the nitrogen gas's total flow rate, calibrating all the error parts out, and calculating AC loss.

3.3.3 System setup

The whole system setup is illustrated in Figure 3.12. The separately excited DC motor is driven by 2 DC power supplies. During the measurement, the HTS rotors are driven by a DC machine to rotate. The HTS stator coil is connected to a load bank, generating three-phase electricity. The LN_2 level in a cryostat is observed by 4 PT100 temperature sensors, LN_2 boil-off flow rate is recorded by a flow meter, all data were recorded by a NI^{TM} *DAQ* system. The HTS machine performance, including coil voltages, coil currents, motor speed, flow meter data and LN_2 level are illustrated in a status monitor.

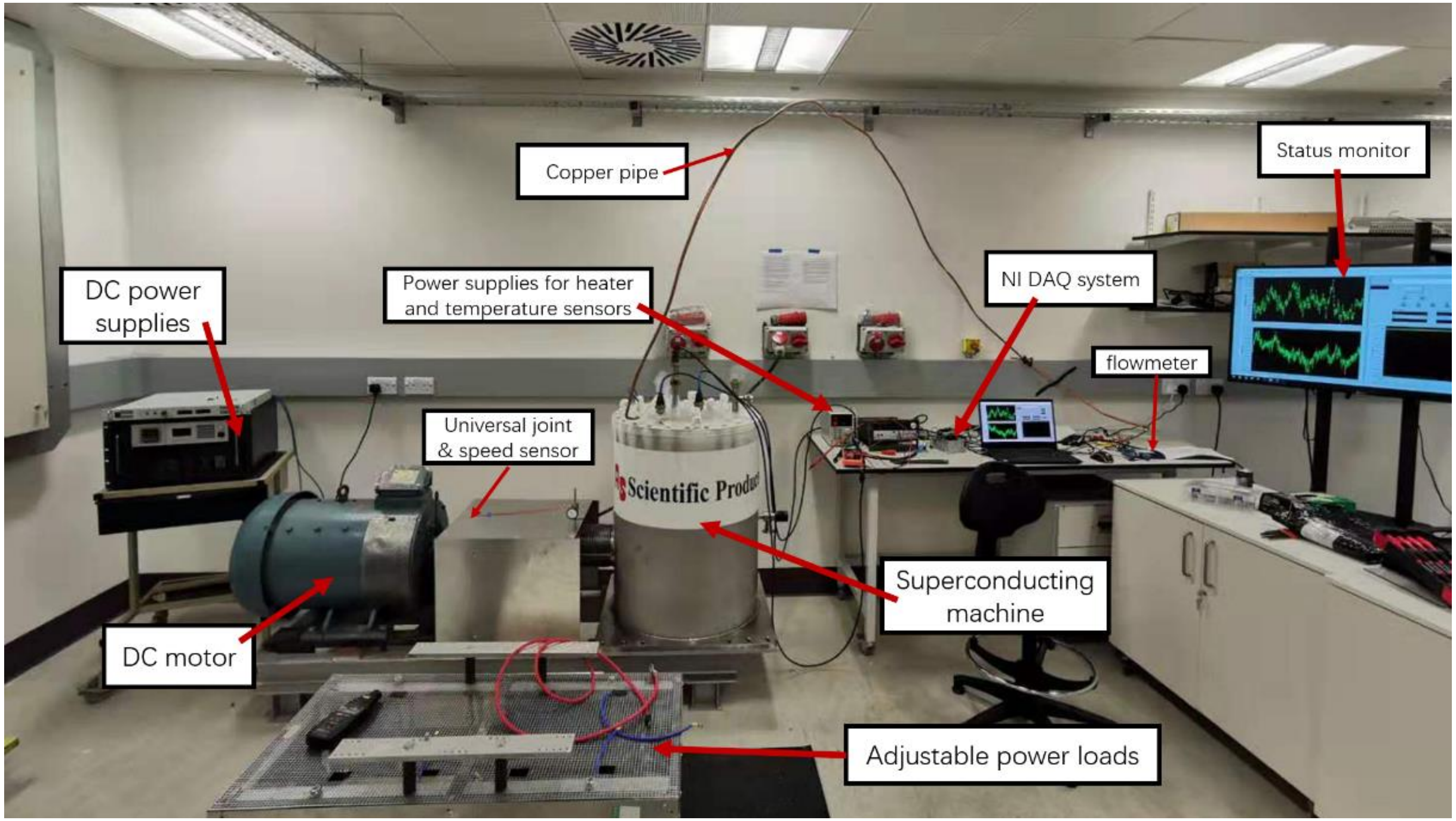

Figure 3.12. Total HTS machine system configuration.

3.4 System calibration and validation

According to the platform setup, the total heat input to the measurement chamber consists of the following parts in Equation 3.2.

$$Q_{total} = Q_{HTS} + Q_{background} + Q_{rotation} + Q_{ter\min al} \tag{3.2}$$

Where Q_{total} refers to the total heat produced in the chamber, Q_{HTS} refers to the heat caused by the HTS coil AC loss, $Q_{background}$ refers to the unavoidable heat leakage in the system, $Q_{rotation}$ refers to the thermal balance condition change when liquid nitrogen was stirring by the rotor and the Joule heat produced by other stator coils, $Q_{ter\min al}$ refers to the Joule heat caused by copper terminal and solder joint resistance between HTS and copper current leads. These losses in Equation 3.2 can be quantified by a set of calibration procedures.

In the calibration procedures, the HTS coil in the measurement chamber was replaced by a very short HTS tape between two copper terminals. One heater made of Kanthal resistance wire (26.4 ohms) was placed in the system, as shown in Figure 3.13 (a). Figure 3.13 (b) demonstrate the normal measurement setup with an HTS coil.

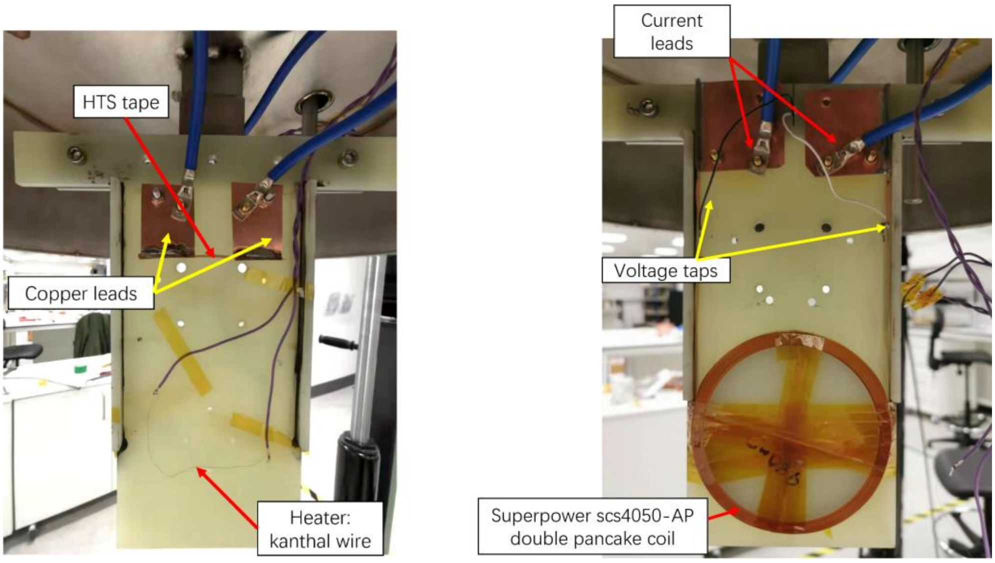

(a) calibration setup, without HTS coil

(b) measurement setup, with HTS coil

Figure 3.13. Setup in the measurement chamber.

3.4.1 $Q_{background}$ measurement

Before the calibration starts, liquid nitrogen completely filled both the measurement chamber and the outer cryostat, ensuring the system was cooled down to 77 K. The flow meter (Omega™ FMA 2710) is connected to the measurement chamber via a long copper pipe. When the rotor is static, a background flow rate refers to $Q_{background}$ in Equation 4.3 was measured, the flow rate was measured for 3000 seconds, the result of the flow meter as shown in Figure 3.14, the background flow of 1.1 SLPM was observed. According to Equation 3.1, the background heat power is 4.29 W due to heat leakage and environmental radiation.

Figure 3.14 illustrated background flow rate can be regarded as a constant value in a short time. $Q_{background}$ can be calibrated out by subtracting the background flow rate.

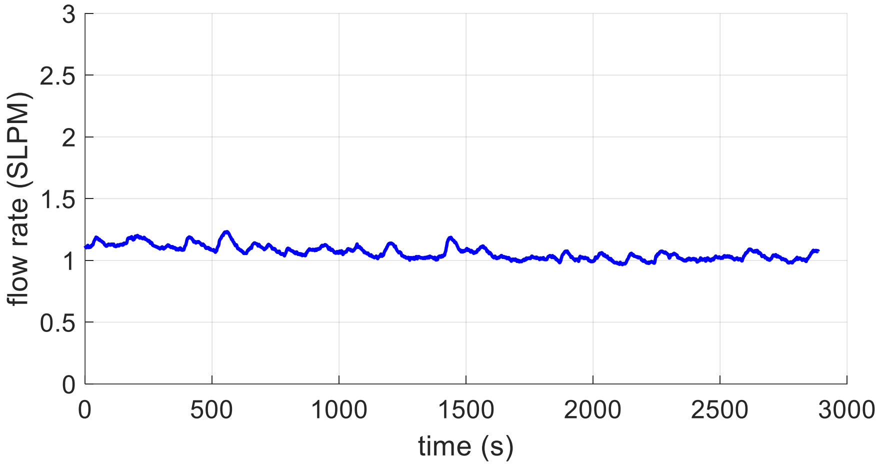

Figure 3.14. Background flow rate data.

3.4.2 $Q_{terminal}$ calibration

As shown in Figure 3.13 (b), two terminals of the HTS coil were soldered to 2 copper current leads, and then connected to 2 copper bars to fed through in the top flange, so there exists resistance in copper bars and copper current leads and also a contact resistance in the solders between the HTS tape and the copper current leads. When there is a transport current, there is a $Q_{terminal}$. The impact of terminal resistance can be measured by shorting two copper terminals. In this measurement, the HTS coil was replaced by a short HTS tape, as shown in Figure 3.13 (a). A 6 cm HTS tape was soldering between two copper current leads. A DC power supply was connected from the outside and then provides a current from 0 - 80 amps. Figure 3.15 shows the results of the flow rate induced by various DC current applied to the current leads.

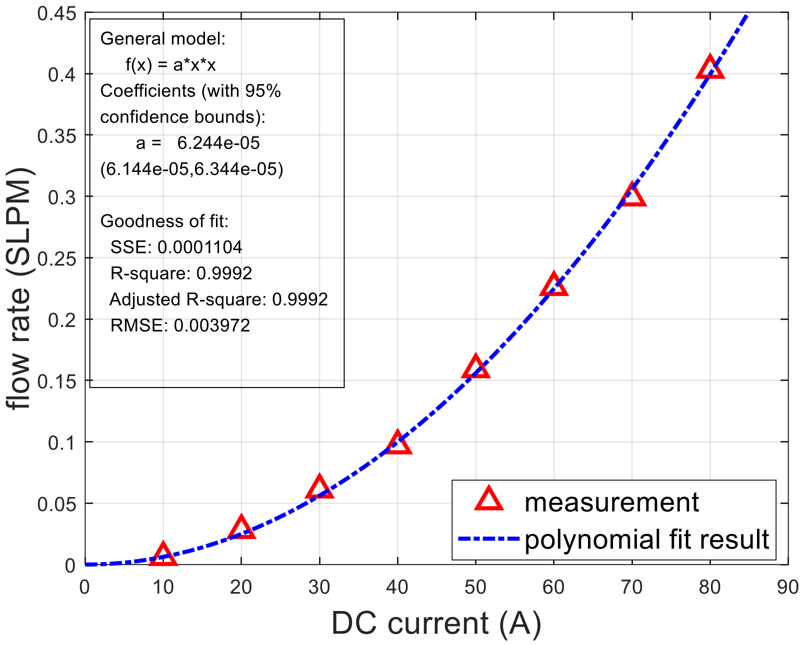

Figure 3.15. Plots of the flow rate induced by various DC current applied to the current leads.

According to Equation 3.1, the heat power (watt) can be expressed in Equation 3.3.

$$I^2 R_{terminal} = \frac{\Delta F}{K} \tag{3.3}$$

Where I is a constant DC current, $R_{terminal}$ is terminal resistance, ΔF refers to a calibrated flow rate (subtracting the $Q_{background}$ flow rate 1.1 SLPM from total flow rate), K is the flow rate constant (0.256 SLPM/W in our setup). Thus, a terminal resistance of 0.243 mΩ was calculated and needed to be calibrated out by Equation 3.4.

$$Q_{terminal} = 2.43\times 10^{-4} I^2 t \tag{3.4}$$

Where $Q_{terminal}$ is Joule heat by terminal resistance in the duration of t, I is transport current.

3.4.3 $Q_{rotation}$ calibration

When the HTS machine is fully operated, the rotor speed is 300 RPM, the peak AC phase current in the stator is 40 A. The rotation of the rotors will stir liquid nitrogen in the outer cryostat and change the heat transfer balance. This may cause the flow rate to change in the measurement chamber. As for stators, phase *B* and phase *C* are copper coils, and the current will generate Joule heat. Although the measurement chamber is made of Tufnol, which is good thermal isolation material, some heat may still transfer to the inner cryostat and cause the flow rate to change.

The rotor speed calibration was operated with open-circuit stator windings. Thus there is no current in the stator, and the rotor speed was measured between 0 to 300 RPM, keep each speed more than 20 minutes. A fluctuation level lower than 0.08 SLPM was observed, we record 9 data as Figure 3.16 shown. When speed increased from 0 to 300 RPM, the flow rate decreased from 1.07 SLPM to 0.83 SLPM. Heat transfer is balanced when the rotor speed is steady, when liquid nitrogen was stirred by the rotor, some liquid nitrogen cooling the top plate and the foam insulation, causing the system to proceed to a new thermal balance condition. With the rotor speed increase, the temperature difference between the measuring chamber and the top plate is decreased and cause a lower background flow rate. Thus, the error caused by rotor speed can be calibrated out by Figure 3.16.

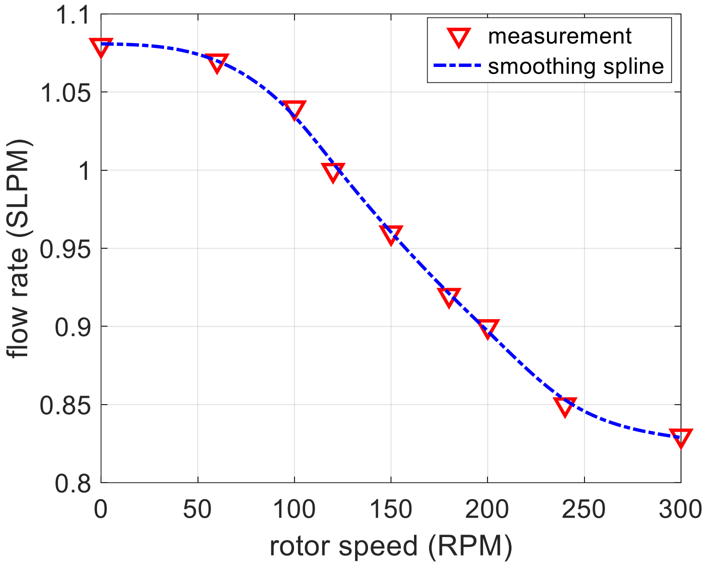

Figure 3.16. Rotor speed calibration.

The stator is designed to operate at a peak phase current of 40 amps. Thus stator calibration is simply kept rotor static, and no input power to inner cryostat, applied currents in all five stator coils in the outer cryostat, record the flow meter data. The results were shown in Figure 3.17. The red curve illustrated the DC current applied to the stator, and the blue line illustrated the flow rate during this time. As we can see from the results, the flow rate does not change when the different current applied in the stator, and Figure 3.17 proves that good thermal isolation of the Tufnol material and the transfer heat is very small, resulting in no influence on the flow rate from stator's Joule heat. Thus, $Q_{rotation}$ is only caused by rotor speed and can be calibrated out by Figure 3.16.

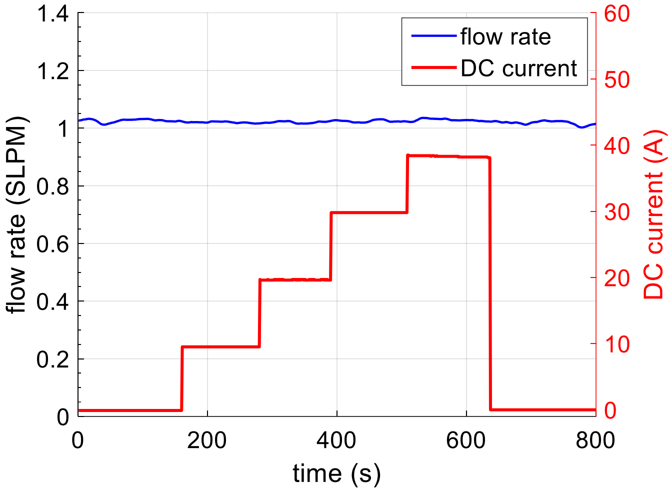

Figure 3.17. The stator coils current calibration.

3.4.4 The measurement chamber calibration

Theoretically, the flow rate constant equals to 0.25 standard litre per min per watt (SLPM/W). A resistance wire of 26.4 ohms (in liquid nitrogen) was placed in the measurement chamber and connected to a DC power source. In the heater calibration procedure, various DC voltages from 0 - 25.2 V were applied in the experiments. Eight points were selected from 3.38 watts to 24.16 watts. Figure 3.18 (a) demonstrated the results of flow rate (subtracting the background flow) induced by carious heating powers applied to the resistance wire. The red curve shows the heater power level, and the blue curve shows the flow rate after calibrated. Plots these data in one figure as shown in Figure 3.18 (b), the results show the flow rate proportional to heating power in the measurement chamber, the curve gives a ratio of 0.256 SLPM/W refers to flow rate constant, these experimental results show that the actual performance is accordant with the theoretical value with only 2.4% error. On the other hand, Figure 3.18 validates the system that there was no gas leakage in the measurement chamber. As the fluctuating range of the flow meter is less than 0.08 SLPM, which gave a measuring error up to 0.3 W.

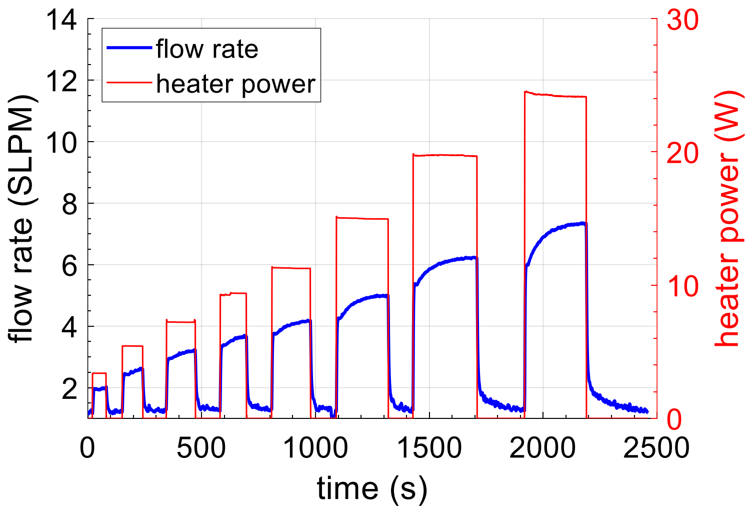

(a) Data of flow rate and heater power

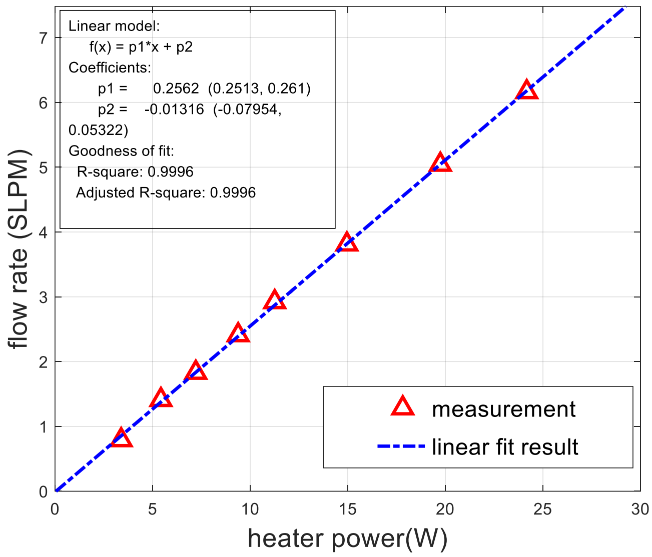

(b) Flow rate versus heater power

Figure 3.18. Background flow rate data.

To sum up, all the errors have been estimated and well-calibrated. The sensitivity of this testing rig is near 0.3 W, and this value makes sense in the platform based on the calorimetric method.

3.5 Conclusions

The platform is verified and validated for AC loss measurements. However, uncertainties do not make a significant percentage error, as observed the whole error level is less than 0.3 Watts (0.08 SLPM), the results are more accurate when applying higher current and higher frequencies, as HTS machine application is normally required to carry a high current (near its critical current value). Thus this platform can give experimental results in machine design.

This chapter reports a pioneering testing platform for fully HTS machines used for future electric aircraft machines. The system provides a machine environment to measure AC loss of HTS windings. This system was carefully calibrated and validated. Focusing on calorimetrically quantify the electrical HTS stator, the platform will provide valuable insights into the AC losses of the HTS stator in a rotational machine environment. The platform can be used to identify AC loss reduction technologies, contributing to the development of a highly efficient fully HTS propulsion machine.

Chapter 4 NI coil for HTS rotor design

High-temperature superconductor (HTS) machine is a promising candidate for electrical aircraft propulsion due to its great advantage in high power density. However, the HTS machine always suffers the problem of low thermal stability during a quench. In this chapter a no-insulation (NI) coil was applied on the rotor windings of HTS machines to enhance the stability and safety of the electrical aircraft. The NI HTS rotor windings experience ripple magnetic fields, which leads to induced eddy currents through turn-to-turn contacts. This induced current and accompanying losses will considerably affect the practicality of this technique. To study this issue, an equivalent circuit network model is developed, and it is validated by experiments. Then, analysis using this model shows that most of the induced current flows in the outermost turns of the NI HTS coil because of skin effect, and lower turn-to-turn resistivity leads to higher transport current induced and more significant accumulation of turn-to-turn loss. A grading turn-to-turn resistivity is proposed to reduce the transport current induced and ac loss accumulation and meanwhile keep the high thermal stability of the NI HTS coil. Optimization of turn-to-turn resistivity is required when the NI HTS coil is applied in the machines' environments.

4.1 Introduction

This chapter aims to investigate the influence of ripple magnetic fields in machines on the electromagnetic behaviour of NI HTS NI coils numerically and experimentally, in order to investigate the practicability of NI HTS machine design. Since the current can flow along any direction in the NI HTS coils, an equivalent circuit modelling method is developed to calculate the current and loss of NI HTS coils exposed in the ac ripple background magnetic field. An NI HTS coil is wound by REBCO tapes for the test, and a copper solenoid is wound to generate the background ripple magnetic field. Then, the NI HTS coil is exposed in the ripple magnetic field and its electromagnetic behaviour is tested. Results from simulation and experiments are compared to validate the model. Then, the distribution of induced eddy current and ac loss is analysed using this model, and the influence of turn-to-turn resistivity, field frequency, and amplitude on the eddy current is also discussed.

The key idea of the NI coil is to remove the turn-to-turn electrical insulation of traditional insulated coils. Transport current can bypass the local hot spot through turn-to-turn metallic contacts so that the quench propagation is prevented and enhanced thermal stability is achieved, which has been validated by both experiments and simulations [55, 141-143]. Another advantage of the NI HTS coil is the enhanced power density because the elimination of turn-to-turn insulation increases the current density of the HTS windings. Therefore, it is promising to improve the thermal stability and prevent quench damage of HTS windings in machines of electrical aircraft by applying the NI technique [57].

The application of HTS windings on the rotor can significantly increase magnetic fields at air gaps so that the power density of the machine is increased. In synchronous machines, the rotation speed of fundamental fields generated by stator windings is the same as the rotation speed of the rotor, and thus, the HTS rotor windings are stationary relative to fundamental fields [38, 144, 145]. If NI HTS coils were applied on rotors, the ripple field may have a considerable influence on the electromagnetic behaviour of NI HTS coils due to the absence of turn-to-turn insulation, such as induced eddy current and extra loss on turn-to-turn contacts [124, 128]. This has never been studied thoroughly, which may be a great challenge for the thermal stability and efficiency of HTS machines with NI coils.

The original circuit network model of the NI coil is developed by Dr Yawei Wang in 2015 [146], we developed an advanced model to study the performance of the NI coil in a small ripple magnetic field which is demonstrated in Chapter 4.2. My other contribution is to design, build and test an experimental platform to validate the simulation model, as shown in Chapter 4.3, and the discussions are given in Chapter 4.4 in detail.

4.2 Numerical model

4.2.1.1 Circuit Model of 2G HTS Tape

The 2G HTS REBCO tape is a coated conductor with high aspect, as shown in Figure 4.1 (a) and Figure 4.1 (b). It has multiple layers, and the superconducting layer is covered by metallic layers (brass, copper, silver, and Hastelloy), as shown in Figure 4.1 (b) [50]. The resistance of the superconducting layer is nearly zero below critical current Ic, and it increases dramatically when the current is higher than the critical current. It can be calculated from the E–J power law of the ReBCO conductor [147].

$$E = E_0\left(\frac{J}{J_c}\right)^n \tag{4.1}$$

Where Jc is the critical current density, $E_0 = 1$ μV/cm, and $n = 30$. During overcurrent operation, some current is forced to flow in metallic layers, and thus, the equivalent circuit model of the REBCO tape can be two parallel resistances: resistance of superconducting layer R_{sc} and normal resistance of metallic layer R_n, as shown in Figure 4.1 (c).

For the REBCO tape used in this study, its width is 4.1 mm and its total thickness is about 250 μm. The average electrical conductivity of all the metallic layers is about 9.7×10^7 S at 77 K in this study. The critical current of the tape is 190 A at 77 K, and its U–I relationship is shown in Figure 4.2, which is obtained from the circuit model in Figure 4.1 (c). All the transport current flows in superconducting layers below the critical current since the resistivity of the superconductor is nearly zero. The Joule loss is increasing exponentially during overcurrent due to the current redistribution to metallic layers.

4.2.1.2 Equivalent Circuit Model for NI HTS Coils

The NI HTS coil is often wound with a pancake structure, as shown in Figure 4.3 (a). When the NI coil is operated in the dc environment, all the transport current follows along the azimuthal direction, and the metallic layers serve as turn-to-turn insulation since the resistivity of the superconducting layer is much lower than the metallic layer. When the NI HTS coil is exposed to ac ripple magnetic fields, eddy current can be induced in the coil, and some current can flow along the radial direction through the turn-to-turn contacts. This induced eddy current and losses may significantly affect the thermal stability and efficiency of the HTS machine, which is to be studied.

An equivalent circuit model is developed to study the distribution of the induced eddy current as well as turn-to-turn loss in the NI HTS coil, as shown in Figure 4.3 (c). In this model, the current is decomposed to the azimuthal component i and radial component *j*. Each turn of the coil is subdivided into a fine arc element, and each element is equivalent to a lumped circuit model. The whole coil is equivalent to a distributed circuit network [58, 148-150], as shown in Figure 4.3 (c). Each dependent current node has four current branches, two azimuthal branches and two radial branches, in which the governing equation can be derived from Kirchhoff's current law. Each dependent circuit mesh also has four current branches, two radial branches and two azimuthal branches, in which the governing equation can be derived from Kirchhoff's voltage law. The two radial branches represent the resistive voltage generated on turn-to-turn contacts. Therefore, the governing equation of this network model can be expressed as:

$$\begin{cases} \sum_k i_k + \sum_k j_k = 0 \\ u_k - u_{k+n_e} - j_{k-1}\dfrac{\rho_r}{S_{r,k-1}} + j_k \dfrac{\rho_r}{S_{r,k}} = 0 \end{cases} \tag{4.2}$$

Where i_k and j_k are the azimuthal and radial current, respectively, $S_{r,k}$ is the radial surface of arc element, ρ_r is the equivalent radial resistivity with a unit of μ·cm^2 [61], which is obtained in the following measurement, and u_k is the voltage of the kth azimuthal branch, including the resistive voltage and inductive voltage.

The background magnetic field can be replaced by equivalent virtual coils in this network model, as shown in Figure 4.3 (b). Then, the influence of the background field can be represented by coupling through the mutual inductance M_e, as shown in Figure 4.3 (c). Therefore, the inductive voltage of u_k has two parts: one is from the coil itself, and the other one is from the virtual external coil:

$$u_k = \sum M_{k,l}\frac{di_k}{dt} + M_{ek}\frac{dI_e}{dt} + V_{R,k}(i_k, I_c) \tag{4.3}$$

Where $M_{k,l}$ is the mutual inductance between two arc elements in the NI HTS coil, M_{ek} is the mutual inductance between the k^{th} arc element and the external equivalent virtual coils, I_e is the transport current of the equivalent virtual coil, the amplitude and frequency of the background field can be changed by adjusting the amplitude and frequency of this current I_e, and $V_{R,k}$ is the resistive voltage of the k^{th} azimuthal circuit branch. Then, the distribution of eddy current as well as losses induced by the external ripple magnetic field can be calculated by solving this numerical model. The simulation model in COMSOL is demonstrated in Figure 4.4.

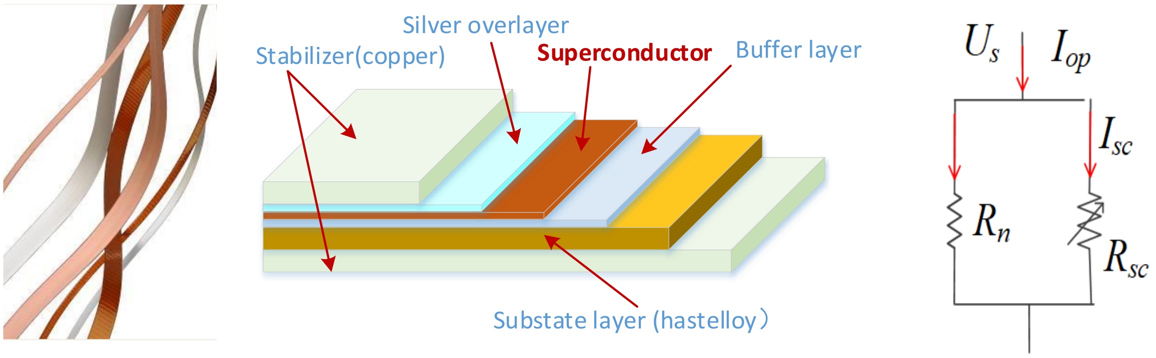

(a) Photo of ReBCO tape (b) Layer structure of ReBCO tape (c) Circuit model for ReBCO tape

Figure 4.1. (a) Photograph of 2G HTS ReBCO tape. (b) Multiple layer structure of the 2G HTS tape. (c) Equivalent circuit model of ReBCO tape.

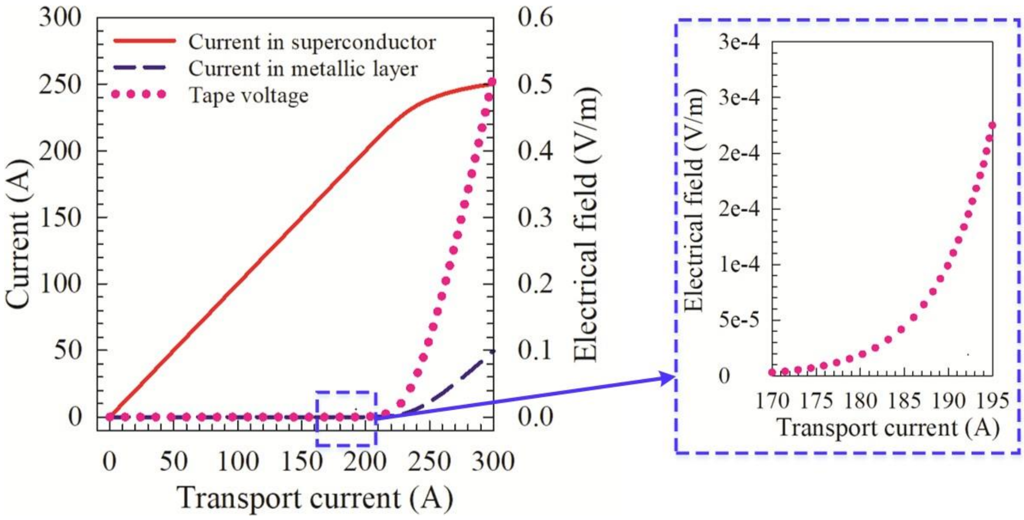

Figure 4.2. U–I relationship of the REBCO tape used in this thesis.

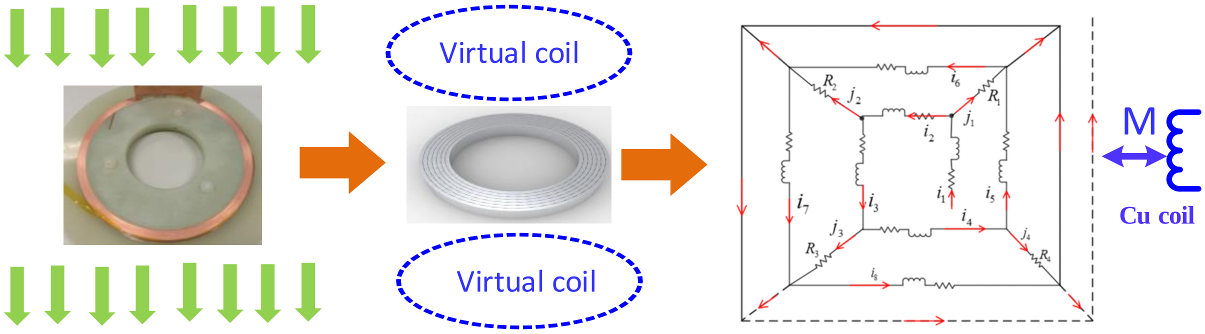

(a) NI HTS coil exposed to ripple magnetic field

(b) NI HTS coil with virtual external coil

(c) Equivalent circuit network model

Figure 4.3. (a) NI HTS pancake coil exposed to background ripple fields. (b) Schematic of NI HTS coil with virtual coils generating the background ripple fields (c) Schematic of the equivalent circuit network model for NI HTS coils exposed to background fields. Notice that each turn is subdivided to four elements in this figure, which is for clear presentation.

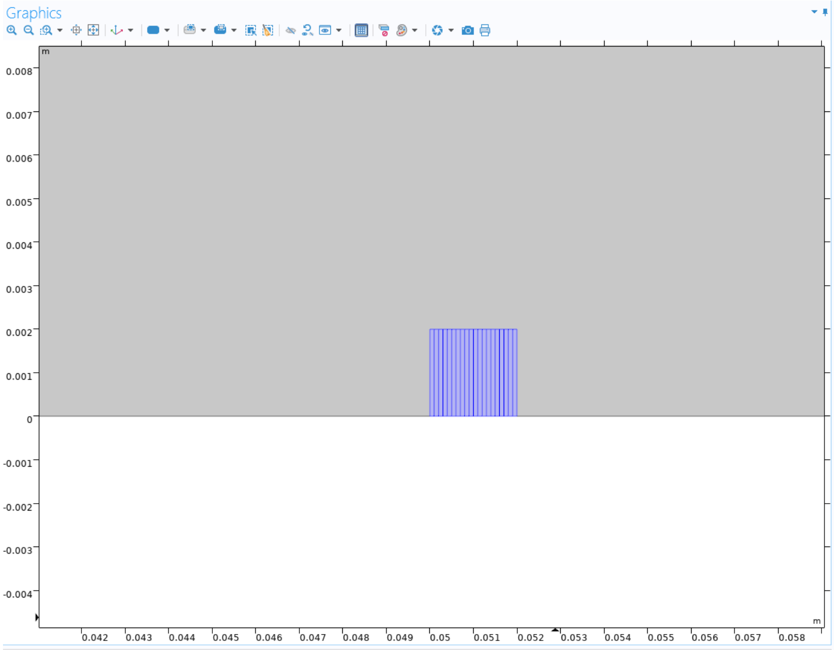

Figure 4.4 Diagram of the simulation model in COMSOL

4.3 Experiments and model validation

4.3.1 Experimental setup

To validate the abovementioned model, an NI HTS coil is wound by REBCO tapes from SuNAM, South Korea, as shown in Figure 4.5 (a). Details of the tape have been shown in Figure 4.1 and Figure 4.2. The tape's critical current at 77 K is 190 A and the coil's critical current is 130 A. The NI coil has a single pancake (SP) geometry, and two copper sheets are used as current leads for the fast discharge test, as shown in Figure 4.5 (a). More details of the coil are shown in Table 4.1. A solenoid copper coil is wound to generate the background ripple magnetic field, as shown in Figure 4.5 (b). It is energized by an AC power supply. Specification of this solenoid is also shown in Table 4.1. During the test, the NI HTS coil is placed at the central position of the copper solenoid, as shown in Figure 4.6, the coil is located 73 mm from the ground due to the position of the screw. And thus, the NI HTS coil is exposed to an ac ripple magnetic field generated by this copper coil. A Hall sensor is placed at the centre of the HTS coil to measure the magnetic field.

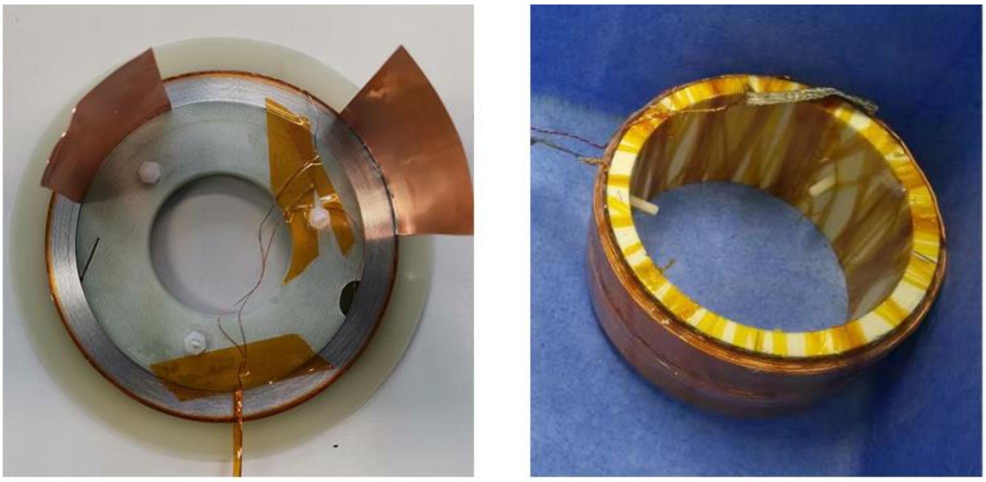

NI HTS coil

Copper coil

Figure 4.5. Photographs of test NI HTS coil and copper solenoid coil.

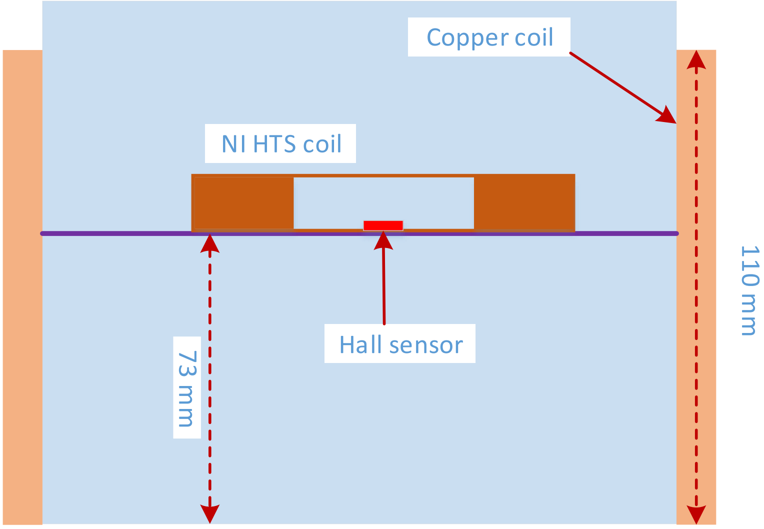

Figure 4.6. Location of the NI HTS coil and copper coil during test.

Table 4.1. Specification of the test HTS coils and copper coil

Parameters	NI HTS coil	Copper coil
Coil type	Single pancake	Solenoid
Inner diameter	100 mm	215 mm
Outer diameter	121 mm	235 mm
Height	4.0 mm	110 mm
Number of turns	45	289
Critical current, @77 K	130 A	/
Inductance	406 μH	18.7 mH
Flux density per Ampere (measured value)	506 μT/A	1.42 mT/A
Tape producer	SuNAM	/
Width/thickness of tape	4.0/0.25 mm	/
Turn-to-turn resistivity	$96.7\ \mu\Omega\cdot\text{cm}^2$	/

4.3.2 Fast discharge test

Turn-to-turn resistivity ρr is a key parameter of NI HTS coil, which distinguishes it from conventional insulated HTS coils. It is also a necessary parameter for the simulation of current distribution in NI coils, as shown in Equation 4.2. Both the HTS coil and the copper coil are immersed in liquid nitrogen during the test. First, fast discharge tests are performed on the NI HTS coil to obtain the turn-to-turn resistivity. During the fast discharge test, the copper solenoid coil is in open circuit, and the NI coil is first ramped to a transport current below critical current and kept at this current for the time long enough to eliminate the charging delay. Then, the current is switched

OFF suddenly by an air circuit breaker, and all the magnetic energy stored in the coil is dissipated in the coil itself. The coil voltage is measured in the process, and its decay is shown in Figure 4.7. Here, the initial stable transport current is 40, 80, and 100 A. The variation of the coil voltage matches the following equation [60]:

$$U = U_0 e^{-\frac{t}{L/R_c}} \tag{4.4}$$

Where U is the coil voltage measured, U_0 is the initial coil voltage, L is the inductance of the coil, and R_c is the equivalent radial resistance. The time constant can be obtained directly from the results in Figure 4.7. The equivalent turn-to-turn resistivity ρ_t with a unit of μ·cm^2 can be calculated by [151]

$$\rho_t = R_c / \sum_{k=1}^{N_t} \frac{1}{2\pi r_k w_d} \tag{4.5}$$

Where N_t is the total number of turns, r_k is the radius of the k^{th} turn, and w_d is the width of the tape. The equivalent turn-to-turn resistivity of the test NI HTS coil is 96.7 μ·cm^2.

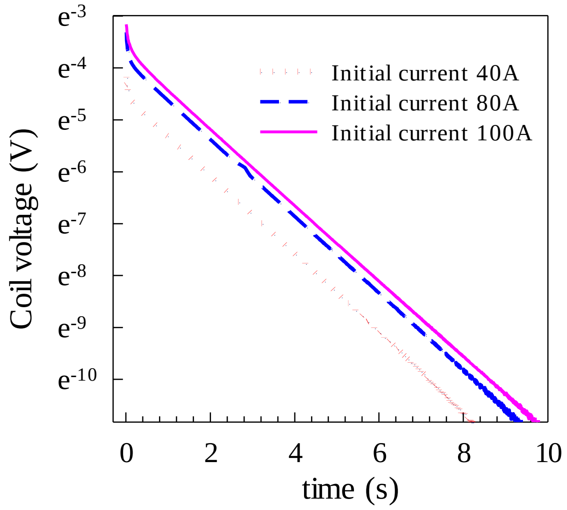

Figure 4.7. Decay of the NI HTS coil's terminal voltage during the fast discharging test.

4.3.3 Model validation

As shown in Figure 4.5, the magnetic field at the coil centre should be lower than the background field generated by the copper coil since the induced eddy current in the NI HTS coil reduces the central magnetic field. Therefore, we can validate the numerical model by comparing the central magnetic fields from measurements and simulations. The NI HTS coil does not carry any transport current, and it is an open circuit during the measurement. The copper leads are removed before this measurement to eliminate the influence of eddy current induced in copper leads. Figure 4.8 shows the variation of magnetic fields at the coil centre when the copper coil is energized by a transport current with an amplitude of 20.66 A and a frequency of 40 Hz. Note that the ripple background field here is that at the same position when there are no NI HTS coils. It is used to represent the background field generated by the copper coil, and its amplitude is 29.3 mT in Figure 4.8. Then, we change the amplitude of the background field and measure the magnetic field at the coil centre under different background ripple fields, as shown in Figure 4.9. The results from the abovementioned model show a good agreement with that from the measurement. The discrepancy between simulation and experiment has two main possible factors. First, the turn-to-turn resistivity used in the simulation is measured from a fast discharge test, and it may change in the following operations, such as removing the current leads and the vibration induced by ripple fields and liquid nitrogen boiling. Second, the turn-to-turn resistivity is assumed uniform among turns in the simulation, while it may vary among turns in fact.

The distribution of the eddy current induced in the NI HTS coil is hard to measure directly in this study. However, this induced eddy current generates an opposite magnetic field at the coil centre. The amplitude of this opposite magnetic field is proportional to the eddy current induced, and its frequency is the same as that of the magnetic field. Therefore, this opposite magnetic field can represent the eddy current induced largely. The model developed is to calculate the current distribution in the NI HTS coil. The opposite magnetic field from this model agrees well with that from measurements, which validates the model largely. A Joule loss is generated on the turn-to-turn contact by the induced eddy current. If the eddy current calculated was reliable, the turn-to-turn loss from this simulation should also be reliable.

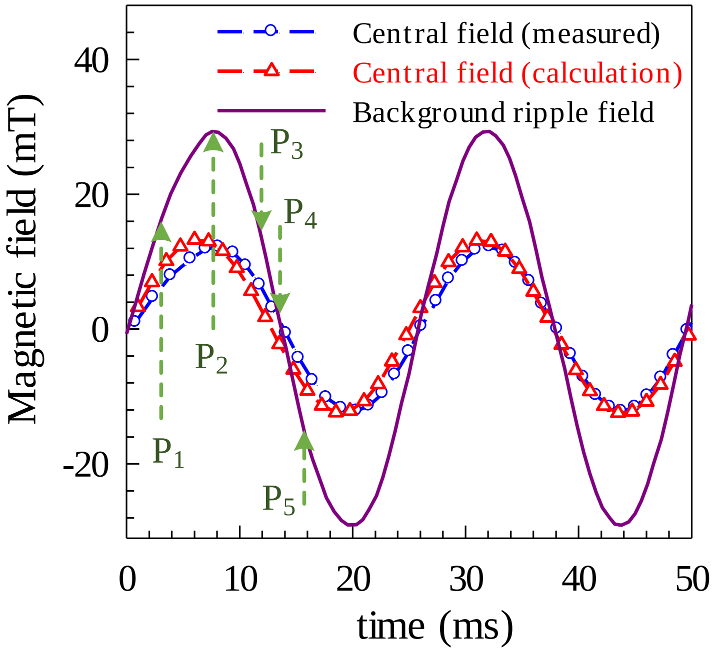

Figure 4.8. Measured and calculated magnetic field at the centre of the NI HTS coil when it is exposed to a ripple background magnetic field with a frequency of 40 Hz.

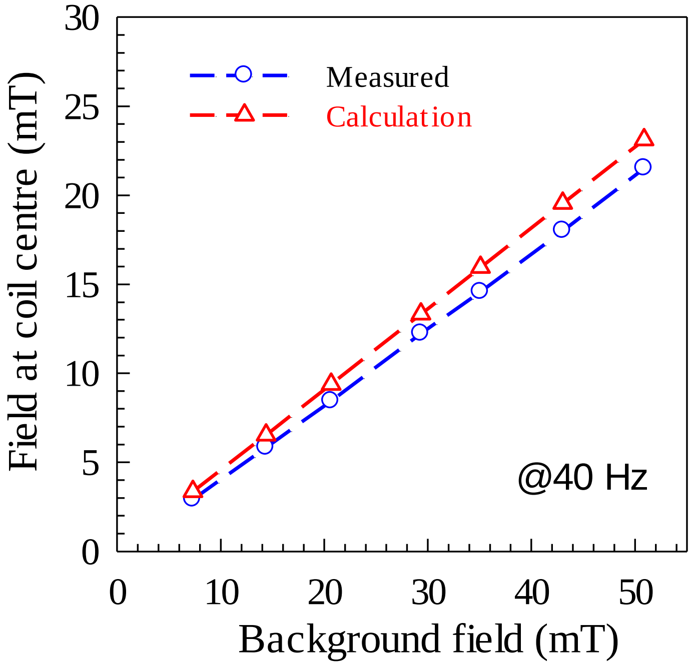

Figure 4.9. Amplitude of magnetic field at the NI HTS centre under different ripple background magnetic fields, the frequency is 40 Hz.

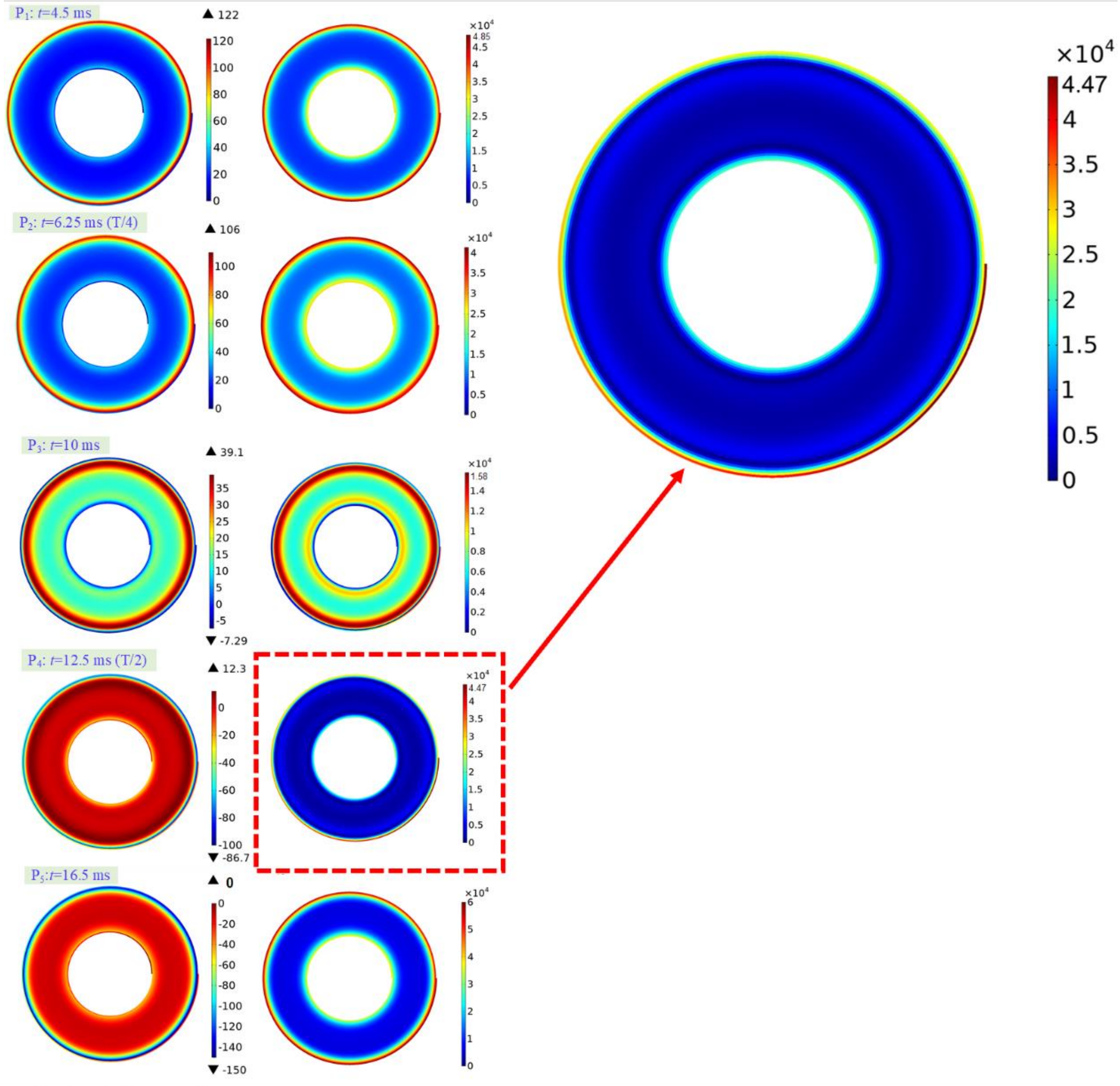

(a) azimuthal current (A) (b) radial current density (A/m^2)

Figure 4.10. Distribution of induced eddy current (azimuthal current and radial current) in the NI HTS coil when it is exposed to ripple background field generated by copper solenoid coil; the background field is 29 mT/40 Hz, and the turn-to-turn resistivity of the NI HTS coil is 96.7 $\mu\Omega \cdot \mathrm{cm}^2$. The thickness of each turn is enlarged 5 times for a better presentation.

4.4 Results and discussion

4.4.1 Induced eddy current and losses

The distribution of induced eddy current is analysed using the abovementioned model developed, as shown in Figure 4.10. Here, five moments P1–P5 are selected during a cycle, as shown in Figure 4.8. The azimuthal current, with a unit of ampere, flows in the superconducting layer below the critical current, and its positive direction is in the anticlockwise direction, as shown in Figure 4.10 (a). The radial current follows through the turn-to-turn contacts, and Figure 4.10 (b) shows the normal value of the radial current density, whose unit is A/m^2 here. We observe a kind of skin effect, where most of the eddy current is generated on the inner and outer turns of the NI HTS coil, especially the outermost turns. This is because the outer turns have a relatively larger diameter, thus coupling more external magnetic flux than other turns. Then, the induced eddy current has a field shielding effect on the middle turns so that less current is induced on middle turns. A transport current is generated on the NI HTS coil (with the open circuit) by the azimuthal current induced and the closed circuit is formed through the turn-to-turn contacts, which leads to the radial current. Thus, the distribution of radial current is almost the same as that of azimuthal current. The induced current shows a uniform distribution along the angular direction of the NI coil, but the current on the outermost turn shows a considerable nonuniform distribution along the angular direction. The zone near the current lead has a higher current than other zones on the same turn.

The maximum transport current (azimuthal current induced) is a critical issue for the HTS coil since the quench risk rises rapidly with the increase of transport current. The transport current in HTS tape has to be below critical current during operations. The results in Figure 4.10 also show that the variation of the transport current induced is not synchronous with the background field. The maximum azimuthal current induced does not occur at the peak point (P2) of the background field, but before these moments, P1 and P5. This is because the induced voltage is generated by the variation of the background field, and it has the highest changing rate at these moments. Therefore, P1 and P5 are the weak moments with higher quench risk for the NI HTS coil. Figure 4.11 shows the azimuthal current induced by higher background fields, and an overcurrent (>190 A) is observed on the outermost turns of the NI HTS coil when the background field is high enough. The penetration depth of induced current increases rapidly with the background field when overcurrent is induced. This is because the resistance of HTS increases dramatically above the critical current, as shown in Figure 4.2, which forces more current to other turns.

Losses are generated by the eddy current induced, which consists of two parts: loss generated by the radial current on turn-to-turn contacts, which is called “turn-to-turn loss” in this study; the loss generated by transport (azimuthal) current is called “azimuthal loss.” The azimuthal current flows in superconducting layers below the critical current, and a magnetisation loss is generated in superconductors by this ac transport current [124, 132]. When the induced transport (azimuthal) current is higher than the critical current (190 A), the resistance of the superconducting layer increases dramatically, some current is forced out to metallic layers, and thus, a huge resistive loss is generated by this overcurrent. Figure 4.12 shows the turn-to-turn loss and azimuthal loss induced by background fields 51 mT/40 Hz. The peak moment of radial loss matches well with the peak moment of the radial current in Figure 4.10. The ac losses should have the same distribution as the eddy current induced. Both the eddy current and losses accumulate on the outermost turns of the NI HTS coil; therefore, the outermost turns have a much higher quench risk than other turns, and special attention is required on this zone during electromagnetic and cooling design.

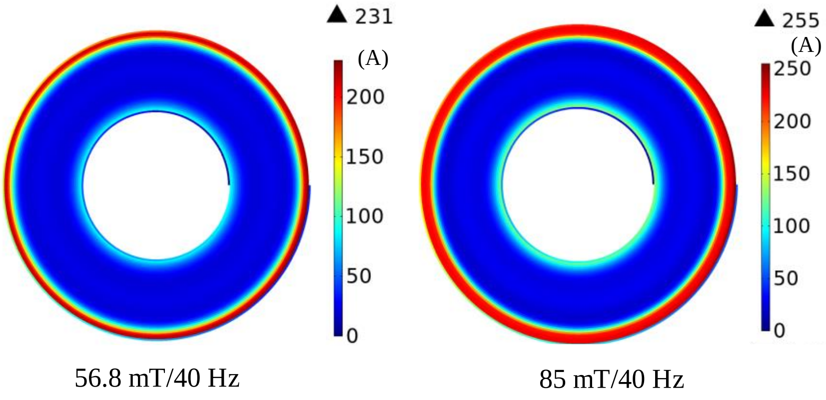

Figure 4.11. Distribution of induced azimuthal current in the NI HTS coil, when it is exposed in higher background fields, 56.8mT/40Hz and 85 mT/40 Hz; the turn-to-turn resistivity of the NI HTS coil is 96.7 $\mu\Omega\cdot\mathrm{cm}^2$.

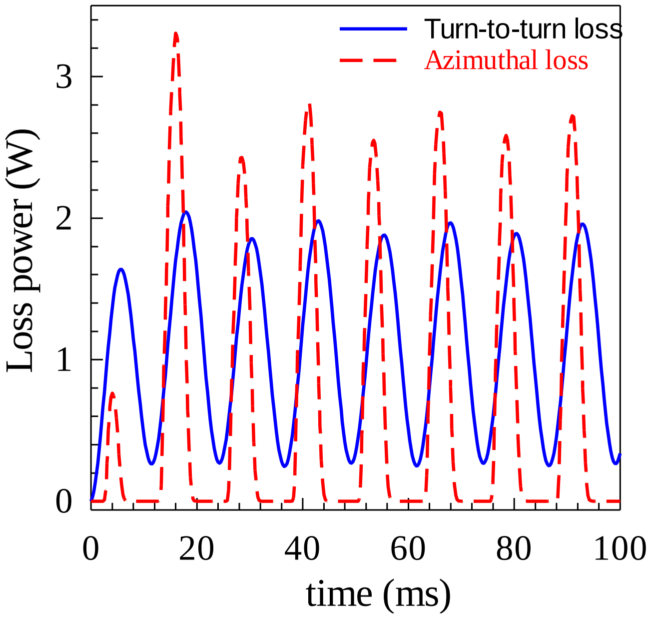

Figure 4.12. Losses generated by radial current (turn-to-turn loss) and azimuthal current when the NI HTS coil is in background field is 56.8 mT/40 Hz, the turn-to-turn resistivity of the NI HTS coil is 96.7 $\mu\Omega\cdot\mathrm{cm}^2$.

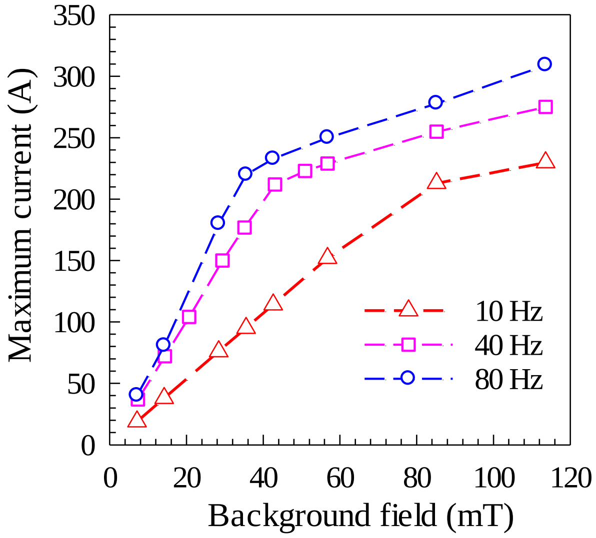

Figure 4.13. Dependence of maximum azimuthal current on the amplitude of background field, the turn-to-turn resistivity of the NI HTS coil is 96.7 $\mu\Omega \cdot \mathrm{cm}^2$.

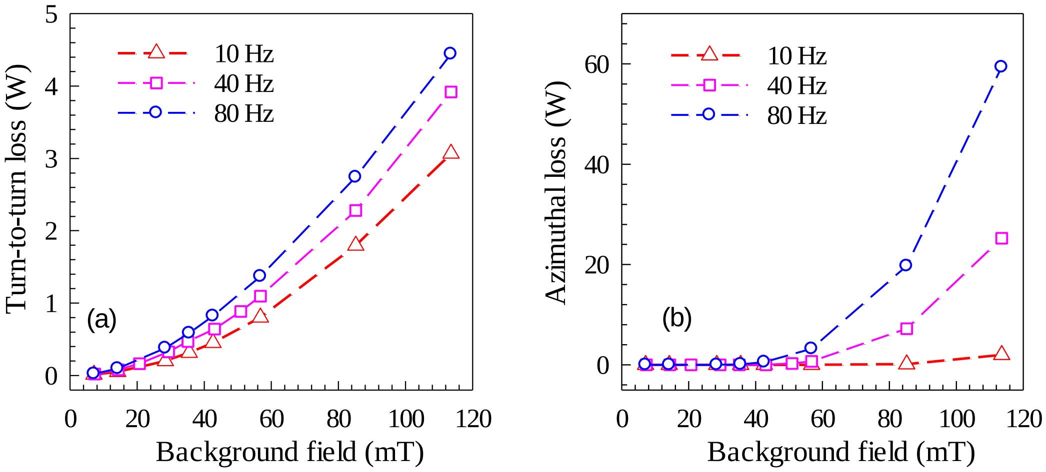

Figure 4.14. Dependence of (a) turn-to-turn loss and (b) azimuthal loss on the amplitude of background field, the turn-to-turn resistivity of the NI HTS coil is 96.7 $\mu\Omega \cdot \mathrm{cm}^2$.

4.4.2 Influence of background fields

Figure 4.13 shows the dependence of the maximum azimuthal current induced (transport current in HTS tape) on the amplitude of background fields. The maximum induced current increases almost linearly with the amplitude of the background fields when it is below the critical current (190 A). Above the critical current, it shows a very slowly increase with the further increase of background fields. Below the critical current, the azimuthal resistance of HTS is nearly zero and the turn-to-turn resistance is constant, and thus, the induced current is almost proportional to the amplitude of the background field. Above the critical current, the resistance of HTS increases rapidly, the maximum transport (azimuthal) current induced is limited, and thus, the increasing rate drops fast.

Figure 4.14 shows the dependence of eddy loss on the amplitude of background fields. The turn-to-turn loss increases rapidly with the amplitude of background fields, and the increasing rate is a little higher than that of linear increase. The azimuthal loss is nearly zero when the induced transport (azimuthal) current is below the critical current, which is much lower than the turn-to-turn loss. When an overcurrent is induced, the azimuthal loss increases dramatically with the background fields, which is beyond the turn-to-turn loss and can be one magnitude of order higher than the turn-to-turn loss. Therefore, a special design is required to prevent this induced overcurrent. Below the critical current, the azimuthal loss is ignorable compared with the turn-to-turn loss.

Figure 4.15 shows the influence of field frequency on the distribution of induced transport current. Higher frequency leads to a more significant nonuniform current distribution on the NI HTS coil, and more induced transport current accumulates on the outermost turns, due to the skin effect. Figure 4.16 shows that the maximum induced transport current increases continually with the frequency of background fields. The results show that a very small AC field can induce a very high transport current in the NI HTS coil, especially at high frequency. As shown in Figure 4.16, a background field of 14 mT/200 Hz can induce a transport current up to 110 A on the NI HTS coil, while the critical current of HTS tapes is only 190 A. In the HTS machine environment of electrical aircraft, the frequency of the ripple field can be much higher than 200 Hz, and the rated current of the HTS coil is often more than 60% of the critical current. Figure 4.17 shows the dependence of the turn-to-turn loss power on field frequency. The logarithm of turn-to-turn loss power is almost proportional to the logarithm of field frequency. The turn-to-turn loss power increases rapidly with field frequency when the frequency is in a low range, but the growth rate drops continually with field frequency. Therefore, the ripple background field with higher frequency leads to more significant eddy current accumulation, higher transport current, and more eddy loss, which can considerably increase the quench risk of the NI HTS coil during operations.

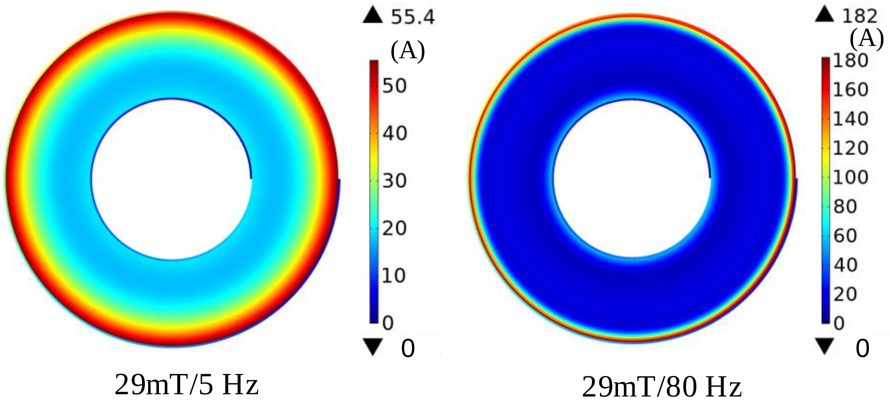

Figure 4.15. Distribution of induced transport (azimuthal) current in the NI HTS coil, the background fields are 29 mT/5 Hz and 29 mT/80 Hz, the turn-to-turn resistivity of the NI HTS coil is 96.7 $\mu\Omega \cdot \mathrm{cm}^2$.

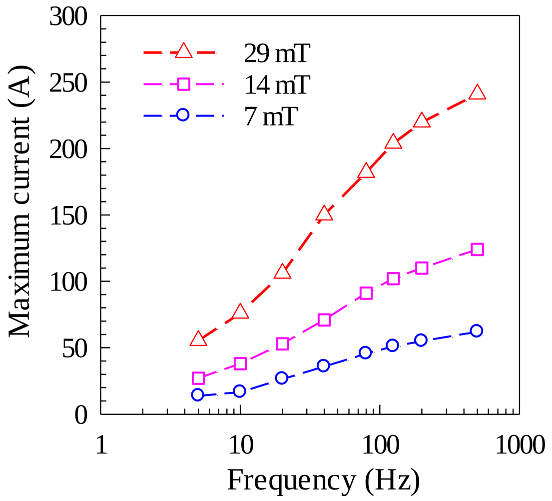

Figure 4.16. Dependence of maximum induced transport (azimuthal) current on the frequency of background field, the turn-to-turn resistivity of the NI HTS coil is 96.7 $\mu\Omega \cdot \mathrm{cm}^2$.

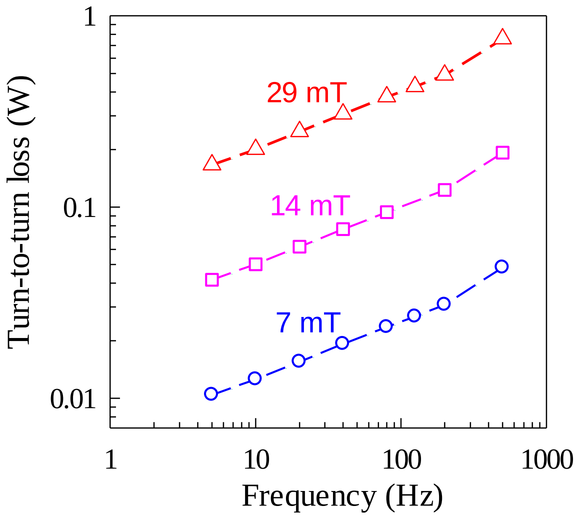

Figure 4.17. Dependence of turn-to-turn loss power on the frequency of background field, the turn-to-turn resistivity of the NI HTS coil is 96.7 $\mu\Omega \cdot \mathrm{cm}^2$.

4.4.3 Influence of turn-to-turn resistivity

The turn-to-turn resistivity of NI HTS coils ranges from 1 to 10 000 μ·cm^2, and it depends on the winding tension, surface condition, materials of lamination, substrate, and stabilizer [152-154]. We change the turn-to-turn resistivity of the NI coil and recalculate the distribution of eddy current induced by ripple background fields, as shown in Figure 4.18. With lower turn-to-turn resistivity, a more significant skin effect is observed, and a higher transport (azimuthal) current is induced in the outermost turns of the NI coil. When the turn-to-turn resistivity is low enough (1 μ·cm^2 in Figure 4.18), the induced current path closes at the connecting position of the outermost turn and its adjacent turns, and thus, the radial current shows a significant accumulation in this zone, which is near the current lead generally, as shown in Figure 4.18. This may induce a local hot spot and increases the quench risk to some extent, and thus, this position is the weak point of the NI HTS coil under ripple fields. The radial current shows a uniform distribution along the angular direction when the turn-to-turn resistivity is high enough. Figure 4.19 shows the dependence of the maximum transport (azimuthal) current on the turn-to-turn resistivity. The results show that the maximum transport current induced can be reduced significantly by increasing the turn-to-turn resistivity. If the background field is high enough (57 mT for example), increasing turn-to-turn resistivity may lead to a slight increase in the transport current induced when the turn-to-turn resistivity is in a low range. Then, the transport current induced drops rapidly with the further increase of the turn-to-turn resistivity. Figure 4.20 shows the dependence of the induced turn-to-turn loss on the turn-to-turn resistivity. The turn-to-turn loss increases with the turn-to-turn resistivity when the resistivity is low. When the resistivity is high enough, the turn-to-turn loss drops rapidly with the further increase of turn-to-turn resistivity. Since the turn-to-turn loss is the product of turn-to-turn contact resistance and the square of the induced radial current, lower turn-to-turn resistivity does not always lead to higher turn-to-turn losses.

If the turn-to-turn resistivity drops to zero, the winding of the NI HTS coil will be shielded from the external ac fields, and the ac loss will be reduced.

On the other hand, if the turn-to-turn resistivity is infinite, the NI HTS coil will change to an insulated HTS coil, and thus, only the superconductor magnetisation loss is induced, which is much lower than the turn-to-turn loss in NI HTS coils. In other words, the behaviour is typical for eddy current loss in metals, where decreasing the resistivity leads to the increase of loss first, then reaches a peak point, and afterwards causes it to drop again. Obviously, this peak point should be avoided when the NI HTS coil is applied in ripple background fields. Therefore, the ac loss of NI HTS coils exposed to AC external magnetic fields can be reduced by both increasing and reducing the turn-to-turn resistivity. Lowering turn-to-turn resistivity always means better current redistribution among turns during quenches, which can increase the thermal stability of the NI HTS coil, while this will lead to more serious charging delay, which is also challenging for the fast magnetisation and demagnetisation of HTS windings [151, 155]. Lower turn-to-turn resistivity will also lead to higher transport current induced by background fields, which will increase the quench risk of the NI coil to some extent. Increasing the turn-to-turn resistivity can significantly reduce the eddy current and turn-to-turn loss induced, while this can prevent current redistribution among turns during a local quench and thus may considerably reduce the thermal stability of NI HTS coils. Therefore, an optimal design on the turn-to-turn resistivity is required on the NI HTS coils when it is applied to machines.

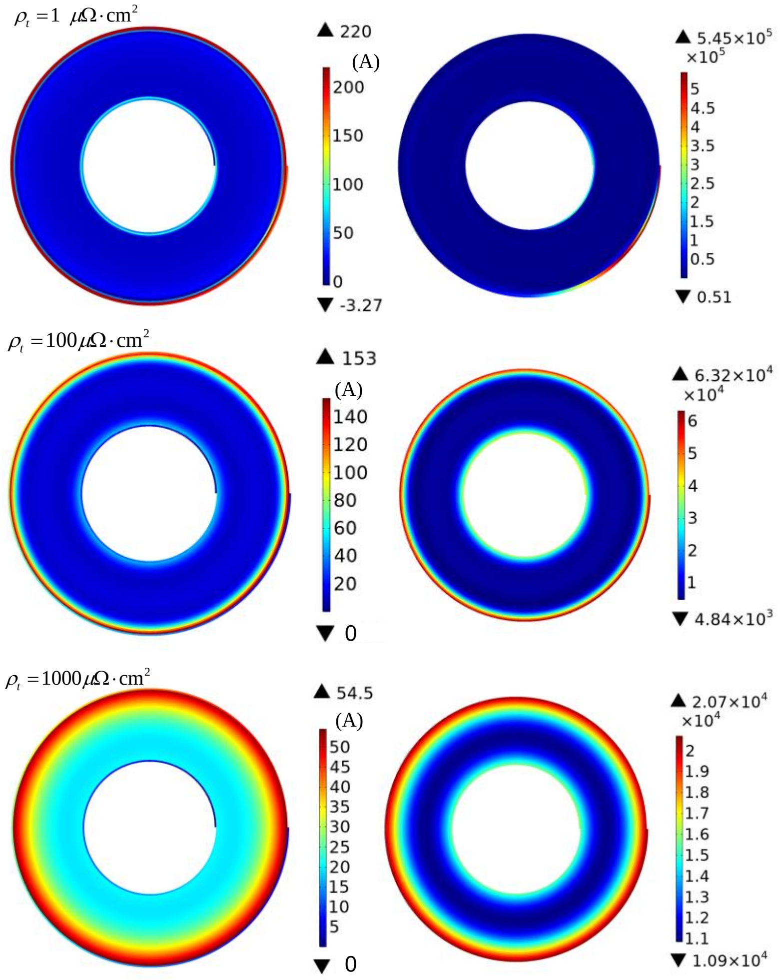

(a) azimuthal current (A) (b) radial current density (A/m^2)

Figure 4.18. The distribution of induced transport (azimuthal) current and radial current in the NI HTS coils with different turn-to-turn resistivity 1~1000 $\mu\Omega\cdot\text{cm}^2$, the background field is 29 mT/50 Hz.

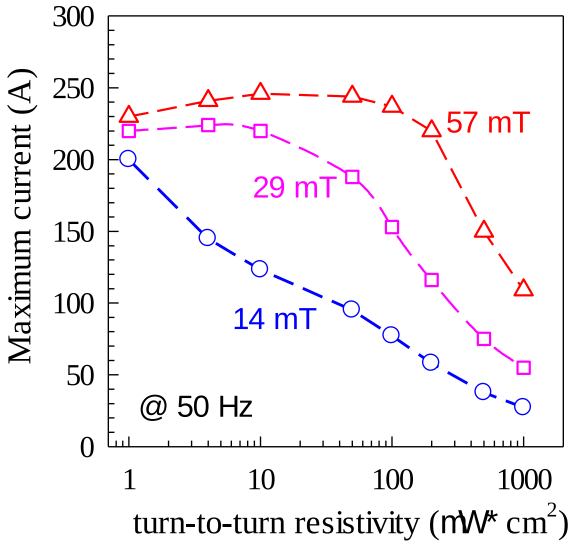

Figure 4.19. Dependence of maximum induced transport (azimuthal) current on the turn-to-turn resistivity of the NI HTS coil, the frequency of the background field is 50 Hz.

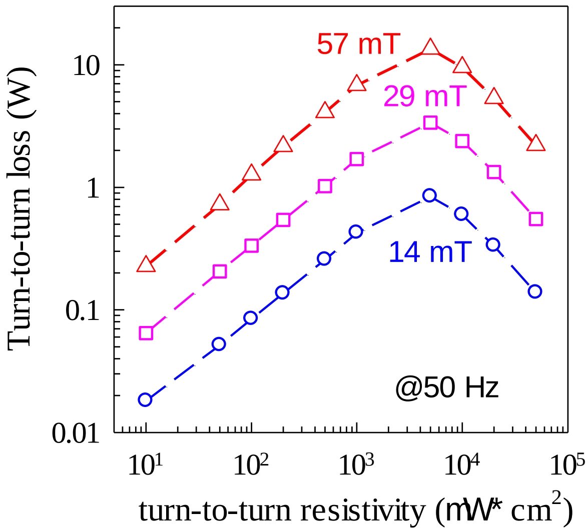

Figure 4.20. Dependence of turn-to-turn loss on the turn-to-turn resistivity of the NI HTS coil, the frequency of the background field is 50 Hz.

4.4.4 Grading turn-to-turn resistivity technique

The abovementioned analysis shows that the transport current induced can be reduced significantly by increasing the turn-to-turn resistivity, while most of the induced current accumulates on the outermost turns of the NI HTS coil. All these studies are based on uniform turn-to-turn resistivity among turns. To reduce the induced transport current and meanwhile keep a better thermal stability of NI coils, a grading turn-to-turn resistivity technique is proposed. Its key idea is that a higher turn-to-turn resistivity is applied on the outer turns of NI coils to reduce the current accumulation, and a lower turn-to-turn resistivity is applied on the middle turns to keep a good thermal stability of the NI coil.

A case study is shown in Figure 4.21. Case 0 is a uniform turn-to-turn resistivity distribution among turns 100 $\mu\cdot\text{cm}^2$, and the distribution of its induced transport (azimuthal) current is shown in Figure 4.18, in which the maximum azimuthal current is 153 A. Figure 4.21 (a) shows three grading turn-to-turn resistivity cases, in which the resistivity of the outermost turns is enlarged. Figure 4.21 (b) shows the distribution of the transport current and the azimuthal current. Figure 4.21 (c) shows the distribution of the turn-to-turn loss power for each case.

The results show that the amplitude of the azimuthal current on the outermost turns is reduced considerably and indicated that the grading turn-to-turn resistivity technique can significantly prevent the current accumulation in the NI HTS coil. The maximum transport current induced is reduced significantly. Since the loss is the product of contact resistance and square of the radial current, and also, the distribution of azimuthal current depends on the turn-to-turn resistivity. The heat can increase the risk of hot induced quench. Therefore, the grading turn-to-turn resistivity technique can significantly enhance the thermal stability of the NI HTS coil exposed to ripple magnetic fields.

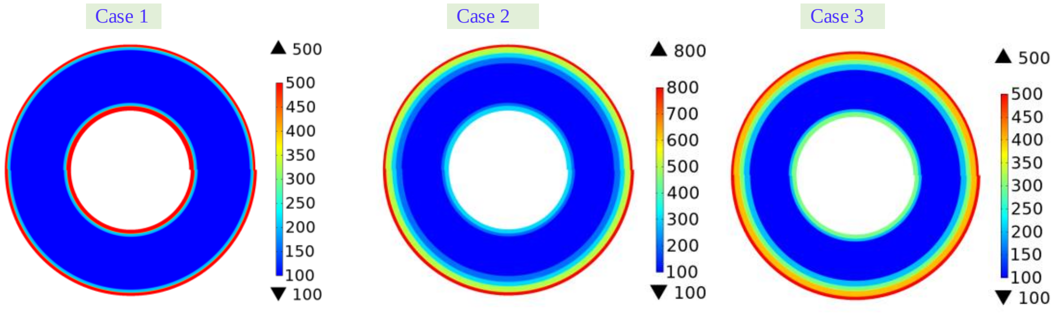

(a) Grading turn-to-turn resistivity ($\mu\Omega\cdot\mathrm{cm}^2$)

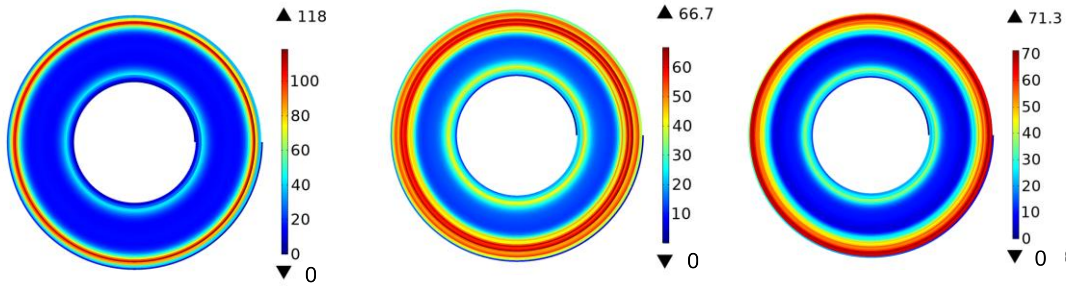

(b) Distribution of transport/azimuthal current (A)

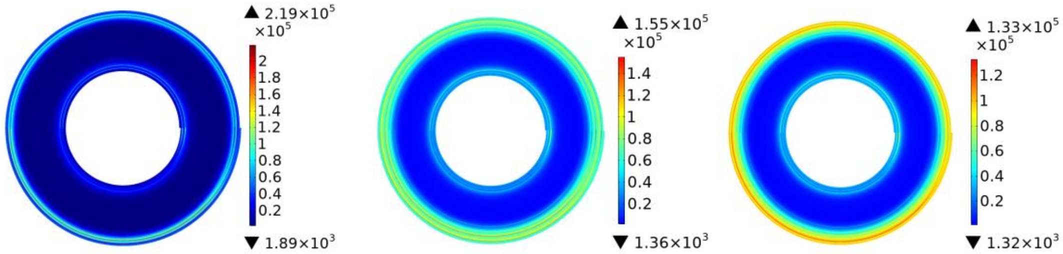

(c) Distribution of turn-to-turn loss power (W)

Figure 4.21. Case study on the grading turn-to-turn resistivity technique, (a) distribution of the grading turn-to-turn resistivity, (b) distribution of the transport(azimuthal) current induced, (c) distribution of the turn-to-turn loss power. The background field is 29 mT/50 Hz.

4.5 Conclusions

To sum up, we studied the practicability of applying the NI HTS winding technique on electrical machines with high power density, which is a promising technique for electrical aircraft propulsion. The induced eddy current and loss of NI HTS coil exposed to ripple magnetic fields are analysed, which have been the main worries about this technique application on the machines of electrical aircraft so far. A numerical model based on the circuit network method is developed for the NI HTS coil exposed to ripple background fields, and it is validated by experiments. Analysis using this model shows that a considerable eddy current is induced in the NI HTS coil exposed to ripple fields. Most of the eddy current accumulates on the outer turns of the NI HTS coil, and a very small external ripple field may induce a very high eddy current on outermost turns. This leads to a higher quench risk on the outermost turns of the NI HTS coil in machines. The induced transport current increases rapidly with the amplitude and frequency of the ripple fields, and an induced overcurrent (above the critical current) is possible when the amplitude and frequency are high enough.

A considerable ac loss is generated in the NI HTS coils, which consists of turn-to-turn loss on contacts and azimuthal loss in HTS tapes. The turn-to-turn loss is more than one order of magnitude higher than the azimuthal loss when the induced transport current is below the critical current. During the overcurrent operation, the azimuthal loss increases dramatically and is much more than the turn-to-turn loss. Therefore, ac loss may be challenging for the efficiency of HTS machines when the NI coil is applied in a machine environment with ripple fields, though the NI technique can significantly enhance the stability and reliability of the HTS windings. The induced transport (azimuthal) current can be reduced significantly by increasing the turn-to-turn resistivity. Below the critical current, the ac loss (turn-to-turn loss) can be significantly reduced by both decreasing the turn-to-turn resistivity and increasing the turn-to-turn resistivity. Lower turn-to-turn resistivity means better thermal stability but leads to a more significant accumulation of eddy current as well as turn-to-turn loss. Therefore, optimising turn-to-turn resistivity is required to avoid this peak point when the NI technique is applied to the HTS machines. A grading turn-to-turn resistivity technique is proposed for the NI HTS coil in machines, which can significantly reduce the transport current induced and meanwhile keep the thermal stability of NI HTS coils. It can considerably increase the practicability of the NI HTS technique in HTS machines of electrical aircraft.

Chapter 5 Insulated HTS coil for HTS stator design

Previous work successfully built a platform to test the HTS coil's performance in a machine environment. Several HTS coils are prepared to study HTS coil, including:

- Coil preparation and selection for HTS armature windings.
- Study of magnetisation loss and total AC loss for HTS armature windings.
- Study of multi-filament tape to reduce AC losses.

5.1 Coil manufacturing

Since 2G HTS tape is a ceramic material and very fragile during manufacturing, too much bend or mechanical stress will cause unrecoverable damage. This requires the winding process of the high-temperature superconducting coil to be as simple as possible to reduce the risk of mechanical damage. The double pancake coils are more suitable for machine purposes because both current leads are located at the outer layer. However, a double pancake coil requires the tape to be separated into two spools, and the coil manufacturing should begin with the mid of the length. This in coil manufacturing the procedures below will be followed: Firstly, to separate half-length of the tape into two spools, A and B, as shown in Figure 5.1 (a); then fix spool B with the coil holder, as shown in Figure 5.1 (b), start winding the first layer of the double pancake coil using tape from spool A, as spool B is rotating with the coil holder, no twist or bend occurs to avoid the risk of any mechanical stress. After finishing the first layer processing, taking off spool B and starting the second layer processing, as shown in Figure 5.1 (c). Finally, the finished double pancake coil is shown in Figure 5.1 (d).

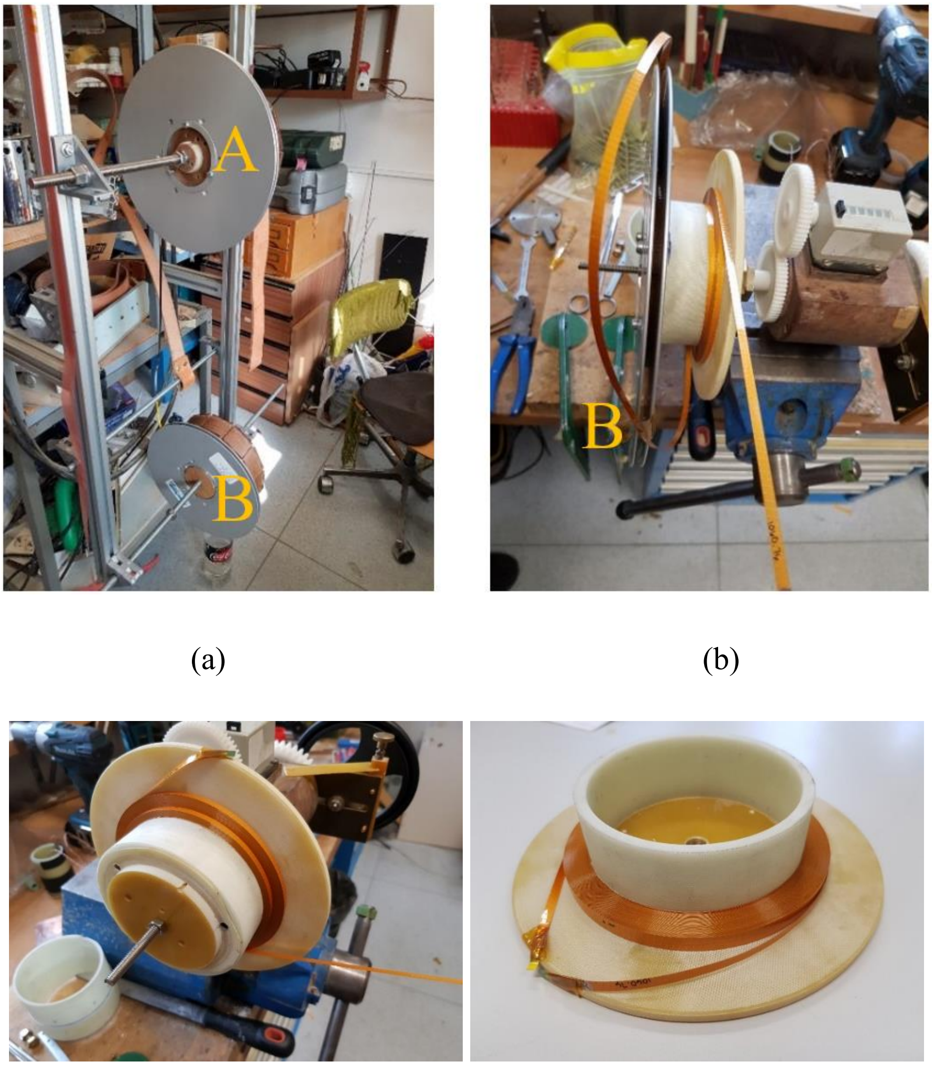

(a) (b)

(c) (d)

Figure 5.1. Double pancake coil manufacturing process: (a) Spool A and spool B; (b) winding the first layer of the double pancake coil; (c) winding the second layer of the double pancake coil; (d) completed coil.

5.2 Coil test in the HTS machine

In electrical machines, the HTS AC windings are subjected to a combined rotational magnetic field and AC current. The AC loss depends not only on the magnitudes of the magnetic field and transport current, but also on the phase shift between the field and the current. Different magnetic field directions and different phase shifts give different levels of AC loss. AC loss studies in HTS tapes and coils have been carried out throughout the duration of the development of HTS devices [36, 101, 105, 129-131, 136, 139, 156, 157]. There are two established methods for measuring AC loss. The transport loss and magnetisation loss of HTS can be measured by the electrical method. The total AC loss, which includes both transport loss and magnetisation loss, can only be measured by the calorimetric method [157]. Previous studies have measured the total AC loss of HTS coils using both the liquid nitrogen boil-off method and the temperature rising method [99, 158, 159]. However, the rotational magnetic field which is an important feature of electrical machines, has not previously been studied in AC loss experiments.

To understand the impact of rotational magnetic fields on the HTS armature losses and the whole machine efficiency, an axial-flux HTS machine platform has been designed and developed to measure the AC loss of an HTS stator in a rotational magnetic field, as shown in Chapter 3. The HTS machine consists of a 2-pole-pair of permanent magnet rotor discs to generate a peak of 0.45 T in a 60 mm air-gap, and an air-cored three-phase HTS stator plate. The stator disc is located between the two rotor discs. The stator is equipped with two HTS coils in Phase *A* and four copper coils in Phases *B* and *C*. Also, as Figure 5.2 shows, the whole machine is hosted in a vacuum-walled cryostat filled with liquid nitrogen (LN_2) during operation, and the top HTS coil was placed in a measurement chamber to measure the AC loss by the calorimetric method. The measurement chamber is fully immersed in LN_2 inside the machine cryostat to minimise heat exchange. A previous study had carefully calibrated and validated this system [160], to provide AC losses of stator coil when the machine was real-time running.

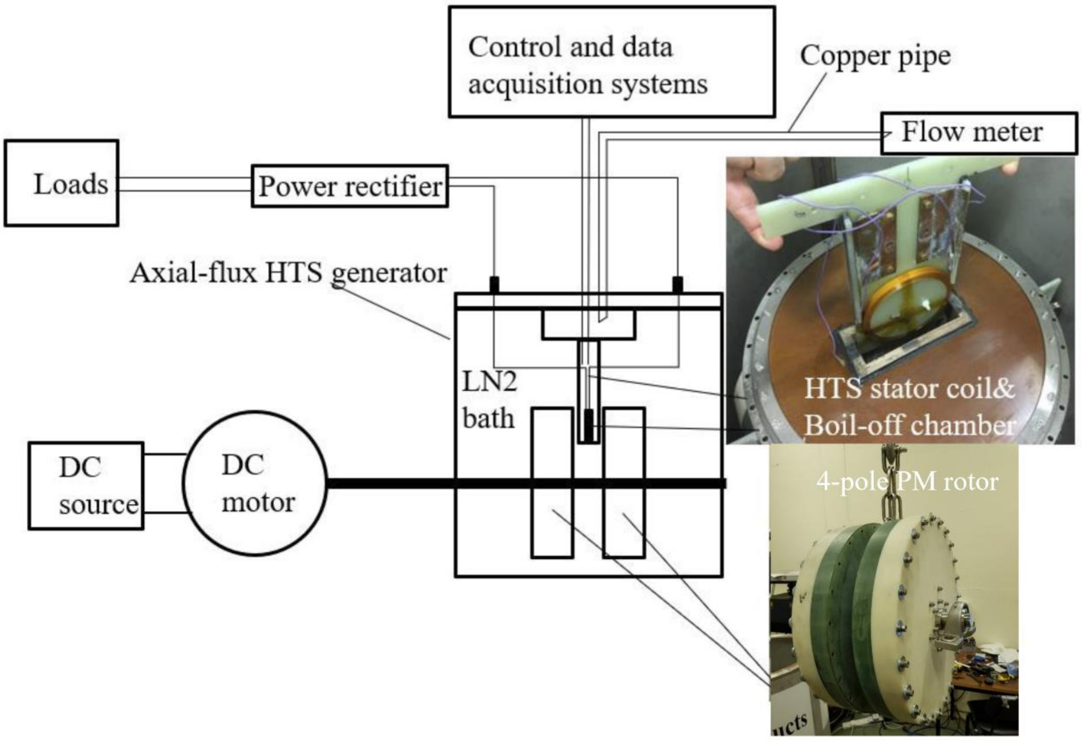

Figure 5.2. Structure of the HTS generator

The AC loss of the HTS coil is measured by the amount of liquid nitrogen being evaporated as nitrogen gas using a gas flow meter. Figure 5.2 shows a copper pipe that connects to the flow meter. Theoretically, the latent heat for liquid nitrogen is 160.6 J/mL, which means every 0.257 standard litre nitrogen gas per minute for every Watt of power (SLPM/W). Therefore, by measuring the nitrogen gas boil-off flow rate, the total AC losses in the measurement chamber can be measured. Total AC loss of *T* can be calculated by Equation 5.1 [101].

$$Q = \int_T \frac{F(t)}{K} dt \tag{5.1}$$

Where Q (Joule) is the total heat produced by the measured HTS coil for a duration of T, F(t) is the flow rate of nitrogen gas boiled off in the measurement chamber. $K=0.256$ (SLPM/W) is the flow rate constant in our setup.

This system provides a synchronous generator to generate 3 phase voltage, the measured HTS coil in the HTS phase can provide the AC losses data while running the machine, two copper phases were impedance match between phase A to provide the same voltage amplitude, in FFT analysis only 3rd harmonic exists in the stator, and the phases are star-connected to remove the 3rd harmonic. The rated line-to-line voltage is 40 V. The Coil #1 is made of 25 meters of 2G YBCO HTS coated conductor, with a critical current measured as 53 A in the 0.45 T rotational field. The peak phase current must be lower than 53 A to prevent HTS quench. Due to the critical current of the HTS coil, the rated current is set as 40 A. The generator was connected with a power rectifier also run in LN_2 temperature, then connected with adjustable power resistors, as Figure 5.2 shown. The data acquisition systems can record the temperature, phase voltage, phase current, nitrogen gas flow rate to calculate total AC losses.

5.2.1 ReBCO characteristics test

Several industrial manufacturers are able to provide REBCO coated conductors for multiple purposes. Due to the differences between REBCO materials, the $J_c(B)$ characteristics of the various tapes could be different. For 2G HTS tapes, the critical current is decreased when the external magnetic field increases, thus, based on the critical-state model, the change in AC current and external AC magnetic field cause the magnetic field redistribution inside the HTS tapes. The transport AC loss is caused by AC current, and the total loss is caused by AC current as well as the AC magnetic field. As a result, in the machine environment, good $J_c(B)$ characteristics of the tape can enhance the AC loss performance.

Thus, another Coil #2 is prepared to make a comparison. Coil #2 is made of 15.5 meters of 2G GdBCO HTS tape. The YBCO tape is from Superpower SCS4050 including 1 μm YBCO, and GdBCO tape is from Sunam SAN04150 including 1-3 μm GdBCO, the total wire thickness of both wires is 100-110 μm. The single tape's critical current for Coil #1 and Coil #2 is 143 A and 150 A, respectively. Figure 5.3 shows the picture of two coils. The parameters of the two coils are shown in Table 5.1.

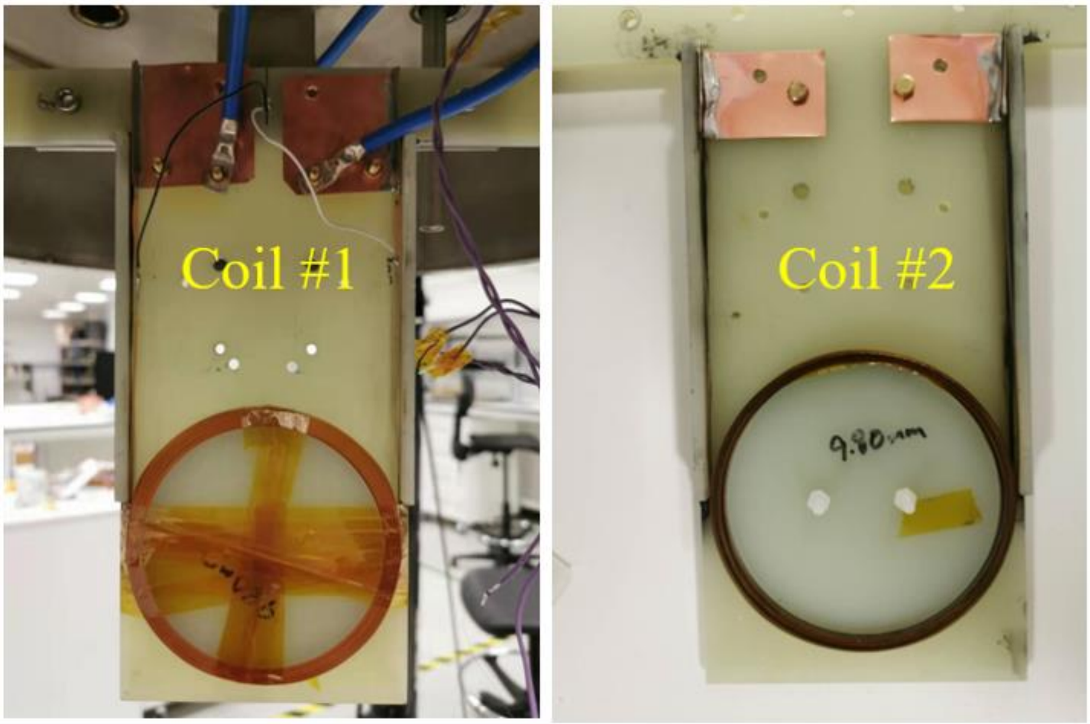

Figure 5.3. Photos of Coil #1 and Coil #2.

Table 5.1. Description of manufactured double pancake coil

	Coil #1	Coil #2
HTS type	Superpower SCS4050	Sunam SAN04150
Coil Length	25 m	15.5 m
Coil inner/outer diameter	98 mm/102.8 mm	98 mm/103.0 mm
Turns per layer	39	25
Total coil turns	78	50
Self-field Ic	72 A	102 A
In-field Ic (0.45 T)	53 A	59 A
Insulation	Kapton tape	Kapton tape

The critical current results are shown in Figure 5.4. The red curve shows the critical current of Coil #1, and the blue curve demonstrates the critical current of Coil #2. The curves with triangle signs indicated the result in 0.45 T magnetic field, the curves with circle signs indicated the critical results with self-field. Figure 5.4 indicated that the critical current drop from self-field to in-field. By using 0.1μV/cm criteria, for Coil #1, the critical current reduces from 72 A to 53 A when a 0.45 T magnetic field apply, which means a 26.4% drop. For Coil #2, the critical current reduces from 102 A to 59 A, which means a 42.2% drop. Although Coil #2 has a higher critical current in 77 K, the critical current decreased rapidly with increasing magnetic field. Thus, Coil #1 has a better $J_c(B)$ characteristic.

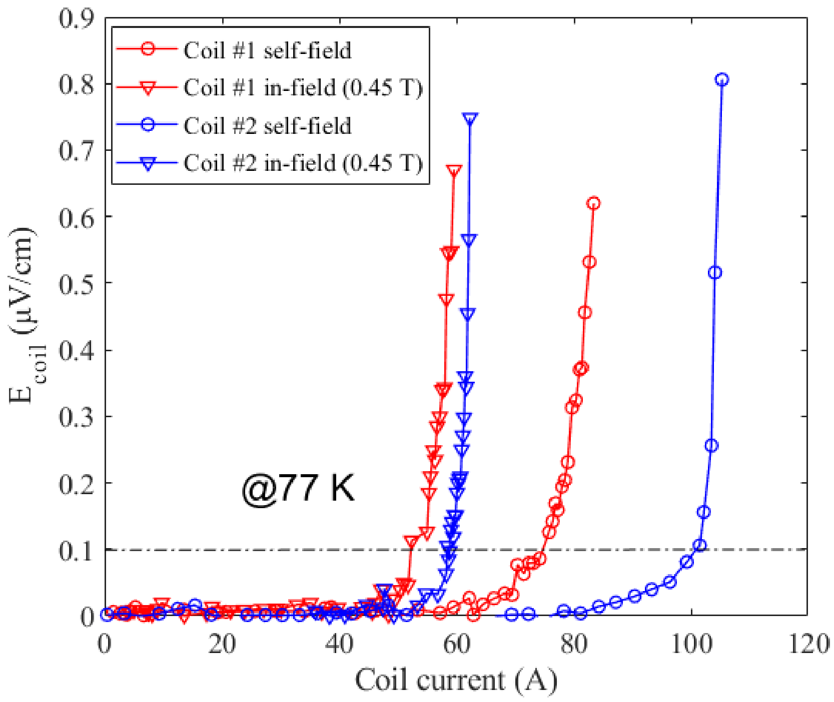

Figure 5.4. Critical currents of Coil #1 and Coil #2.

In order to evaluate the difference between the two coils, the experimental value of transport loss is measured by the electrical method [101, 131]. The loss voltage can be compensated by a cancelling coil, as shown in Equation 5.2, where i and u_c are the transport current and voltage after compensation by cancelling coil. T refers to the cycle of AC current. Two frequencies were chosen for this experiment. The normalized transport loss versus normalized transport current measured by the electrical method is shown in Figure 5.5. According to our AC power supply's limit, the frequencies are chosen at 36 Hz and 72 Hz, and the results are shown by normalized AC loss (Joule/cycle/m). The results indicate that the transport AC loss of both coils is frequency independent. According to the normalized transport AC loss results, the transport loss of Coil #1 is 43.1% lower than Coil #2.

$$Q = \int_T (i \cdot u_c) dt \tag{5.2}$$

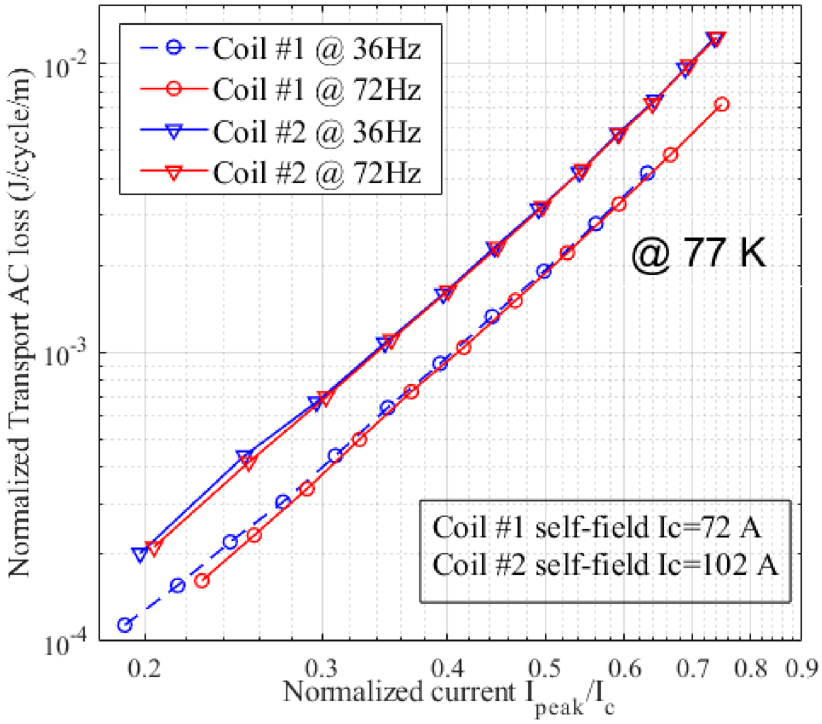

Figure 5.5. Transport loss of Coil #1 and Coil #2.

The total AC loss versus normalized current was measured by the calorimetric method are shown in Figure 5.6. The maximum rotational speed is 300 RPM due to the limitation of the bearing in 77 K, which means a 10 Hz output. Thus, the frequencies are set at 5 Hz and 10 Hz, the transport currents are chosen from 10 A to 50 A. In our machine, the rotor generates a peak of 0.45 T rotational magnetic field. According to the normalized total AC loss results, both coils' total AC loss is frequency independent, and the total loss of Coil #1 is 65.8% lower than Coil #2. Also, Figure 5.4 and Figure 5.5 indicate that Coil #1 has lower transport AC loss and fewer in-field critical current reduction. As a result, two coils have the same outer diameter, Coil #1 has more length of tapes and more turns, but AC losses are significantly lower than Coil #2, considering the operating reliability for the following stage machine experiments, the Coil #1 is finally chosen for subsequent stage tests.

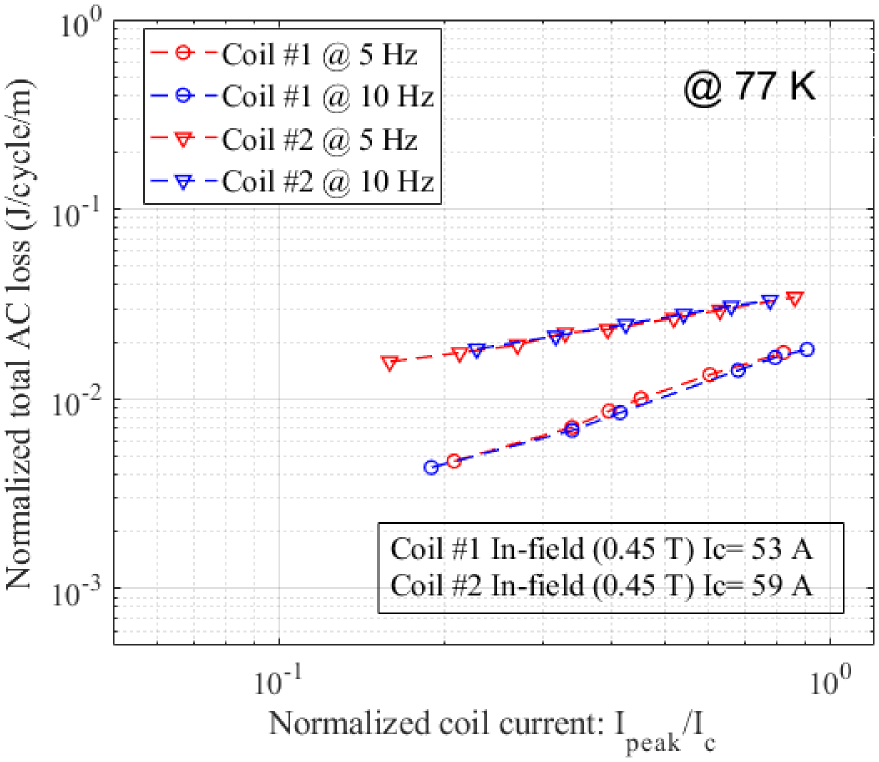

Figure 5.6. Total loss of Coil #1 and Coil #2.

5.3 AC loss of HTS stator

The HTS coil is prepared using 25 meters 4mm superpower SCS 4050-AP tape, and the single tape critical current is 140 A. The specification of the HTS double pancake coil is shown in Table 5.2. The photograph of the coil and setup is illustrated in Figure 3.13 (b).

Table 5.2. Specification of HTS stator winding coil

Parameters	value
Tape type	Superpower SCS4050-AP
Tape Ic	140A
Coil Ic (self-field)	72A
Coil inner diameter	95mm
Coil outer diameter	99.8mm
Turns per layer	38
Total coil turns	76
inductance	937.4μH

Both the self-field critical current and in-field critical current of the coil was measured, and the results were shown in Figure 5.7. By using 0.1 μV/cm criteria, the self-field critical current is 72 A and the in-field critical current is 53 A (at peak 0.45 T). Thus, this coil is satisfied to operate at a peak current of 40 A.

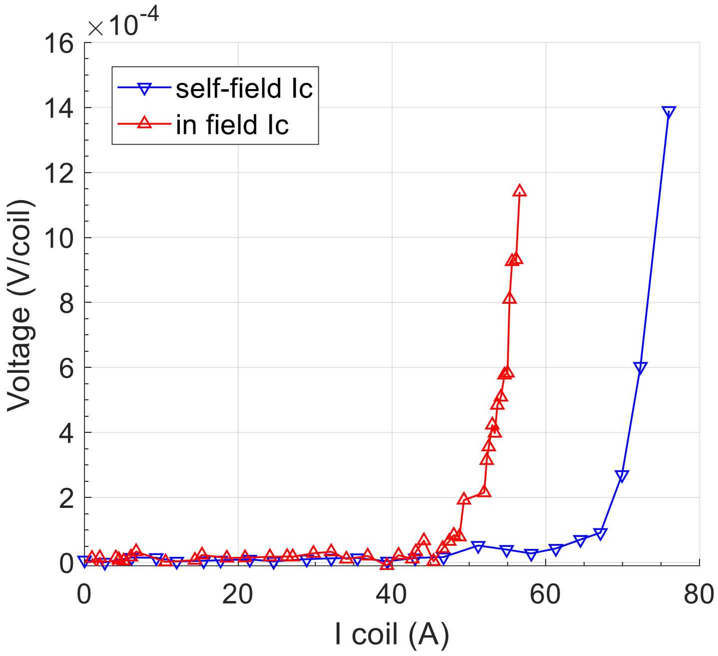

Figure 5.7. Self-field and in-field critical current.

5.3.1 Magnetisation loss

The magnetisation loss of this coil can be measured by keeping the HTS coil open circuited, so no transport current in the HTS coil and only the magnetisation loss is measured. We measured five different frequencies (3.33 Hz, 5.00 Hz, 6.67 Hz, 8 Hz and 10 Hz), as this is a two-pole-pair rotor, these frequencies corresponding to rotor speeds at 100, 150, 200, 240 and 300 RPM, respectively. Recording the flow rate data at these frequencies (the sample rate of data acquisition is 20 S/s), the results were shown in Figure 5.8 (a), the red line showed the flow rate data, and the blue line showed the rotor speed. When the rotor speed increase, the thermal equilibrium condition change to a new thermal balance condition. After a short unbalanced thermal period, a fluctuation level lower than 0.08 SLPM was observed. These fluctuations are caused by small bubbles of nitrogen gas in the measurement chamber. Thus, use the integral operation to calculate the total nitrogen gas volume of the last 10 seconds. After flow rate calibrating out the errors by Equation 3.2, the magnetisation loss of this coil versus frequency can be calculated by Equation 3.1, as Figure 5.10 (b) shown.

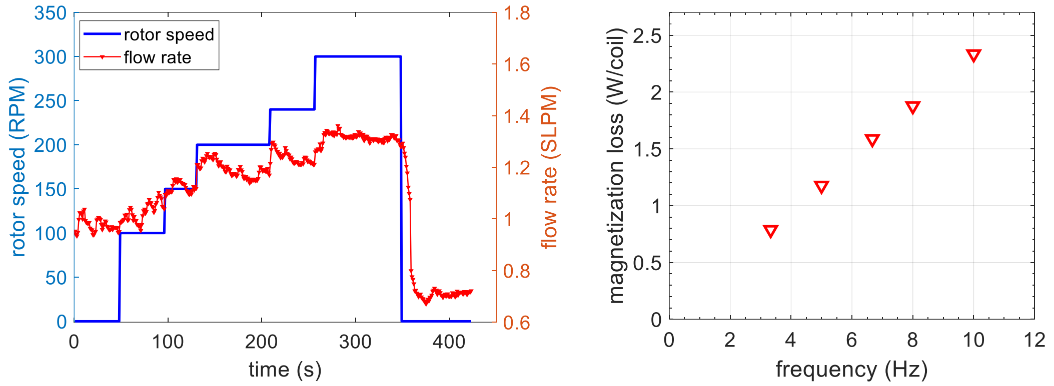

(a) (b)

Figure 5.8. Magnetisation loss versus frequency.

To estimate the magnetisation loss, finite element modelling is used for magnetisation loss calculation. Previous studies have been demonstrated that finite element modelling using H-formulation can estimate AC loss for double pancake coil. Our double pancake coil specification is shown in Table 5.1. Figure 5.9 shows that a COMSOL model of this coil was developed using a 2D axis-symmetric model and H-formulation [99]. The model was simplified by applied a time-variant magnetic field using Figure 3.10 (a). The FEM simulation results indicated that at 10 Hz, the magnetisation loss of double pancake coil is 2.2 W. As this value is calculated by a time-variant magnetic field waveform, the magnetic environment is not exactly the same as experiments. Thus, the simulation result can only use to estimate the magnetisation loss level.

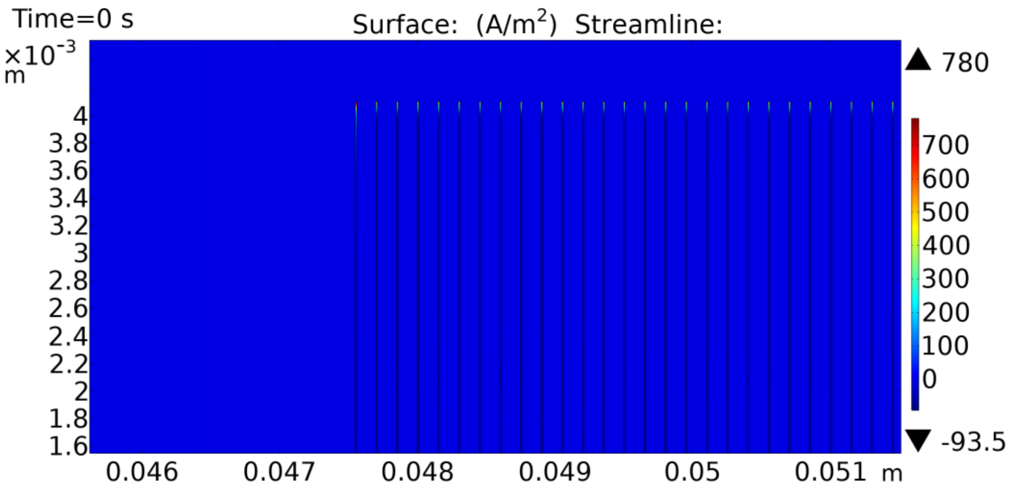

Figure 5.9 The FEM model of the HTS stator coil in COMSOL

5.3.2 Total AC loss

The total AC loss of the single HTS coil is measured by connecting the three-phase stator windings to adjustable power resistors. To measure the total AC loss with various currents, the resistors need to be changed. We measured six different peak transport currents between 10 A and 40 A for four frequencies (3.33 Hz, 5 Hz, 6.67 Hz and 10 Hz), corresponding to rotor speeds at 100, 150, 200 and 300 RPM, respectively. The maximum speed for the rotor is set at 300 RPM to protect the rotor bearings in cryogenic temperature. Flow rate data from experiments were illustrated in Figure 5.10, where the blue curves refer to the rotor speed, and the red curves refer to the instantaneous flow rate value. The transport current values for different frequencies are shown in Table 5.3. The AC loss is a small value when a small transport current applies and also low frequencies, if fluctuate level is below 0.08 SLPM more than 1 min, use the integral operation to calculate flow rate data of last 10 seconds to improve accuracy. After calibrating out the errors by Equation 3.2, the total AC loss versus transport current are shown in Figure 5.11. Figure 5.12 shows a comparison between the total AC loss and the transport AC loss. The rotational field of 0.45 T has significantly increased the AC loss of the coil.

Our results show that at a peak current of 73% Ic and a peak rotational field of 0.45 T, the HTS coil generates in total 4.56 W of heat at 10 Hz and 48 A. To further understand the impact of a rotational magnetic field, we compared the transport loss of the HTS coil with the total AC loss, as shown in Figure 5.12. The transport loss was measured in 77 K using the four-point electrical method [101, 161], since the normalised AC loss is frequency independent (Joule/cycle), the frequencies were chosen as 36 Hz and 72 Hz to give higher loss and higher accuracy. The total AC loss is very high for standard 4 mm HTS tape used as machine windings. To minimise the total AC losses from HTS stator windings, new HTS winding solutions to reduce AC loss are essential. One advantage of this platform is that it enables the comparison of the AC loss of different HTS windings. For example, we plan to measure a 1 mm wide multi-filament HTS cable coil with the same geometry as the HTS coil used in this chapter and quantify its loss reduction in a machine environment [111, 115].

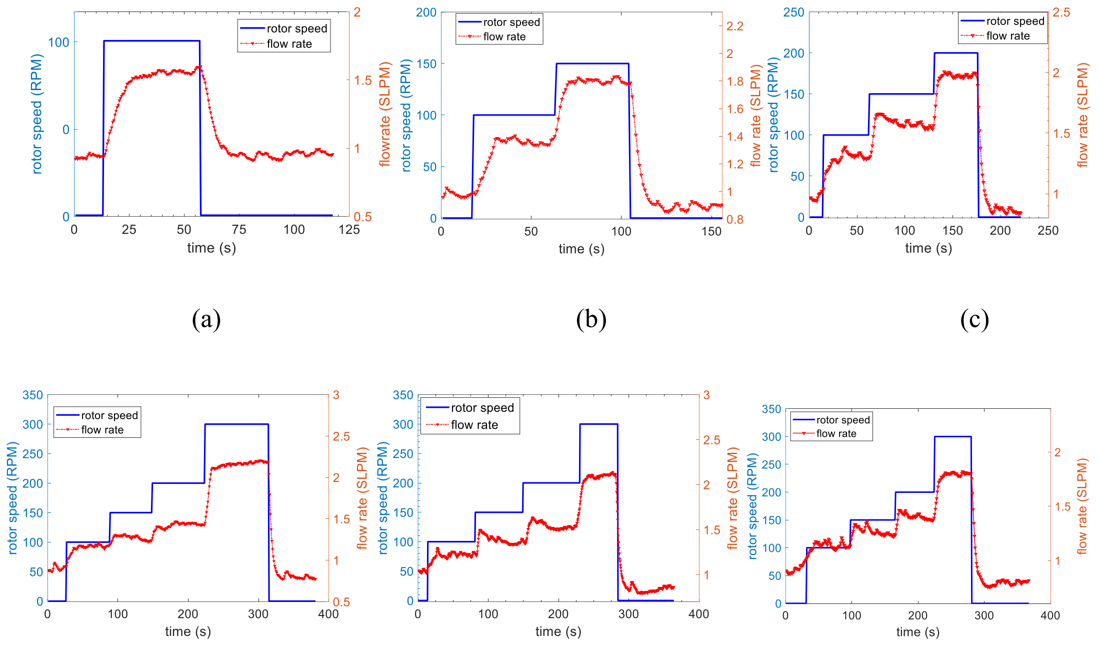

(a)

(b)

(c)

(d) (e) (f)

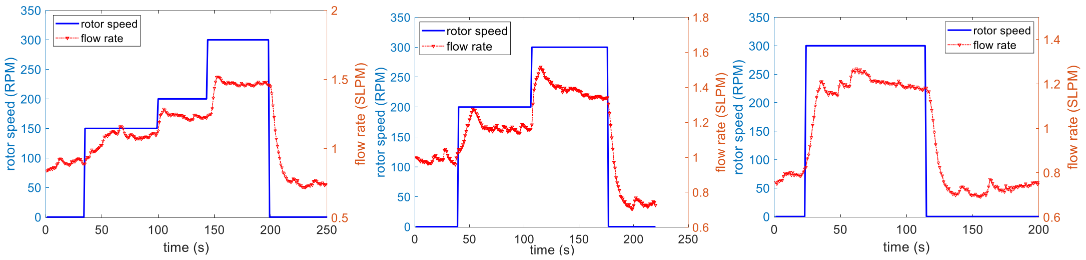

(g) (h) (i)

Figure 5.10. Total AC loss measurements.

Table 5.3. Transport current values in Figure 5.10

	3.33 Hz	5.00 Hz	6.67 Hz	10.00 Hz
Figure 5.10 (a)	40A			
(b)	29A	43.5A		
(c)	21A	32A	41A	
(d)	16A	24A	32A	48A
(e)	14A	21A	28A	42A
(f)	11A	18A	24A	36A
(g)		11A	15A	22A
(h)			12A	18A
(i)				10A

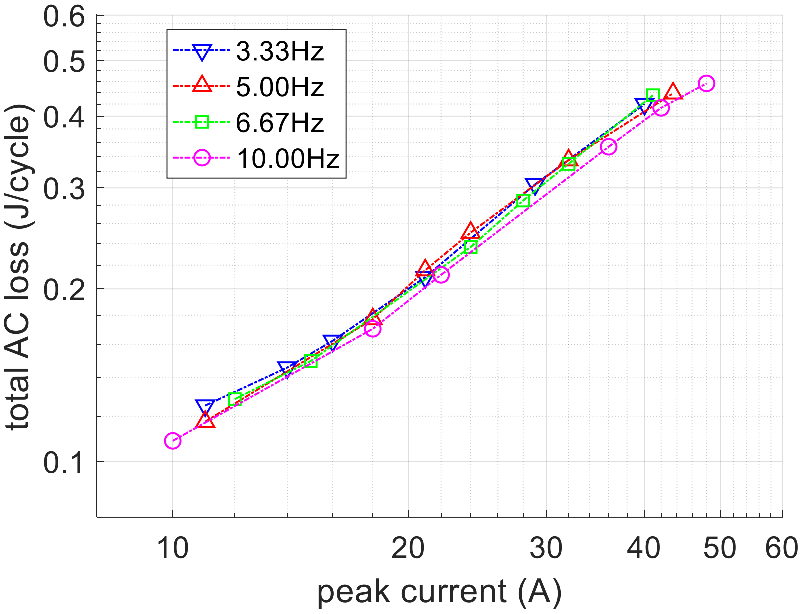

Figure 5.11. Measured total AC loss.

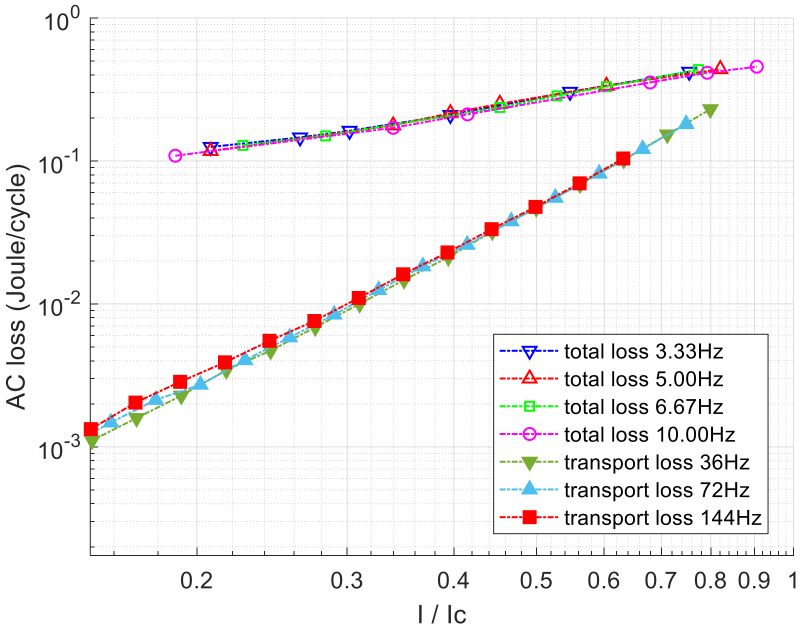

Figure 5.12. Transport loss and total loss.

5.4 AC loss reduction

Since 2G high temperature superconducting tapes have a high current density, it is suitable for high-power application proposes. However, their extremely large width-to-thickness ratio in geometry (which is usually above 1000) makes them easily subjected to significant magnetisation loss under time-varying magnetic fields conditions. AC loss becomes an issue to affect the efficiency of HTS AC machines [160, 162, 163]. AC loss reduction technology has become a hot research focus.

Commercial 2G HTS manufacturers can provide ReBCO tape with various widths (typically 4 mm or 12 mm). The magnetisation AC loss per unit length of an HTS tape with a large width-to-thickness ratio, with the geometry of width $2a$, thickness $2b$ and critical current J_{cs}, sheet critical current density $J_{cs} = J_c/2a$, in a uniform AC perpendicular field $H_a \sin(\omega t)$ is given in equation [111]:

$$Q = 4\mu_0 a^2 J_{cs} H_a g\left(\frac{H_a}{H_c}\right) \tag{5.3}$$

Where μ_0 is vacuum permeability, $g(x) = (2/x)\ln\cosh(x) - \tanh(x)$, and $H_c = J_{cs}/\pi$.

When the background magnetic field is large enough to fully penetrate the HTS tape, the magnetisation loss is proportional to the square of tape width according to Equation 5.3. Thus, the multi-filament HTS tape can reduce AC loss by narrowing the tape width.

The challenge is that the multi-filament 2G HTS tape can be easier to damage due to narrower tape width when manufacturing and operating in a complex electromagnetic environment. The overall losses could also increase due to a coupling current will flow between copper stabilizer layers in AC magnetic fields. Thus, 2G HTS tape with a transposition structure to reduce coupling losses has been proposed, e.g. Roebel cables [53]. The study of AC loss reduction on Roebel cables has been reported in [164-166]. However, a Roebel cable's manufacturing process is complicated, and an abundance of materials will be wasted during the punching process. The tape is also easy to damage due to the imperfect punching manufacturing process. A new multi-filament HTS wire is called soldered-stacked-square (3S) wire is proposed to reduce AC losses by Shanghai Jiaotong University [167]. The idea is to mechanically cut 4 mm wide tape into 1 mm, stack them into a wire and soldering simultaneously. The previous results have shown good critical current distribution and effectively reduce transport AC loss [115]. However, the total loss of 3S wire in a machine environment has not been studied yet.

To confirm the effectiveness of the 3S wires in AC loss reduction, we studied the total loss and magnetisation loss of double pancake coils made of a 3S wire and normal 4 mm tape in a 0.45 T rotational background magnetic field, respectively. To prove 3S wire can effectively reduce total AC loss in a machine environment.

5.4.1 3S coil preparation

As the magnetisation loss is proportional to the square of the conductor's width, we proposed to mechanically cut 2G HTS tape to 1 mm and stack the narrow conductors into a wire structure, which is called 3S HTS wire. As shown in Figure 5.13, the 3S wire is fabricated through narrowing, soldering and stacking processes. The commercial 2G HTS conductors are cut into 1 mm filament. The critical current of each 1 mm tape is about 50 A.

Due to the imperfect manufacturing process, two spools of 3S tapes are prepared for the test. Coil #3 and Coil #4 are winding with 3S wire. Coil #3 is insulated by Kapton tape, and Coil #4 is insulated by a heat-shrink tube, as shown in Figure 5.15.

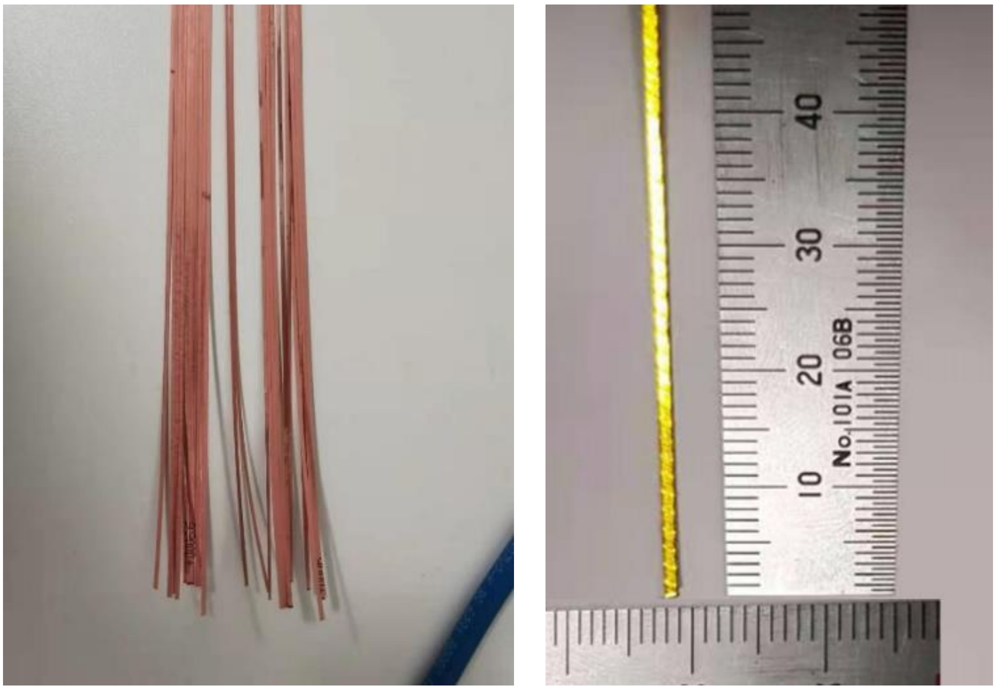

Figure 5.13. Multi-filament wire manufacturing.

Figure 5.14 shows the test result of the uniformity of the critical current of the single wire used in Coil #3, the uniformity can be scan by a Hall-probe and then calculate by critical model, the critical current by this method (average 250A) will be higher than critical current measured by electrical method (normally around 150 A). The uniformity of the critical current of the HTS wire describes its reliability. A low point was observed, this damage is caused by imperfection of mechanical cutting. This low point refers to one mechanical damage point when cutting the ReBCO tape. Thus another wire without a low point was manufactured and prepared for Coil #4.

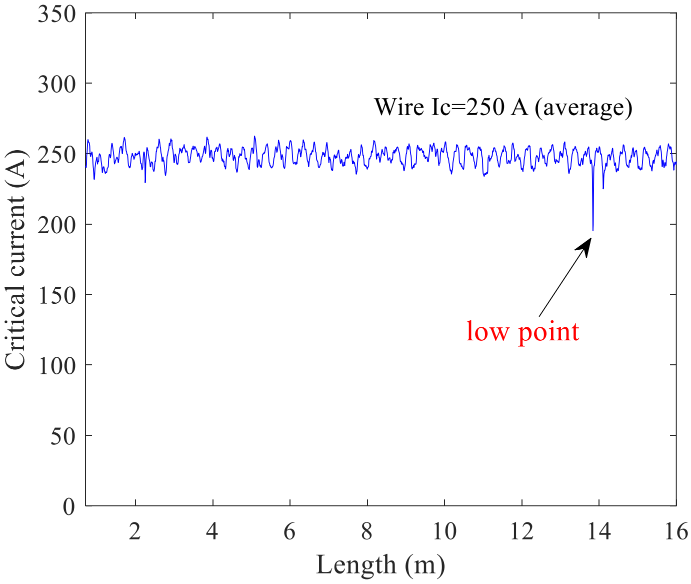

Figure 5.14. Uniformity of the critical current of the 3S wire.

Figure 5.15. Photos of 3S Coil #3 (left) and Coil #4 (right).

Table 5.4. Specifications of Coil #3 and Coil #4

	Coil #3	Coil #4
HTS type	Sunam SAN04150	Sunam SAN04150
Coil Length	20 m	15.5 m
Coil inner/outer diameter	98 mm/110 mm	98 mm/103.0 mm
Total coil turns	54	56
Single wire Ic @77 K	150 A	150 A
Self-field Ic @77 K	75 A	91 A
In-field Ic (0.45 T @77 K)	Not measured	49 A
Insulation	Kapton tape	Heat-shrink tube

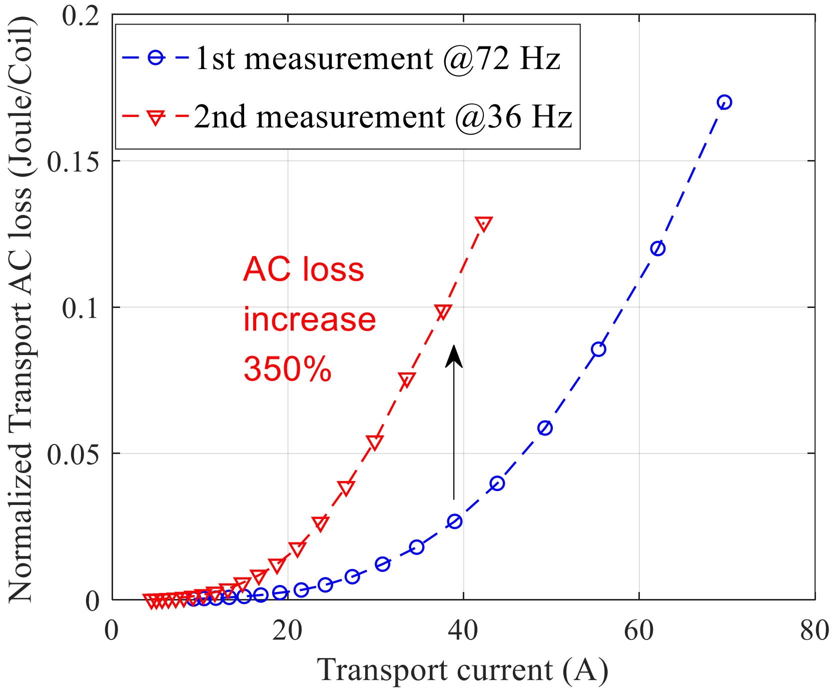

Figure 5.16. Transport loss measurement for Coil #3.

Figure 5.15 shows the normalized transport AC loss (Joule/cycle) of Coil #3. The first measurement was applied at a frequency of 72 Hz, and some abnormal bubbles occurred during the measurement. It means a hot spot occurred in the wire due to the imperfect wire manufacturing process. Then the second measurement was applied at a frequency of 36 Hz, the heat continuously accumulates in the coil and cause the coil to be further damaged. An increase of 350% of normalized transport AC loss was observed. Finally, Coil #3 was burned out during the transport loss test, as shown in Figure 5.17. Since a low point exists in Coil #3 and the insulation tape's thermal conductivity is not good, this causes a quench to happen in the coil's inner turns.

Coil #4 is made by a 3S wire without an imperfect point. The heat-shrink tube is attempted to insulate the coil to reduce the usage of Kapton tape. In the next stage, the AC losses of Coil #4 were studied, including transport loss, magnetisation loss and total loss in a rotational magnetic field. Also, the results are compared with Coil #2, which is made with the normal 4 mm tape.

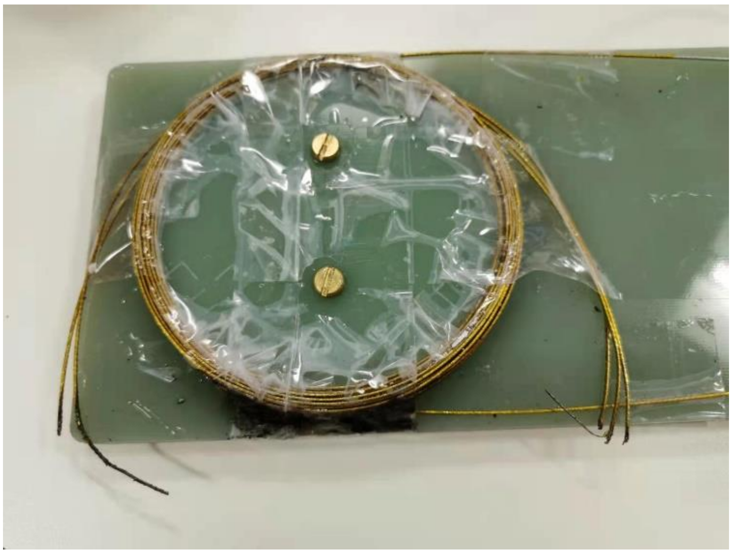

Figure 5.17. Coil #3 was damaged after the transport loss test.

5.4.2 3S coil measurements

Coil #2 and Coil #4 are made of normal 4 mm tape and 1mm 3S wire, respectively. The full specifications of Coil #2 and Coil #4 are shown in Table 5.4. The critical current result of Coil #2 (normal 4 mm tape) is shown in Figure 5.18. The red curve shows the critical current in a 0.45 T magnetic field, and the blue line demonstrates the critical current with self-field. The critical current result of Coil #4 (1 mm multi-filament tape) is shown in Figure 5.19, the red curve shows the critical current in 0.45 T magnetic field, the blue line demonstrates the critical current with self-field. By using 0.1μV/cm criteria, for Coil #2, the critical current reduces from 102 A to 59 A when a 0.45 T magnetic field apply, which means a 42.2% drop. For Coil #4, the critical current reduces from 91 A to 49 A, which means a 46.2% drop. The critical current results of Coil #4 are about 10% - 20% lower than Coil #2 due to the imperfections in mechanical cutting.

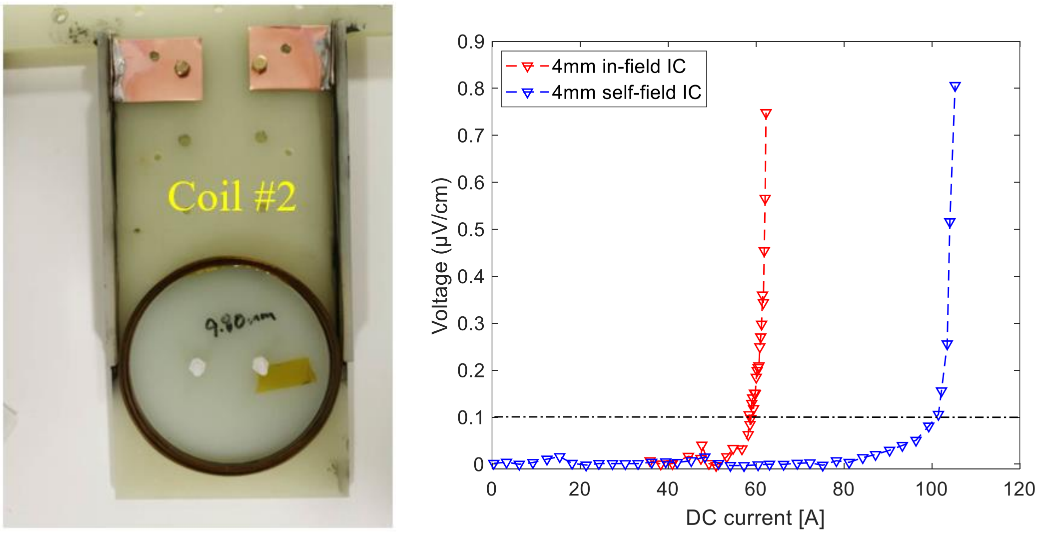

Figure 5.18. Picture of Coil #2 and its critical current with self-field and in-field (0.45 T).

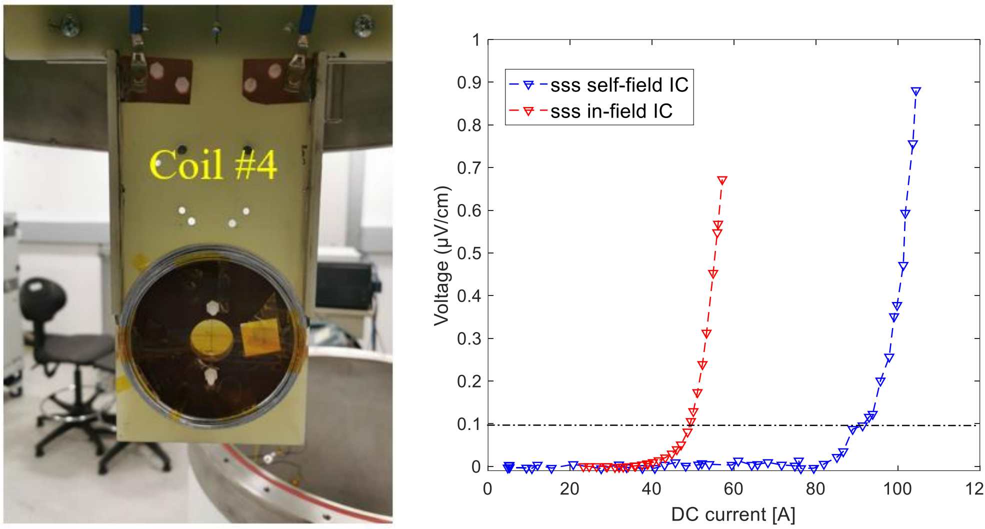

Figure 5.19. Picture of Coil #4 and its critical current with self-field and in-field (0.45 T).

Table 5.5. Specifications of Coil #2 and Coil #4

	Coil #2	Coil #4
HTS type	Sunam SAN04150	Sunam SAN04150
Coil Length	15.5 m	15.5 m
Coil inner/outer diameter	98 mm/103 mm	98 mm/112.0 mm
Total number of turns	50	56
Coil inductance	440 μH	449 μH
Tape width	4 mm	1 mm
Single wire Ic @77 K	150 A	150 A (4mm tape before cutting)
Self-field Ic @77 K	102 A	91 A
In-field Ic (0.45 T @77 K)	59 A	49 A
Insulation	Kapton tape	Heat-shrink tube

The normalized transport loss versus normalized transport current was measured by the electrical method, as shown in Figure 5.20. According to our AC power supply's limit, the frequencies are chosen at 36 Hz and 72 Hz, and the results are shown by normalized AC loss (Joule/cycle/m). The results indicate that the transport AC loss of both coils is frequency independent. According to the normalized transport AC loss results, the transport loss of the 3S coil is 40% lower than the normal 4mm coil.

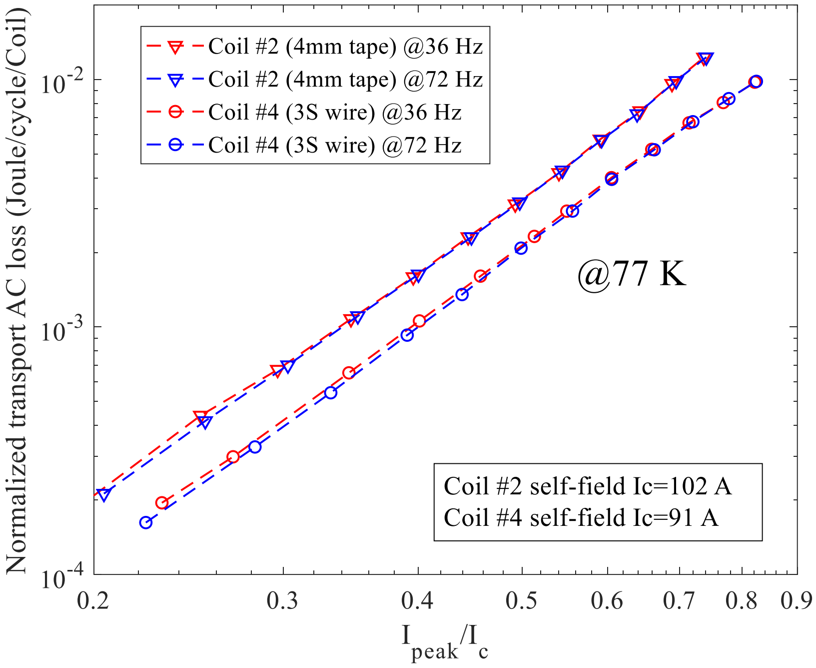

Figure 5.20. Transport loss of Coil #2 and Coil #4 measured by electrical method.

The magnetisation loss of Coil #4 in a 0.45 T rotational magnetic field is shown in Figure 5.21, at 10 Hz, for 3S wire coil, the magnetisation loss is 3.39 W. While the normal 4 mm tape coil is 2.82 W, due to more soldering used in the 3S coil the magnetisation loss is only 0.57 W higher than normal 4 mm coil at 10 Hz, which is 0.057 Joule/cycle. The magnetisation loss can be reduced by reducing soldering used in 3S wire fabrication.

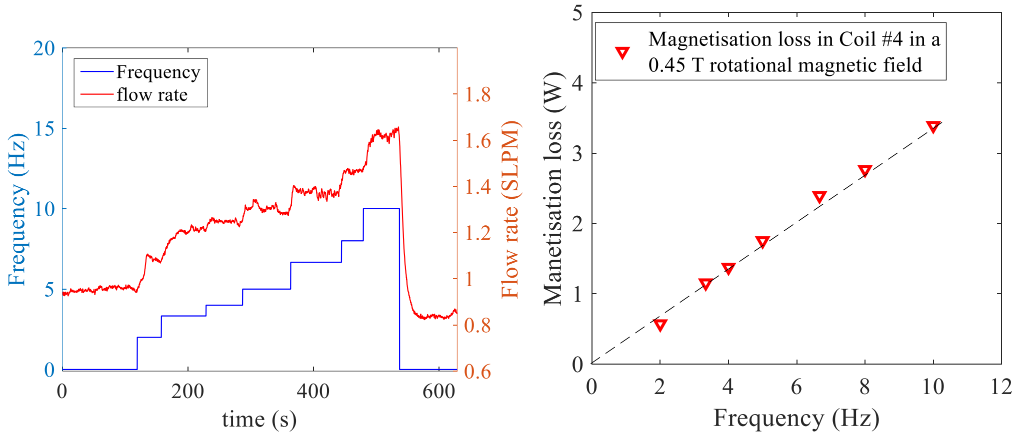

Figure 5.21. Magnetisation loss of Coil #4 in 0.45 T rotational magnetic field.

The total AC loss versus normalized current was measured by the calorimetric method are shown in Figure 5.22. The maximum rotational speed is 300 RPM due to the limitation of the bearing in 77 K, which means a 10 Hz output. Thus, the frequencies are set at 5 Hz and 10 Hz, and the transport currents are chosen from 10 A to 50 A. In our machine, the rotor generates a peak of 0.45 T rotational magnetic field. According to the normalized total AC loss results, the total AC loss of both coils are frequency independent, and the total loss of Coil #4 is 26% lower than Coil #2.

To sum up, the 3S coil can reduce the total loss by 26% and also reduce transport loss by 40%. The magnetisation loss increase is only 0.057 W/cycle due to more soldering used during wire manufactured. Thus, the 3S coil can reduce transport loss and total loss in the HTS stator. With a developing manufacturing technique for tape cutting, lower critical current loss and lower magnetisation loss can be reached. 3S wire has the potential to reduce total loss by more than 40%.

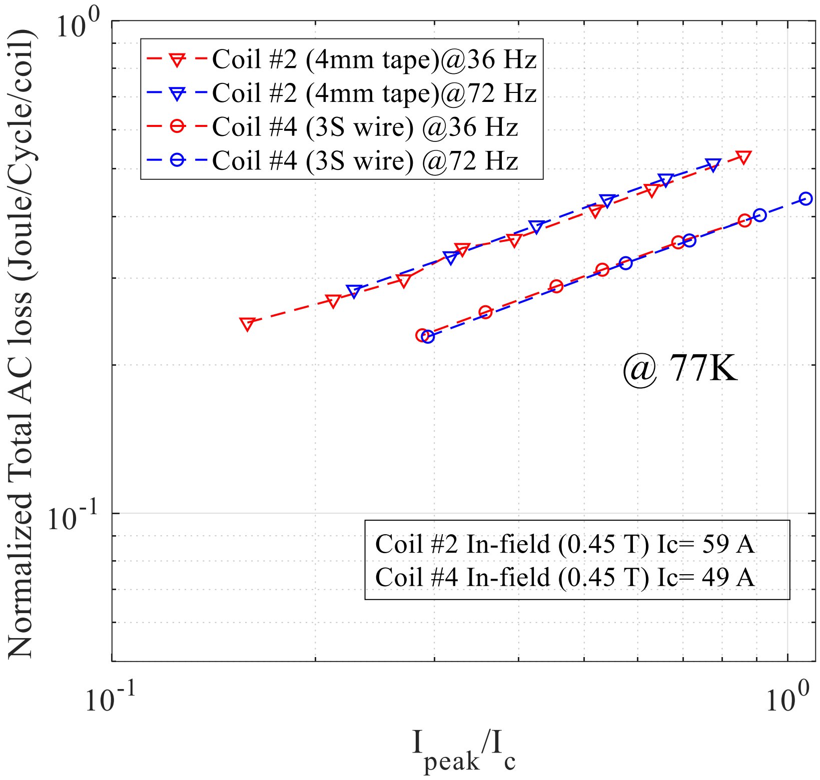

Figure 5.22. Total loss of Coil #2 and Coil #4 measured by calorimetric method.

5.5 Conclusions

We have developed a platform for HTS coils in machine environments. Several coils have been tested on this platform. We have studied the tape characteristics in the machine environment, and the good $J_c(B)$ characteristics of the tape can improve the AC loss performance in the machine environment. We measured the magnetisation loss and total loss of a variety of 2G HTS double pancake coils in the machine environment and demonstrated that 3S wire can reduce AC loss in machine design.

The measurement for total AC losses in Figure 5.11 was performed in a generator mode, so the transport current and the rotational magnetic field are in phase. According to the previous study [36], the phase angle between the transport current and the external magnetic field affects the total AC losses. When the current and magnetic field are in phase, the total AC loss is the highest. Thus, in machine operation, the in-phase experiment results can be used in thermal design.

Chapter 6 Influence of a Rectifier on HTS machine

This chapter reports a demonstration platform of a cryogenic rectifier at liquid nitrogen temperature. A high temperature superconducting (HTS) machine is connected with a cryogenic power rectifier in a generator mode to prove the feasibility of a cryogenic propulsion unit for electric aircraft propulsion applications. There is a possibility to test the impact of power electronic devices on the AC losses of HTS stator by connecting them together and measuring AC losses. Machine operation was carried out with a particular focus on the total heat dissipation inside the HTS AC windings. The transient operation was carried out to represent a short-circuit failure in one of the power electronic devices. The test shows AC loss performance of the HTS windings using the calorimetric method during the short circuit event, indicating the importance of developing protection schemes for the cryogenic propulsion units to prevent damage to the HTS components. This chapter provides initial insights into the interaction between superconducting machines and cryogenic power electronics within a cryogenic propulsion unit. It serves as an essential first step to understand and to further develop the cryogenic propulsion technology for future electric aircraft.

6.1 Introduction

Assuming that fully HTS machines can meet power density requirement, a cryogenic power network is still required to transfer the propulsion electricity. HTS generators, HTS motors, HTS cables are required to operate at cryogenic temperature. Considering the efficiency of the cryo-refrigerator, a closed-loop cooling system would be used to ensure reliability and increase the efficiency of the cryogenic cooling systems [32, 168, 169]. This means power electronic devices would also run in cryogenic operating temperature (25 - 77 K). In this propulsion system, the cryogenic temperature would improve the heat dissipation of these power electronic devices, and significantly increase the power density and enhance the reliability [170, 171]. Currently, key network components, including superconducting machine, superconducting cables and cryogenic power electronics have been studied [29, 157, 169, 172, 173]. Operating power electronic devices at cryogenic temperatures can reduce the temperature gradient experienced in the network and minimise the cooling requirement for all systems. However, the feasibility of operating power electronic devices at cryogenic temperatures in conjunction with superconducting machines has not been proved, although individual device tests have been done at cryogenic temperatures [171].

This Chapter is organised into four sections. The second section introduces a novel HTS demonstrating machine which allows the measurement of HTS armature coil AC losses. Chapter 6.2 introduced the testing platform, a cryogenic rectifier was connected with the HTS machine. Chapter 6.3 analyses the transient test results, which led to the quench of the HTS armatures. The first-of-its-kind results demonstrate in this chapter show the feasibility of a cryogenic propulsion unit. It also reveals the importance to develop protection functions for such a novel unit. The final section is the summary and conclusion.

6.2 A novel cryogenic propulsion testing platform

The whole platform for a cryogenic propulsion unit has been developed [160]. In this setup, the total AC loss can be measured by the calorimetric method [104, 105, 137, 158, 159, 174, 175]. Figure 6.1 shows the platform, which consists of a conventional DC motor, an axial-flux HTS machine in generator mode, a cryogenic power electronic testing chamber and a control/data acquisition system. Consequently, the DC machine drives the HTS machine as a generator. The three-phase output from the HTS machine is connected to a cryogenic power rectifier, feeding DC electricity into power resistances, as shown in Figure 6.1.

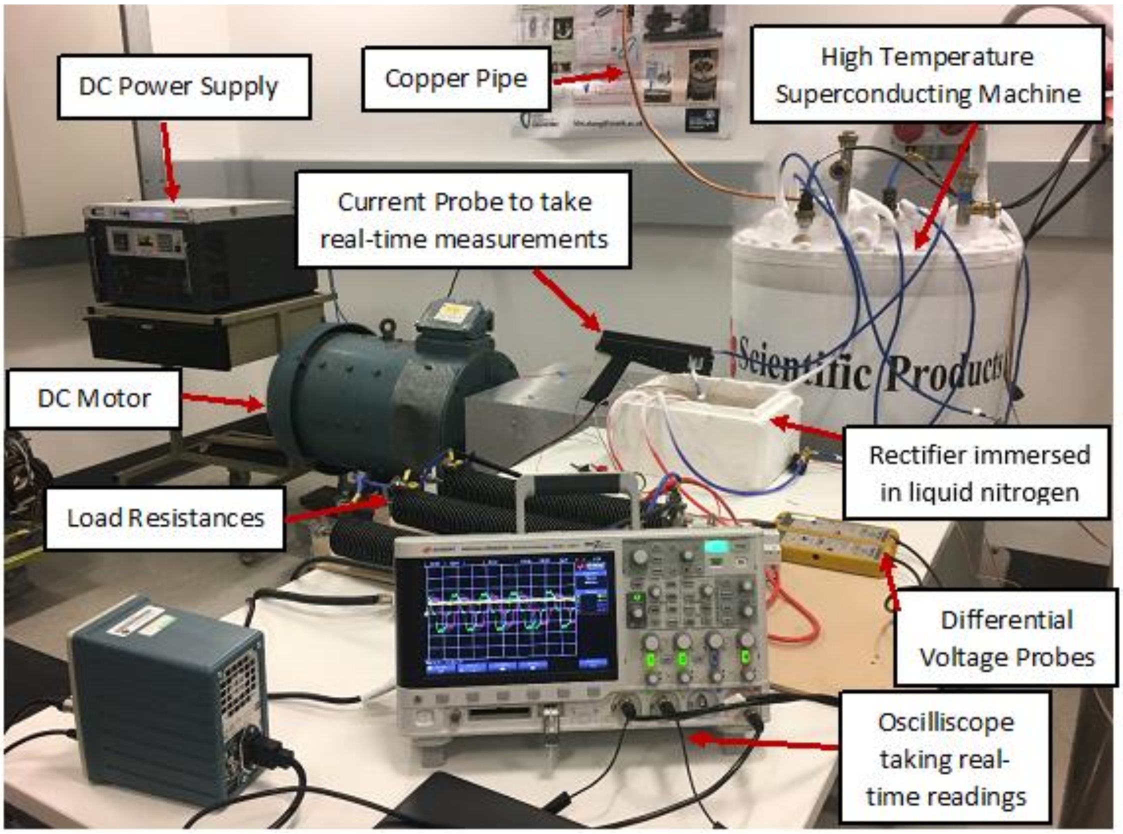

Figure 6.1. Cryogenic propulsion unit test platform

6.2.1 Cryogenic power rectifier

A full-bridge three-phase rectifier was developed and tested in LN_2. The diode chosen is a Silicon fast recovery type made by Microsemi® (type APT2X101DQ120J). Different types of the diode, including Silicon, Silicon Carbide Schottky and Fast Recovery Epitaxial Diodes, have been tested at cryogenic and room temperature by Abdelrahman Elwakeel at the University of Strathclyde. However, this particular diode has been chosen as it offers low power dissipation at cryogenic temperatures. The forward voltage of the diode was measured at 25 A at both room temperature and 77 K and there was found to be a significant reduction, from 1.6 V at room temperature to 1.3 V at 77 K. This would result in a reduction of the power losses of the rectifier at cryogenic temperatures.

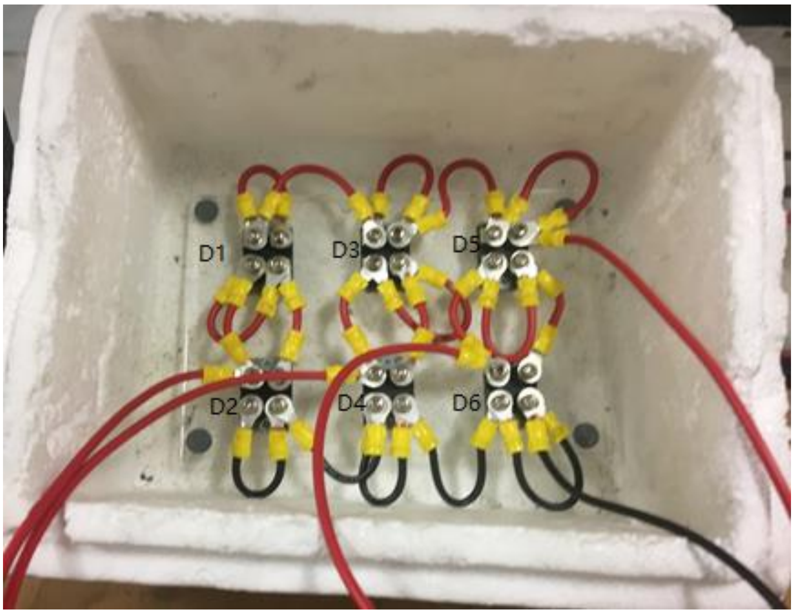

Figure 6.2. Rectifier of 6 diodes.

6.2.2 System operation circuit

Figure 6.3 shows the system circuit. The system operates in a generator mode, with a three-phase output from the HTS machine (Phase *A* is superconducting). During steady-state operation, the HTS machine is connected to the three-phase rectifier, which is cooled down by liquid nitrogen. The rectifier is connected with/without an *LC* filter circuit to a resistive load bank. To study transient operation, a short-circuit was introduced across *D4*. A low pass filter, consisting of an inductor *L1* and a capacitor *C1*, as shown in Figure 6.2, has been added to reduce the oscillations in the output current and voltage. The inductance has been chosen at 40 µH and the capacitance at 1 µF due to the relatively low operating speed of the system. The parameters measured during the tests include the total nitrogen gas boil-off rate (the total AC loss) in an HTS coil in Phase *A*, the three-phase voltage/current, the load current, as well as the rotational speed of the system.

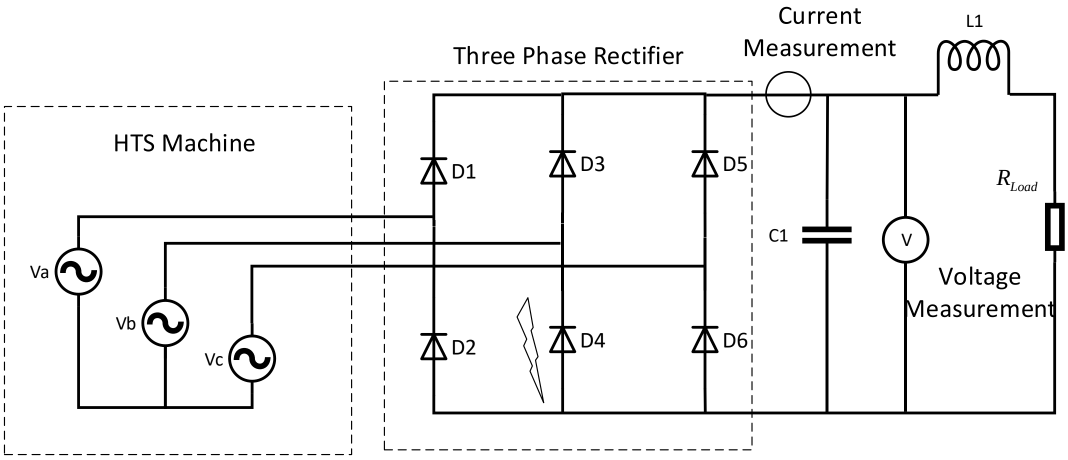

Figure 6.3. Circuit diagram of the cryogenic propulsion unit.

6.3 Transient analysis of the propulsion unit

The system was operated at 240 RPM in generator mode. Before commencing rotation, the HTS machine and the rectifier were fully cooled down to 77 K by LN_2. The speed control of the rotational shaft was implemented via the separately excited DC motor by adjusting the DC power supply input. Figure 6.4 shows the measured operating voltages and the load voltage. The imbalance in the voltage outputs is due to the geometry difference between Phase *A* (HTS tape windings) and Phases *B* and *C* (copper wire windings).

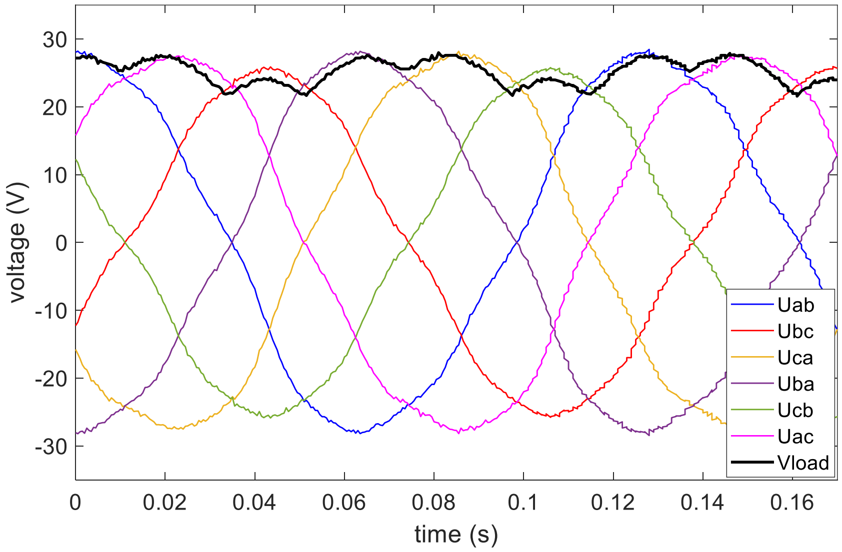

Figure 6.4. No-load output three-phase armature voltage and the load voltage at 240 RPM.

Both tests were carried out for comparison: the rectifier with and without the *LC* filter. The nitrogen boil-off rate in both cases was measured in order to understand the impacts of the filter on the HTS AC losses. Figure 6.5 shows the comparison of the results. Figure 6.5 (a) indicates the nitrogen gas boil-off rate versus load current without filter; Figure 6.5 (b) illustrates the nitrogen gas boil-off rate versus load current with filter. When there is a load current output, a corresponding nitrogen flow rate indicates the amount of heat or AC loss generated inside one HTS coil. When the experiment was switched off at 45 s, the flow rate was reduced to a background flow level, which is usually around 0.5 - 0.8 SLPM. The sensitivity of the measurement method and system validation can be found in Chapter 3 as well as in [160]. It is shown that with the filter, the oscillations in the load current were reduced and the overall load current drawn increased. This is because the filter has attenuated the harmonics otherwise introduced by the rectifier. The increase in the current drawn has increased the total AC loss of the HTS coil. The results show that the total AC loss from a single HTS armature coil increases from 3.54 W to 3.93 W when the filter is connected with the system.

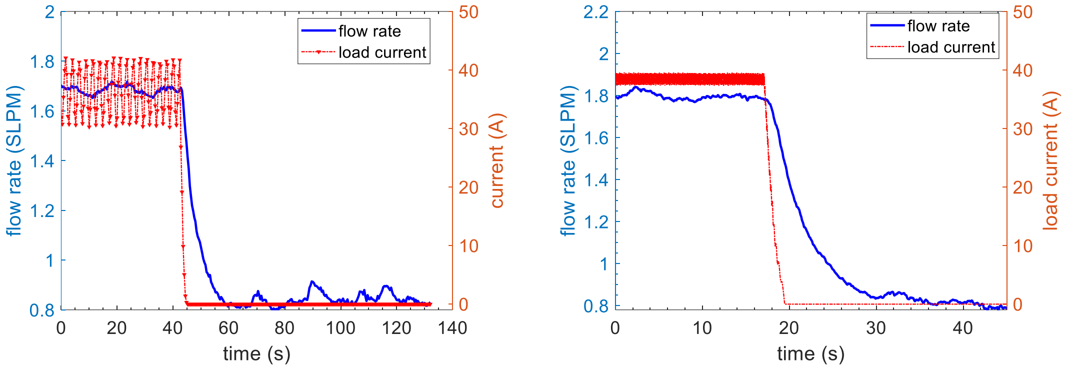

Figure 6.5. (a) Measured nitrogen flow rate and the corresponding load current without the LC filter; (b) nitrogen flow rate and load current measured with filter.

A sudden short-circuit in a cryogenic propulsion network can have serious impacts on superconducting machines and the whole aircraft electrical system. It can potentially happen when there is a device or insulation failure in the cryogenic environment, leading to permanent damage of HTS windings and consequently affecting the performance of the whole system. In this section, the effect of a short circuit event at the power electronics side of the propulsion unit, which can be caused by the failure of a diode, is studied both experimentally and numerically.

As shown in Figure 6.3, a short-circuit was introduced across *D4* at approximately 0.5 s. When the short-circuit event occurs, there was a loud sound from the machine, indicating a quench event happening. The nitrogen gas boil-off rate increases dramatically, as shown in Figure 6.6, which indicated the coil loss increase from 1.01W to 28.5W. The HTS coil was inspected physically and electrically afterwards. There was no obvious burn out sign of the coil due to the quench induced by the short-circuit. However, the outermost layer of the coil has been deformed slightly due to unbalanced Lorentz forces during the short-circuit. The critical current of the measured HTS coil tested and the result remains the same, but the AC loss values are 28 times higher than before the short-circuit event. This indicates that weak points have been introduced into the coil, caused potentially by the unbalanced Lorentz forces or the large amount of heat generated during the quench.

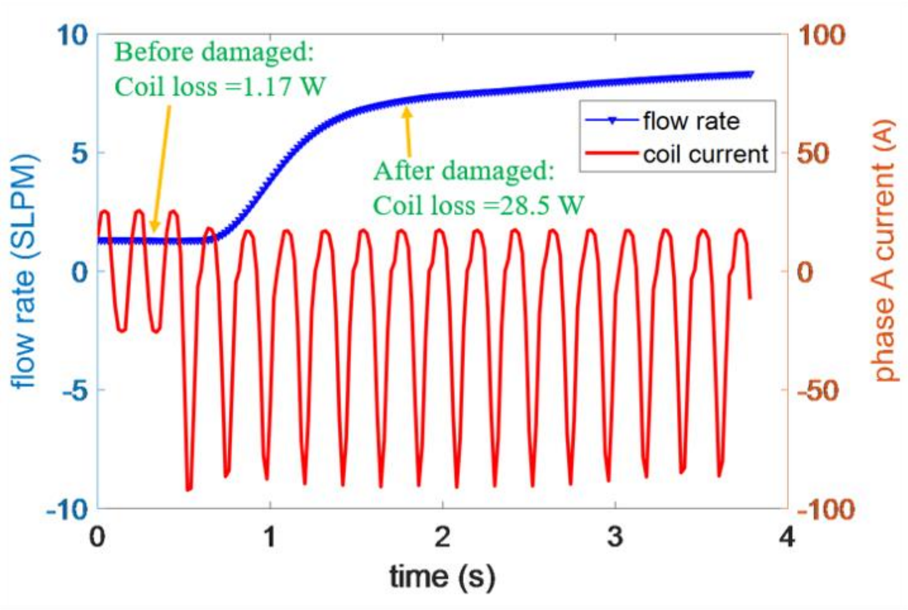

Figure 6.6. Phase A current during the short-circuit event and the corresponding nitrogen gas boil-off rate measured by the flow meter.

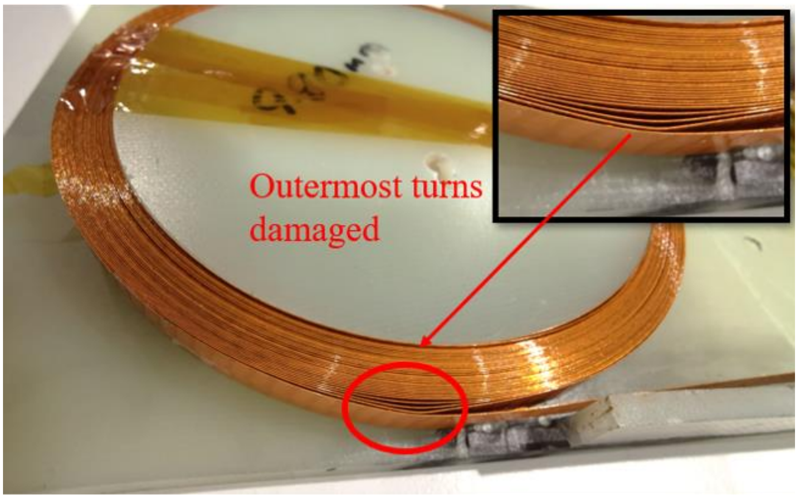

Figure 6.7. Damaged coil after quench.

Figure 6.8 shows the phase-phase output voltages and the load voltage before and immediately after the short-circuit event. The sample rate is 50 samples/s due to *DAQ* system limitations. During the experiment, diode D_4 was short-circuited as seen in Figure 6.3, meaning that when V_b is larger than V_a or V_c, there is a short-circuit across line voltage V_{ba} and V_{bc}, which in return would cause very large current passing through the phases, and eventually causing the superconducting coil in Phase *A* to quench.

To better understand what happened during the short-circuit event, we performed a MATLAB simulation. The parameters that were measured directly from the system are listed in Table 6.1. The simulation simplifies the quench progress of HTS windings by ignoring the quench propagation process, and uses two resistance values to represent the HTS winding before and after the quench, respectively. Good agreements between experiment and simulation have been found, as shown in Figure 6.9 and Figure 6.10.

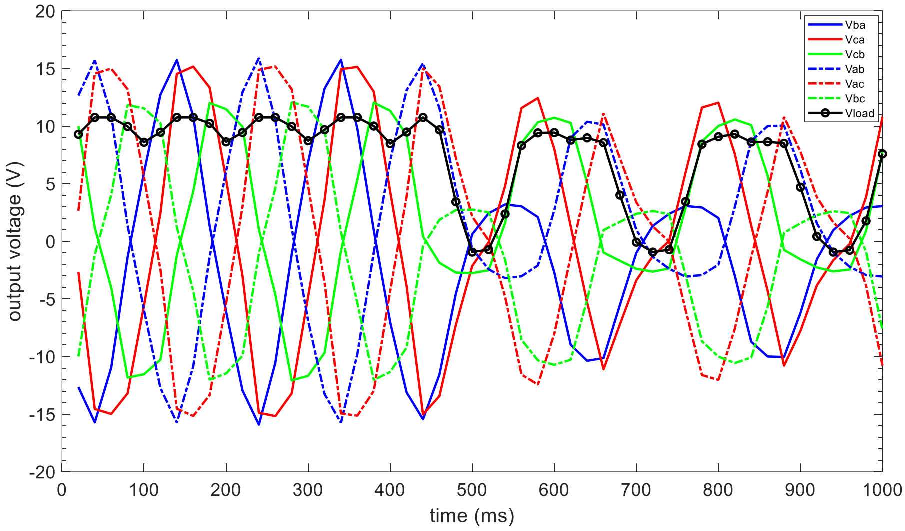

Figure 6.8. Measured voltages during the short-circuit event.

Table 6.1. Parameters used in system simulation

Symbols	Descriptions	Value
R_{Load}	Measured resistance for the load resistance bank	0.33 Ω
$R_{HTS\ Coil}$	Measured resistance for the HTS coil joints	$2\ \mu\Omega$
R_{quench}	Equivalent resistance after the HTS coil quenches	$60\ m\Omega$
$R_{copper\ Coil}$	Measured resistance for copper coils	$98\ m\Omega$

Figure 6.9 shows a comparison between the experimental and simulation results for the output voltages. When the short-circuit happens, the negative half cycles of V_{ab} are around -3 V, corresponding to voltage drops from D_2 and the copper cables when an overcurrent flowed from phase *B* to phase *A*. Similarly, the positive half cycles of V_{bc} are around 3 V, corresponding to voltage drops from D_6 and the copper cables when an overcurrent flowed from phase *B* to phase *C*. V_{ca} is largely unaffected. The slight drop in voltage is the result of the slowing down of the DC machine from 150 RPM to 136.5 RPM. This results in the peak induced EMF being reduced from 15 V to 12 V. A similar voltage drop is also observed in the positive half cycles of V_{ab} and the negative half cycles of V_{bc}.

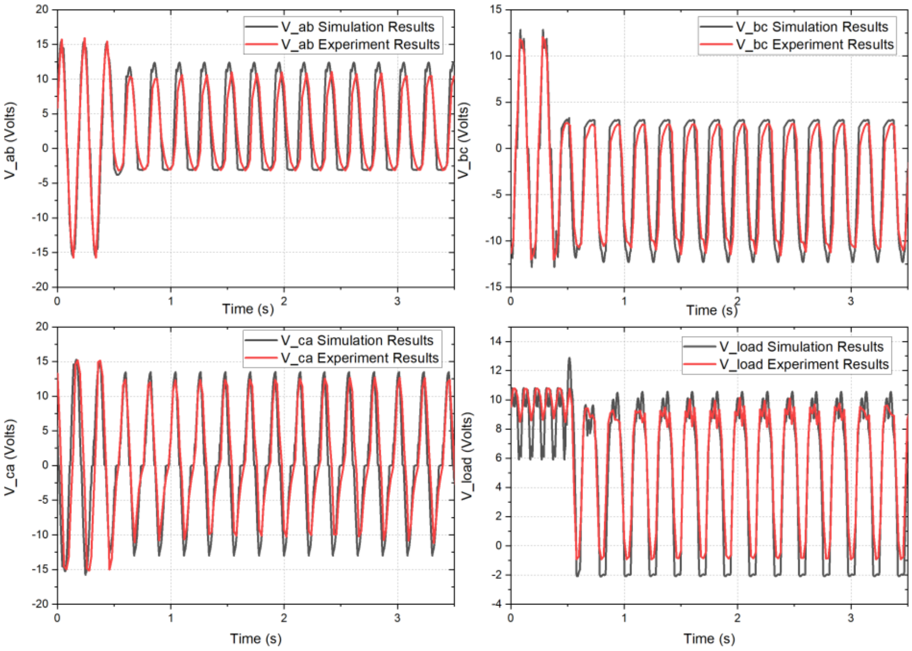

Figure 6.9. Measured voltages during the short-circuit event.

Figure 6.10 shows the comparison between experimental results and simulation for the measured load current and Phase *A* current. During the pre-fault period, the load current had small oscillations around 25 A. After the fault, the load current has been significantly reduced, as seen in Figure 6.8. The peak Phase *A* current is approximately -80 A to -90 A for the negative half cycles. This is much higher than the critical current of the HTS coil, which is 53 A under the rotational field conditions. Consequently, the HTS coil quenches, leading to the large nitrogen boil-off rate, as shown in Figure 6.6. The Phase *A* current is asymmetric, because the short-circuit only happens when V_b is higher than V_a and $\mathrm{V_c}$. For positive half-cycles, the slight reduction in the Phase A current is the result of EMF reduction.

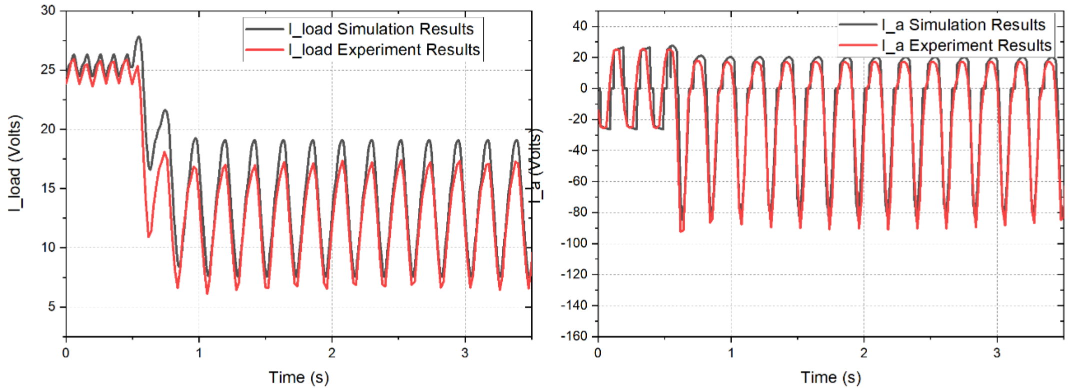

Figure 6.10. Comparison between experiment and simulation for the load current I_{load} and phase *A* current *Ia*.

6.4 Conclusions

We have developed a testing platform for cryogenic propulsion applications. This chapter reports the test on the cryogenic propulsion unit in both steady/transient conditions. The advantage of the platform is that the total AC loss of the HTS armature can be measured whilst connected to different types of power electronics to study the system impact on the HTS machine efficiency. More importantly, how the HTS machine reacts in a transient condition from the network point of view can also be tested. The steady operation confirms that the filter circuit has an impact on the efficiency of HTS machines. The transient operation confirms that the HTS machine windings are subjected to damage when there is a short-circuit event in the propulsion network. Fast response protection schemes for HTS machines will need to be investigated.

Chapter 7 Conclusion

7.1 Thesis summary

This thesis presented the research on the fully superconducting machine for power application purposes, including the stator design and the rotor design. Some experiments and models have been proposed and studied in order to explain coil performance in a machine environment. For electrical machine application in electrified aircraft, the power density need to be significantly increased. Thus the coil AC losses should be appropriately addressed and evaluated, and this is one of the primary factors for machine design and cryogenic cooling systems design. The outputs of HTS coils' performance in the machine environment can push the HTS machine forward to possible large-scale applications.

In Chapter 2, some fundamental theories of superconductivity were explained. This chapter demonstrates the understanding of different types of superconductors, critical temperature, critical current, AC loss theory, and AC loss measurement methods. These theories are the methodological foundation for the following researches. In this chapter, HTS conductor types and HTS coil types are also demonstrated in detail. This chapter illustrates the literature review of superconducting machines. Furthermore, this chapter shows the review of the insulated coil and NI coil, and the fundamental theories of NI coil are also discussed in this chapter.

In order to study coil performance in machine environments, the researches were separated into two parts: one permanent magnet machine testing rig to study the HTS stator coil in a rotational magnetic field; and an NI coil testing rig to study the HTS rotor coil in the ripple magnetic field. This study mainly focuses on the coil AC losses in the machine environment to provide data for fully size HTS machine design.

Chapter 3 demonstrated the setup of the stator windings testing rig. This chapter provided discussions for the design rationale and concepts. In the stator winding testing rig, a rotational magnetic field is provided by a permanent magnet rotor. The measured HTS stator coil is sitting in a measurement chamber. The coil loss can be measured by the boil-off method with a flowmeter. This chapter introduces the machine setup, calibration and systems validation of a 10 kW axial-flux fully superconducting machine. This system can measure either magnetisation AC loss and total loss for a 2G HTS stator coil. These results offer much data for large-scale superconducting machine design and provide a platform for different types of HTS coils to act further AC loss reduction research.

Chapter 4 demonstrates the study on NI coil for rotor design, the rotor coil is regarded as a circuit network unit, and the background field is provided by a copper coil. The magnetic flux density can be measured by a hall sensor in order to validate the circuit network model. A circuit network model of the rotor's design using NI coils was introduced. This model indicated the NI coils performance in AC magnetic field environments, and this model is validated by experiment. This part presents the simulation and experimental results of a NI coil in a uniform AC ripple field, indicated the rotor performance in a machine environment. In this chapter, the current distribution in the rotor winding is discussed. The maximum induced current in the NI coil is influenced by the amplitude and frequency of the background field. A higher amplitude or frequency of the ripple field would induce a higher induced current in the NI coil. The current distribution is also influenced by the coil turn-to-turn resistivity. To protect the coil in the machine rotor, the above factor needs to be considered in machine design.

In Chapter 5, the manufacturing process of 2G HTS coils for the HTS machine is demonstrated. This part also includes the necessary experimental results of 2G double pancake HTS coils. In this chapter, discussions of different types of the coil are demonstrated in detail. This part also provided experimental data for different types of

HTS stator coils to help identify the AC loss reduction techniques. These results can support AC loss researches in the future superconducting machine and all HTS systems design. Finally, in this chapter, a multi-filament superconducting wire is validated to reduce the coil AC loss in the stator effectively. The results of transport loss, magnetisation loss and total loss in a rotational magnetic field are demonstrated. These results are also compared with a normal 4 mm tape.

Chapter 6 introduces a novel cryogenic propulsion testing platform to connects the superconducting generator with the cryogenic power rectifier, the generator parts are demonstrated in Chapter 3. A high temperature superconducting (HTS) machine is connected with a cryogenic power rectifier in a generator mode to prove the feasibility of a cryogenic propulsion unit for electric aircraft propulsion applications. Machine operation was carried out with a special focus on the total heat dissipation inside the HTS AC windings. This platform is to simulate the AC superconducting generator connected with power electronics in future aircraft. In this chapter, both the steady/transient state of the superconducting generator was tested, and a short-circuit event was studied to shows the HTS coil's performance when a diode failure. It also reveals the importance to develop protection functions for such a novel unit.

7.2 Future work

Future work will include a new helium cooling system to decrease the operating temperature by 25 K. The critical current can significantly increase. Also, the machine rotor needs to be redesigned to achieve higher rotational speed and higher air-gap magnetic field. The stator can also be redesigned by increasing the number of turns. These acts can improve the testing rig to a higher operating current, higher output voltage and higher operating frequency. Recently, more technologies to reduce coil AC loss are developed, and more structure of the coil, i.e. CORC® cable, can be measured in this platform. It is to be hoped that with the rapid development of HTS technologies, the fully HTS machine will be used in commercial power applications, finally, to help solve the energy issues.

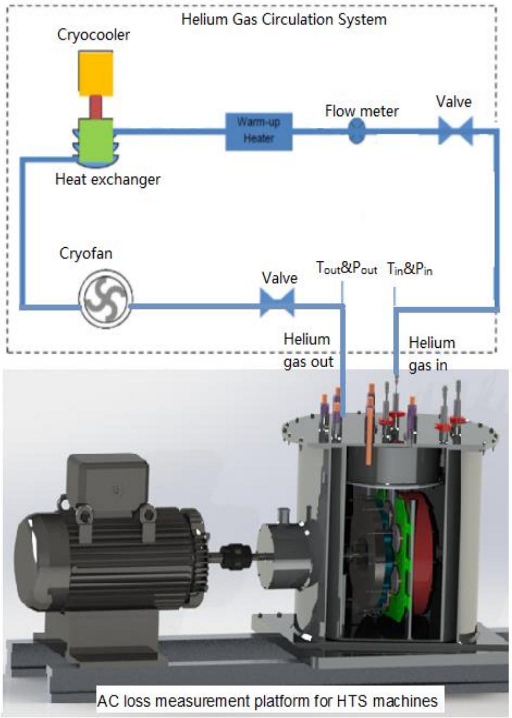

Figure 7.1. AC loss platform with the Helium gas circulation system

Machine upgrades:

- Speed increases from 300 RPM to 3000 RPM, operating frequency increases from 10 Hz to 100Hz
- Temperature from 77 K to 25 K by Helium gas cooling systems
- More types of HTS material can be tested, including MgB_2, more types of HTS wire can be tested, including CORC® cable.

References

[1] F. B. Silsbee, "A note on electrical conduction in metals at low temperatures," *Journal of the Washington Academy of Sciences,* vol. 6, no. 17, pp. 597-602, 1916.

[2] W. Meissner and R. Ochsenfeld, "Ein neuer effekt bei eintritt der supraleitfähigkeit," *Naturwissenschaften,* vol. 21, no. 44, pp. 787-788, 1933.

[3] E. Maxwell, "Isotope effect in the superconductivity of mercury," *Physical Review,* vol. 78, no. 4, p. 477, 1950.

[4] C. Reynolds, B. Serin, W. Wright, and L. Nesbitt, "Superconductivity of isotopes of mercury," *Physical Review,* vol. 78, no. 4, p. 487, 1950.

[5] J. G. Bednorz and K. A. Müller, "Possible highT c superconductivity in the Ba− La− Cu− O system," *Zeitschrift für Physik B Condensed Matter,* vol. 64, no. 2, pp. 189-193, 1986.

[6] C. Michel, L. Er-Rakho, and B. Raveau, "The oxygen defect perovskite BaLa4Cu5O13. 4, a metallic conductor," *Materials research bulletin,* vol. 20, no. 6, pp. 667-671, 1985.

[7] H. Takagi, S.-i. Uchida, K. Kitazawa, and S. Tanaka, "High-Tc Superconductivity of La-Ba-Cu Oxides. II.–Specification of the Superconducting Phase," *Japanese journal of applied physics,* vol. 26, no. 2A, p. L123, 1987.

[8] M.-K. Wu *et al.*, "Superconductivity at 93 K in a new mixed-phase Y-Ba-Cu-O compound system at ambient pressure," *Physical review letters,* vol. 58, no. 9, p. 908, 1987.

[9] K. S. Haran *et al.*, "High power density superconducting rotating machines—development status and technology roadmap," *Superconductor Science & Technology,* vol. 30, no. 12, p. 123002, 2017.

[10] H. Karmaker, D. Sarandria, M. T. Ho, J. Feng, D. Kulkarni, and G. Rupertus, "High-power dense electric propulsion motor," *IEEE Transactions on Industry Applications,* vol. 51, no. 2, pp. 1341-1347, 2014.

[11] T. Keim, T. Laskaris, J. Fealey, and P. Rios, "Design and manufacture of a 20 MVA superconducting generator," *IEEE Transactions on power apparatus systems,* no. 6, pp. 1474-1483, 1985.

[12] "Westinghouse Superconducting Generator Design," *Report EPRI EL-577, Project RP429,* 1977.

[13] B. B. Gamble and T. Keim, "High-power-density superconducting generator," *Journal of Energy,* vol. 6, no. 1, pp. 38-44, 1982.

[14] P. Tixador, Y. Brunet, P. Vedrine, Y. Laumond, and J. Sabrie, "Electrical tests on a fully superconducting synchronous machine," *IEEE transactions on magnetics,* vol. 27, no. 2, pp. 2256-2259, 1991.

[15] K. Yamaguchi *et al.*, "70 MW class superconducting generator test," *IEEE Transactions on applied superconductivity,* vol. 9, no. 2, pp. 1209-1212, 1999.

[16] S. S. Kalsi, "Development status of superconducting rotating machines," in *2002 IEEE Power Engineering Society Winter Meeting. Conference Proceedings (Cat. No. 02CH37309)*, 2002, vol. 1, pp. 401-403: IEEE.

[17] H. Neumüller *et al.*, "Advances in and prospects for development of high-temperature superconductor rotating machines at Siemens," vol. 19, no. 3, p. S114, 2006.

[18] W. Nick, M. Frank, G. Klaus, J. Frauenhofer, and H.-W. J. I. t. o. a. s. Neumuller, "Operational experience with the world's first 3600 rpm 4 MVA generator at Siemens," vol. 17, no. 2, pp. 2030-2033, 2007.

[19] J. Buck, B. Hartman, R. Ricket, B. Gamble, T. MacDonald, and G. Snitchler, "Factory testing of a 36.5 MW high temperature superconducting propulsion motor," *Fuel Tank to Target: Building the Electric Fighting Ship at American Society of Naval Engineers Day,* 2007.

[20] K. Sivasubramaniam *et al.*, "Development of a high speed HTS generator for airborne applications," *IEEE Transactions on applied superconductivity,* vol. 19, no. 3, pp. 1656-1661, 2009.

[21] S. Kalsi, "Ship propulsion motor employing Bi-2223 and MgB2 superconductors," in *Research, Fabrication and Applications of Bi-2223 HTS Wires*: World Scientific, 2016, pp. 427-449.

[22] IATA, "Aircraft Technology Roadmap to 2050," Available: https://www.iata.org/contentassets/8d19e716636a47c184e7221c77563c93/technology20roadmap20to20205020no20foreword.pdf.

[23] M. J. Armstrong, C. A. Ross, M. J. Blackwelder, and K. Rajashekara, "Propulsion system component considerations for NASA N3-X turboelectric distributed propulsion system," *SAE International Journal of Aerospace,* vol. 5, no. 2012-01-2165, pp. 344-353, 2012.

[24] NASA, "Aviation Renaissance: NASA Advances Concepts for Next-gen Aircraft," 2017, Available: https://www.nasa.gov/feature/aviation-renaissance-nasa-advances-concepts-for-next-gen-aircraft.

[25] (Accessed: SEP. 2021. [online]). *Sugar - Boeing: How sweet the future of aviation*. Available: https://www.boeing.com/features/innovation-quarterly/aug2017/feature-technical-sugar.page

[26] L. Juve, J. Fosse, E. Joubert, and N. Fouquet, "Airbus Group electrical aircraft program, the E-FAN project," in *52nd AIAA/SAE/ASEE Joint Propulsion Conference*, 2016, p. 4613.

[27] J. L. Felder, G. V. Brown, H. DaeKim, and J. Chu, "Turboelectric distributed propulsion in a hybrid wing body aircraft," 2011.

[28] G. Brown, "Weights and efficiencies of electric components of a turboelectric aircraft propulsion system," in *49th AIAA aerospace sciences meeting including the new horizons forum and aerospace exposition*, 2011, p. 225.

[29] C. A. Luongo *et al.*, "Next generation more-electric aircraft: a potential application for HTS superconductors," *IEEE Transactions on Applied Superconductivity,* vol. 19, no. 3, pp. 1055-1068, 2009.

[30] B. Sarlioglu and C. T. Morris, "More electric aircraft: review, challenges, and opportunities for commercial transport aircraft," *IEEE Transactions on Transportation Electrification,* vol. 1, pp. 54-64, 2015.

[31] L. Bertola, T. Cox, P. Wheeler, S. Garvey, and H. Morvan, "Superconducting electromagnetic launch system for civil aircraft," *IEEE Transactions on Applied Superconductivity,* vol. 26, no. 8, pp. 1-11, 2016.

[32] F. Berg, J. Palmer, P. Miller, M. Husband, and G. Dodds, "HTS electrical system for a distributed propulsion aircraft," *IEEE Transactions on Applied Superconductivity,* vol. 25, no. 3, pp. 1-5, 2015.

[33] A. S. Gohardani, G. Doulgeris, and R. Singh, "Challenges of future aircraft propulsion: A review of distributed propulsion technology and its potential application for the all electric commercial aircraft," *Progress in Aerospace Sciences,* vol. 47, no. 5, pp. 369-391, 2011.

[34] M. Henke *et al.*, "Challenges and opportunities of very light high-performance electric drives for aviation," *Energies,* vol. 11, no. 2, p. 344, 2018.

[35] R. Vepa, "Modeling and Dynamics of HTS Motors for Aircraft Electric Propulsion," *Aerospace,* vol. 5, no. 1, p. 21, 2018.

[36] M. Zhang, W. Yuan, J. Kvitkovic, and S. Pamidi, "Total AC loss study of 2G HTS coils for fully HTS machine applications," *Superconductor Science & Technology,* vol. 28, no. 11, p. 115011, 2015.

[37] M. Ainslie, M. Izumi, and M. Miki, "Recent advances in superconducting rotating machines: an introduction to the 'focus on superconducting rotating machines'," *Superconductor Science & Technology,* vol. 29, 2016.

[38] P. Song, T. Qu, L. Lai, M. Wu, X. Yu, and Z. Han, "Thermal analysis for the HTS stator consisting of HTS armature windings and an iron core for a 2.5 kW HTS generator," *Superconductor Science & Technology,* vol. 29, 2016.

[39] P. Eckels and G. Snitchler, "5 MW high temperature superconductor ship propulsion motor design and test results," *Naval Engineers Journal,* vol. 117, no. 4, pp. 31-36, 2005.

[40] W. Nick, J. Grundmann, and J. Frauenhofer, "Test results from Siemens low-speed, high-torque HTS machine and description of further steps towards commercialisation of HTS machines," *Physica C: Superconductivity and its Applications,* vol. 482, pp. 105-110, 2012.

[41] S. Li, Y. Fan, J. Fang, W. Qin, G. Lv, and J. Li, "HTS axial flux induction motor with analytic and FEA modeling," *Physica C,* vol. 494, pp. 230-4, 2013.

[42] T. Qu *et al.*, "Development and testing of a 2.5 kW synchronous generator with a high temperature superconducting stator and permanent magnet rotor," *Superconductor Science & Technology,* vol. 27, 2014.

[43] W. Cao, B. C. Mecrow, G. J. Atkinson, J. W. Bennett, and D. J. Atkinson, "Overview of electric motor technologies used for more electric aircraft (MEA)," *IEEE transactions on industrial electronics,* vol. 59, no. 9, pp. 3523-3531, 2011.

[44] (Accessed: Mar. 2016. [online]). *The Future of Electric Hybrid Aviation.* Available: http://www.machinedesign.com/batteriespowersupplies/future-electric-hybrid-aviation

[45] (2017). *Horizon 2020, Work Programme 2016–2017.*

[46] C. E. Jones, P. J. Norman, S. J. Galloway, M. J. Armstrong, and A. M. Bollman, "Comparison of Candidate Architectures for Future Distributed Propulsion Aircraft," *Ieee Transactions on Applied Superconductivity,* vol. 26, no. 6, Sep 2016, Art. no. 3601409.

[47] F. Berg, J. Palmer, P. Miller, and G. Dodds, "HTS System and Component Targets for a Distributed Aircraft Propulsion System," *IEEE Transactions on Applied Superconductivity,* vol. 27, no. 4, Jun 2017, Art. no. 3600307.

[48] X. Zhang, C. L. Bowman, T. C. O. Connell, and K. S. Haran, "Large electric machines for aircraft electric propulsion," *IET Electric Power Applications,* vol. 12, no. 6, pp. 767-779, 2018.

[49] I. D. Chasiotis and Y. L. Karnavas, "A Generic Multi-Criteria Design Approach Toward High Power Density and Fault-Tolerant Low-Speed PMSM for Pod Applications," *IEEE Transactions on Transportation Electrification,* vol. 5, no. 2, pp. 356-370, 2019.

[50] Y. Zhao *et al.*, "Progress in fabrication of second generation high temperature superconducting tape at Shanghai Superconductor Technology," vol. 32, no. 4, p. 044004, 2019.

[51] P. J. Masson, G. V. Brown, D. S. Soban, C. A. J. S. S. Luongo, and Technology, "HTS machines as enabling technology for all-electric airborne vehicles," vol. 20, no. 8, p. 748, 2007.

[52] R. Jansen, C. Bowman, and A. Jankovsky, "Sizing power components of an electrically driven tail cone thruster and a range extender," in *16th AIAA Aviation Technology, Integration, and Operations Conference*, 2016, p. 3766.

[53] W. Goldacker *et al.*, "ROEBEL assembled coated conductors (RACC): preparation, properties and progress," vol. 17, no. 2, pp. 3398-3401, 2007.

[54] D. C. van der Laan, "YBa2Cu3O7− δ coated conductor cabling for low ac-loss and high-field magnet applications," *Superconductor Science and Technology,* vol. 22, no. 6, p. 065013, 2009.

[55] Y. H. Choi *et al.*, "Thermal Quench Behaviors of No-Insulation Coils Wound Using GdBCO Coated Conductor Tapes With Various Lamination Materials," (in English), *IEEE Transactions on Applied Superconductivity,* Article vol. 24, no. 3, p. 5, Jun 2014, Art. no. 8800105.

[56] S. Choi, H. C. Jo, Y. J. Hwang, S. Hahn, and T. K. Ko, "A study on the no insulation winding method of the HTS coil," *IEEE transactions on applied superconductivity,* vol. 22, no. 3, pp. 4904004-4904004, 2011.

[57] U. Bong *et al.*, "A Design Study on 40 MW Synchronous Motor With No-Insulation HTS Field Winding," *IEEE Transactions on Applied Superconductivity,* vol. 29, no. 5, pp. 1-6, 2019.

[58] M. Cho *et al.*, "Combined Circuit Model to Simulate Post-Quench Behaviors of No-Insulation HTS Coil," *IEEE Transactions on Applied Superconductivity,* vol. 29, no. 5, pp. 1-5, 2019.

[59] S. Hahn *et al.*, "No-insulation multi-width winding technique for high temperature superconducting magnet," *Applied Physics Letters,* vol. 103, no. 17, Oct 21 2013, Art. no. 173511.

[60] S. Hahn, D. K. Park, J. Bascunan, and Y. Iwasa, "HTS Pancake Coils Without Turn-to-Turn Insulation," (in English), *Ieee Transactions on Applied Superconductivity,* Article vol. 21, no. 3, pp. 1592-1595, Jun 2011.

[61] X. D. Wang *et al.*, "Turn-to-turn contact characteristics for an equivalent circuit model of no-insulation ReBCO pancake coil," (in English), *Superconductor Science & Technology,* vol. 26, no. 3, Mar 2013.

[62] H. Park, A.-r. Kim, S. Kim, M. Park, K. Kim, and T. Park, "Mechanical and electric characteristics of vacuum impregnated no-insulation HTS coil," *Physica C: Superconductivity its Applications,* vol. 504, pp. 138-143, 2014.

[63] T. S. Lee *et al.*, "The effects of co-wound Kapton, stainless steel and copper, in comparison with no insulation, on the time constant and stability of GdBCO pancake coils," *Superconductor Science and Technology,* vol. 27, no. 6, p. 065018, 2014.

[64] K. Kim *et al.*, "Analytical and empirical studies on the characteristic resistances of no-insulation GdBCO racetrack pancake coil under various operating currents," *Current Applied Physics,* vol. 15, no. 1, pp. 8-13, 2015.

[65] K. Kim, Y. Choi, D. Yang, J. Song, and H. Lee, "Transient characteristics of a GdBCO racetrack pancake coil without turn-to-turn insulation," *Superconductor Science and Technology,* vol. 27, no. 1, p. 015001, 2013.

[66] Y.-G. Kim, D. G. Yang, J. Lee, W. J. Kim, S. H. Kim, and H. Lee, "Numerical analysis on bifurcated current flow in no-insulation magnet," *IEEE transactions on applied superconductivity,* vol. 24, no. 3, pp. 1-4, 2013.

[67] Y. Iwasa and S. Hahn, "First-cut design of an all-superconducting 100-T direct current magnet," *Applied Physics Letters,* vol. 103, no. 25, Dec 16 2013, Art. no. 253507.

[68] L. Prigozhin, "Analysis of critical-state problems in type-II superconductivity," *IEEE Transactions on Applied Superconductivity,* vol. 7, no. 4, pp. 3866-3873, 1997.

[69] Pia Jensen Ray. Figure 2.4 in Master's thesis, "Structural investigation of La(2–x)Sr(x)CuO(4+y) - Following staging as a function of temperature". Niels Bohr Institute, Faculty of Science, University of Copenhagen. Copenhagen, Denmark, November 2015. DOI:10.6084/m9.figshare.2075680.v2

[70] W. Buckel and R. Kleiner, *Superconductivity: fundamentals and applications*. John Wiley & Sons, 2008.

[71] D. Larbalestier, A. Gurevich, D. M. Feldmann, and A. Polyanski, "High-Tc superconducting materials for electric power applications," *Nature,* vol. 414, no. 6861, p. 368, 2001.

[72] L. D. Landau, *Collected papers of LD Landau*. Pergamon, 1965.

[73] J. Bardeen, L. N. Cooper, and J. R. Schrieffer, "Theory of superconductivity," *Physical review,* vol. 108, no. 5, p. 1175, 1957.

[74] Y. Iijima, K. Kakimoto, Y. Sutoh, S. Ajimura, and T. Saitoh, "Development of 100-m long Y-123 coated conductors processed by IBAD/PLD method," *Physica C: Superconductivity,* vol. 412, pp. 801-806, 2004.

[75] M. Rupich *et al.*, "Progress on MOD/RABiTSTM 2G HTS wire," *Physica C: Superconductivity,* vol. 412, pp. 877-884, 2004.

[76] E. Härö, A. Stenvall, J. van Nugteren, and G. Kirby, "Modeling of minimum energy required to quench an HTS magnet with a strip heater," *IEEE Transactions on Applied Superconductivity,* vol. 25, no. 6, pp. 1-5, 2015.

[77] J.-H. Joo, H. Sano, S. B. Kim, S. Murase, Y. K. Kwon, and H. M. Kim, "Development of quench detection method based on normal transition behaviors for HTS coils," *IEEE transactions on applied superconductivity,* vol. 19, no. 3, pp. 2415-2418, 2009.

[78] H. Kim, J. Kim, J. Lee, and T. K. Ko, "HTS coil with enhanced thermal stability in over-current operation for fast response magnet power application," *Superconductor Science and Technology,* vol. 28, no. 10, p. 105006, 2015.

[79] H. Kim, Y. Kwon, J. Lee, J. Song, and H. Lee, "Quench and recovery characteristics of a racetrack double pancake coil wound with YBCO-coated conductor," *Superconductor Science and Technology,* vol. 22, no. 2, p. 025014, 2009.

[80] J.-d. Lee *et al.*, "Thermal quench in HTS double pancake race track coil," *IEEE transactions on applied superconductivity,* vol. 17, no. 2, pp. 1603-1606, 2007.

[81] Y. Yanagisawa *et al.*, "The mechanism of thermal runaway due to continuous local disturbances in the YBCO-coated conductor coil winding," *Superconductor Science and Technology,* vol. 25, no. 7, p. 075014, 2012.

[82] F. Bergsma, P. Blanc, F. Garnier, and P. Giudici, "A High Precision 3D Magnetic Field Scanner for Small to Medium Size Magnets," *IEEE Transactions on Applied Superconductivity,* vol. 26, no. 4, pp. 1-4, 2016.

[83] C. Daversin, C. Prudhomme, and C. Trophime, "Full three-dimensional multiphysics model of high-field polyhelices magnets," *IEEE transactions on applied superconductivity,* vol. 26, no. 4, pp. 1-4, 2016.

[84] Y. Iwata, T. Shirai, and K. Noda, "Design of superconducting magnets for a compact carbon gantry," *IEEE Transactions on Applied Superconductivity,* vol. 26, no. 4, pp. 1-4, 2015.

[85] M. Kang, M. Ku, H. Lee, G. Cha, and K. Choi, "The Optimal Air Gap Between the Pancake Windings in a HTS Magnet Consisting of Insert and Outsert Magnet," *IEEE Transactions on Applied Superconductivity,* vol. 20, no. 3, pp. 1802-1805, 2010.

[86] E. Pardo, J. Šouc, and L. Frolek, "Electromagnetic modelling of superconductors with a smooth current–voltage relation: variational principle and coils from a few turns to large magnets," *Superconductor Science and Technology,* vol. 28, no. 4, p. 044003, 2015.

[87] J. Pelegrin, E. Young, and Y. Yang, "Numerical winding model for the analysis of superconducting insert coils," *IEEE Transactions on Applied Superconductivity,* vol. 25, no. 3, pp. 1-5, 2014.

[88] J. Hernandez-Llambes and D. Hazelton, "Advantages of second-generation high temperature superconductors for pulsed power applications," in *2009 IEEE Pulsed Power Conference*, 2009, pp. 221-226: IEEE.

[89] V. Selvamanickam, Y.-Y. Xie, and J. Reeves, "Progress in scale-up of 2G conductor at SuperPower," in *Superconductivity for Electric Systems 2008 DOE Annual Peer Review*, 2006, pp. 25-27.

[90] C. Barth, G. Mondonico, and C. Senatore, "Electro-mechanical properties of REBCO coated conductors from various industrial manufacturers at 77 K, self-field and 4.2 K, 19 T," *Superconductor Science and Technology,* vol. 28, no. 4, p. 045011, 2015.

[91] *'SuperPower® 2G HTS Wire Specifications*. Available: http://www.superpower-inc.com/content/wire-specification

[92] L. Prigozhin, "The Bean model in superconductivity: Variational formulation and numerical solution," *Journal of Computational Physics,* vol. 129, no. 1, pp. 190-200, 1996.

[93] J. Rhyner, "Magnetic properties and AC-losses of superconductors with power law current—voltage characteristics," *Physica C: Superconductivity,* vol. 212, no. 3-4, pp. 292-300, 1993.

[94] C. P. Bean, "Magnetization of high-field superconductors," *Reviews of modern physics,* vol. 36, no. 1, p. 31, 1964.

[95] W. Carr Jr, *AC loss and macroscopic theory of superconductors*. CRC press, 2001.

[96] F. Grilli *et al.*, "Superconducting motors for aircraft propulsion: the Advanced Superconducting Motor Experimental Demonstrator project," in *Journal of Physics: Conference Series*, 2020, vol. 1590, no. 1, p. 012051: IOP Publishing.

[97] S. Sahoo, X. Zhao, and K. Kyprianidis, "A review of concepts, benefits, and challenges for future electrical propulsion-based aircraft," *Aerospace,* vol. 7, no. 4, p. 44, 2020.

[98] H. Zhang, Z. Wen, F. Grilli, K. Gyftakis, and M. Mueller, "Alternating Current Loss of Superconductors Applied to Superconducting Electrical Machines," *Energies,* vol. 14, no. 8, p. 2234, 2021.

[99] F. Grilli, E. Pardo, A. Stenvall, D. N. Nguyen, W. Yuan, and F. Gömöry, "Computation of losses in HTS under the action of varying magnetic fields and currents," *IEEE Transactions on Applied Superconductivity,* vol. 24, no. 1, pp. 78-110, 2013.

[100] Y. Wang, X. Guan, and J. Dai, "Review of AC loss measuring methods for HTS tape and unit," *IEEE Transactions on Applied Superconductivity,* vol. 24, no. 5, pp. 1-6, 2014.

[101] J.-H. Kim, C. H. Kim, G. Iyyani, J. Kvitkovic, and S. Pamidi, "Transport AC loss measurements in superconducting coils," *IEEE Transactions on Applied Superconductivity,* vol. 21, no. 3, pp. 3269-3272, 2011.

[102] M. D. Ainslie *et al.*, "Transport AC Loss Measurements of a Triangular, Epoxy-Impregnated High Temperature Superconducting (HTS) Coil," 2017: Institute of Electrical and Electronics Engineers.

[103] W. Carr, "AC loss from the combined action of transport current and applied field," *IEEE Transactions on Magnetics,* vol. 15, pp. 240-3, 1979.

[104] S. Ashworth and M. Suenaga, "The calorimetric measurement of losses in HTS tapes due to ac magnetic fields and transport currents," *Physica C,* vol. 315, pp. 79-84, 1999.

[105] T. Hardono, C. D. Cook, and J. X. Jin, "Measurements of AC losses in HTSC wires exposed to an alternating field using calorimetric methods," *IEEE Transactions on Applied Superconductivity,* vol. 9, pp. 813-6, 1999.

[106] D. Daney, H. Boenig, M. Maley, D. McMurry, and B. DeBlanc, "AC loss calorimeter for three-phase cable," *IEEE Transactions on Applied Superconductivity,* vol. 7, pp. 310-3, 1997.

[107] J. Ekin, *Experimental techniques for low-temperature measurements: cryostat design, material properties and superconductor critical-current testing*. Oxford university press, 2006.

[108] N. Amemiya *et al.*, "AC loss reduction of YBCO coated conductors by multifilamentary structure," *Superconductor Science and Technology,* vol. 17, no. 12, p. 1464, 2004.

[109] M. D. Sumption, P. N. Barnes, and E. W. Collings, "AC losses of coated conductors in perpendicular fields and concepts for twisting," *IEEE transactions on applied superconductivity,* vol. 15, no. 2, pp. 2815-2818, 2005.

[110] M. Marchevsky, E. Zhang, Y. Xie, V. Selvamanickam, and P. G. Ganesan, "AC losses and magnetic coupling in multifilamentary 2G HTS conductors and tape arrays," *IEEE transactions on applied superconductivity,* vol. 19, no. 3, pp. 3094-3097, 2009.

[111] F. Grilli and A. Kario, "How filaments can reduce AC losses in HTS coated conductors: a review," *Superconductor Science & Technology,* vol. 29, 2016.

[112] M. Halse, "AC face field losses in a type II superconductor," *Journal of Physics D: Applied Physics,* vol. 3, no. 5, p. 717, 1970.

[113] E. H. Brandt and M. Indenbom, "Type-II-superconductor strip with current in a perpendicular magnetic field," *Physical review B,* vol. 48, 1993.

[114] E. Zeldov, J. R. Clem, M. McElfresh, and M. Darwin, "Magnetization and transport currents in thin superconducting films," *Physical Review B,* vol. 49, no. 14, p. 9802, 1994.

[115] M. Wang *et al.*, "An effective way to reduce AC loss of second-generation high temperature superconductors," *Superconductor Science & Technology,* vol. 32, no. 1, p. 01LT01, 2018.

[116] M. Oomen, W. Herkert, D. Bayer, P. Kummeth, W. Nick, and T. Arndt, "Manufacturing and test of 2G-HTS coils for rotating machines: Challenges, conductor requirements, realization," (in English), *Physica C-Superconductivity and Its Applications,* Article vol. 482, pp. 111-118, Nov 2012.

[117] X. Song *et al.*, "Ground Testing of the World's First MW-Class Direct Drive Superconducting Wind Turbine Generator," *IEEE Transactions on Energy Conversion,* pp. 1-1, 2019.

[118] H. H. Song, K. Gagnon, and J. Schwartz, "Quench behavior of conduction-cooled YBa2Cu3O7-delta coated conductor pancake coils stabilized with brass or copper," (in English), *Superconductor Science & Technology,* Article vol. 23, no. 6, p. 10, Jun 2010, Art. no. 065021.

[119] T. Shen, L. Ye, D. Turrioni, and P. Li, "High-field quench behavior and dependence of hot spot temperature on quench detection voltage threshold in a

Bi2Sr2CaCu2Ox coil," *Superconductor Science and Technology,* vol. 28, no. 7, p. 075014, 2015.

[120] L. Ye, P. Li, T. Shen, and J. Schwartz, "Quench degradation limit of multifilamentary Ag/Bi2Sr2CaCu2Ox round wires," *Superconductor Science and Technology,* vol. 29, no. 3, p. 035010, 2016.

[121] Y. Wang, J. Zheng, Z. Zhu, M. Zhang, and W. Yuan, "Quench behavior of high-temperature superconductor (RE)Ba2Cu3O x CORC cable," *Journal of Physics D: Applied Physics,* vol. 52, no. 34, p. 345303, 2019/06/24 2019.

[122] H. Song and J. Schwartz, "Stability and Quench Behavior of YBa2Cu3O7-x Coated Conductor at 4.2 K, Self-Field," *Ieee Transactions on Applied Superconductivity,* vol. 19, no. 5, pp. 3735-3743, Oct 2009.

[123] Y. Wang, W. K. Chan, and J. Schwartz, "Self-protection mechanisms in no-insulation (RE) Ba2Cu3O x high temperature superconductor pancake coils," *Superconductor Science & Technology,* vol. 29, no. 4, p. 045007, 2016.

[124] Y. Wang, M. Zhang, W. Yuan, Z. Hong, Z. Jin, and H. Song, "Non-uniform ramping losses and thermal optimization with turn-to-turn resistivity grading in a (RE) Ba2Cu3Ox magnet consisting of multiple no-insulation pancake coils," *Journal of Applied Physics,* vol. 122, no. 5, p. 053902, 2017.

[125] J. J. Scheidler and T. F. Tallerico, "Design, Fabrication, and Critical Current Testing of No-Insulation Superconducting Rotor Coils for NASA's 1.4 MW High-Efficiency Megawatt Motor," in *2018 AIAA/IEEE Electric Aircraft Technologies Symposium (EATS)*, 2018, pp. 1-9: IEEE.

[126] S. Yoon *et al.*, "Fabrication and characterization of 4-T/203 mm RT bore 2G HTS magnet with no-insulation method," *IEEE Transactions on Applied Superconductivity,* vol. 24, no. 3, pp. 1-4, 2014.

[127] Y. Wang *et al.*, "No-insulation high temperature superconductor winding technique for electrical aircraft propulsion," *IEEE Transactions on Transportation Electrification,* 2020.

[128] Y. Wang, H. Song, W. Yuan, Z. Jin, and Z. Hong, "Ramping turn-to-turn loss and magnetization loss of a No-Insulation (RE) Ba2Cu3Ox high temperature superconductor pancake coil," *Journal of Applied Physics,* vol. 121, no. 11, p. 113903, 2017.

[129] F. Gömöry, M. Vojenčiak, E. Pardo, M. Solovyov, and J. Šouc, "AC losses in coated conductors," *Superconductor Science & Technology,* vol. 23, no. 3, p. 034012, 2010.

[130] J. Šouc, E. Pardo, M. Vojenčiak, and F. Gömöry, "Theoretical and experimental study of AC loss in high temperature superconductor single pancake coils," *Superconductor Science & Technology,* vol. 22, no. 1, p. 015006, 2008.

[131] F. Grilli and S. P. Ashworth, "Measuring transport AC losses in YBCO-coated conductor coils," *Superconductor Science & Technology,* vol. 20, no. 8, p. 794, 2007.

[132] Y. Wang, M. Zhang, F. Grilli, Z. Zhu, and W. Yuan, "Study of the magnetization loss of CORC® cables using a 3D T-A formulation," *Superconductor Science & Technology,* vol. 32, 2019.

[133] X. Pei, A. C. Smith, X. Zeng, M. Husband, and M. Rindfleisch, "Design, build and test of an AC coil using MgB2 wire for use in a superconducting machine," *IEEE Transactions on Applied Superconductivity,* vol. 23, pp. –, 2013.

[134] Y. Yang, E. Martinez, and W. Norris, "Configuration and calibration of pickup coils for measurement of ac loss in long superconductors," *Journal of applied physics,* vol. 96, no. 4, pp. 2141-2149, 2004.

[135] M. Majoros *et al.*, "AC magnetization loss of a YBCO coated conductor measured using three different techniques," *IEEE Transactions on Applied Superconductivity,* vol. 21, no. 3, pp. 3293-3296, 2011.

[136] Z. Hong, W. Yuan, M. Ainslie, Y. Yan, R. Pei, and T. Coombs, "AC losses of superconducting racetrack coil in various magnetic conditions," *IEEE Transactions on Applied Superconductivity,* vol. 21, pp. 2466-9, 2010.

[137] M. Zhang *et al.*, "AC loss measurements for 2G HTS racetrack coils with heat-shrink tube insulation," *IEEE Transactions on Applied Superconductivity,* vol. 24, no. 3, pp. 1-4, 2014.

[138] E. Pardo, "Calculation of AC loss in coated conductor coils with a large number of turns," *Superconductor Science & Technology,* vol. 26, no. 10, p. 105017, 2013.

[139] J. Šouc, F. Gömöry, and M. Vojenčiak, "Calibration free method for measurement of the AC magnetization loss," *Superconductor Science & Technology,* vol. 18, no. 5, p. 592, 2005.

[140] J. Patel, "Design, Build & Test of an HTS Machine AC Loss Measurement Platform: Aircraft Applications," University of Bath, 2019.

[141] J.-B. Song, S. Hahn, T. Lecrevisse, J. Voccio, J. Bascunan, and Y. Iwasa, "Over-current quench test and self-protecting behavior of a 7 T/78 mm multi-width no-insulation REBCO magnet at 4.2 K," *Superconductor Science & Technology,* vol. 28, no. 11, Nov 2015, Art. no. 114001.

[142] W. D. Markiewicz, J. J. Jaroszynski, D. V. Abraimov, R. E. Joyner, and A. Khan, "Quench analysis of pancake wound REBCO coils with low resistance between turns," *Superconductor Science & Technology,* vol. 29, no. 2, pp. 25001-25001, Feb 2016, Art. no. 025001.

[143] T. M. Qu, P. C. Michael, J. Voccio, J. Bascunan, S. Hahn, and Y. Iwasa, "Persistent-current switch for pancake coils of rare earth-barium-copper-oxide high-temperature superconductor: Design and test results of a double-pancake

coil operated in liquid nitrogen (77-65 K) and in solid nitrogen (60-57 K)," *Applied Physics Letters,* vol. 109, no. 8, Aug 2016, Art. no. 082601.

[144] M. Furuse, M. Yoshikawa, Y. Itoh, S. Fukui, and T. Nakamura, "Fabrication and Testing of Racetrack-Shaped Double-Pancake Coil for Stator Windings of Induction-Synchronous Motor," *IEEE Transactions on Applied Superconductivity,* vol. 25, no. 3, pp. 1-4, 2015.

[145] H. Moon, Y.-C. Kim, H.-J. Park, I.-K. Yu, and M. Park, "An introduction to the design and fabrication progress of a megawatt class 2G HTS motor for the ship propulsion application," *Superconductor Science and Technology,* vol. 29, no. 3, p. 034009, 2016.

[146] Y. Wang, H. Song, D. Xu, Z. Li, Z. Jin, and Z. Hong, "An equivalent circuit grid model for no-insulation HTS pancake coils," *Superconductor Science and Technology,* vol. 28, no. 4, p. 045017, 2015.

[147] Y. Wang, H. Bai, J. Li, M. Zhang, and W. Yuan, "Electromagnetic modelling using TA formulation for high-temperature superconductor (RE) Ba2Cu3O x high field magnets," *High Voltage,* vol. 5, no. 2, pp. 218-226, 2020.

[148] H. L. Quach *et al.*, "Analysis on Electrical and Thermal Characteristics of a No–Insulation HTS Coil Considering Heat Generation in Steady and Transient States," *IEEE Transactions on Applied Superconductivity,* vol. 29, no. 5, pp. 1-6, 2019.

[149] S. Noguchi, R. Itoh, S. Hahn, and Y. Iwasa, "Numerical Simulation of Superconducting Coil Wound With No-Insulation NbTi Wire," *Ieee Transactions on Applied Superconductivity,* vol. 24, no. 3, Jun 2014, Art. no. 4900504.

[150] D. Liu, W. Zhang, H. Yong, and Y. Zhou, "Numerical analysis of thermal stability and mechanical response in a no-insulation high-temperature superconducting layer-wound coil," *Superconductor Science and Technology,* vol. 32, no. 4, p. 044001, 2019/02/15 2019.

[151] Y. Wang and H. Song, "Influence of turn-to-turn resistivity and coil geometrical size on charging characteristics of no-electrical-insulation REBCO pancake coils," *Superconductor Science and Technology,* vol. 29, no. 7, p. 075006, 2016.

[152] M. Bonura, C. Barth, A. Joudrier, J. F. Troitino, A. Fête, and C. Senatore, "Systematic Study of the Contact Resistance Between REBCO Tapes: Pressure Dependence in the Case of No-Insulation, Metal Co-Winding and Metal-Insulation," *IEEE Transactions on Applied Superconductivity,* vol. 29, no. 5, pp. 1-5, 2019.

[153] M. Sohn, K. Sim, B. Eom, H. Ha, H. Kim, and K. Seong, "Controllability of the Contact Resistance of 2G HTS Coil With Metal Insulation," *IEEE Transactions on Applied Superconductivity,* vol. 28, no. 3, pp. 1-5, 2018.

[154] L. Jun, G. Robert, H. Ke, and H. Seungyong, "Contact resistance between two REBCO tapes under load and load cycles," *Superconductor Science and Technology,* vol. 30, no. 4, p. 045005, 2017.

[155] Y. Wang *et al.*, "Analysis and Comparison Between No-Insulation and Metallic Insulation REBCO Magnet for the Engineering Design of a 1-MW DC Induction Heater," *IEEE Transactions on Applied Superconductivity,* vol. 27, no. 4, pp. 1-5, 2017.

[156] M. Zhang *et al.*, "AC loss estimation of HTS armature windings for electric machines," *IEEE Transactions on Applied Superconductivity,* vol. 23, no. 3, pp. 5900604-5900604, 2013.

[157] M. Zhang, F. Eastham, and W. Yuan, "Design and modeling of 2G HTS armature winding for electric aircraft propulsion applications," *IEEE Transactions on Applied Superconductivity,* vol. 26, no. 3, pp. 1-5, 2016.

[158] P. Ghoshal, T. Coombs, and A. Campbell, "Calorimetric method of ac loss measurement in a rotating magnetic field," *Review of Scientific Instruments,* vol. 81, no. 7, p. 074702, 2010.

[159] J. Eikelboom, "Apparatus for calorimetric measurement of ac losses in superconductors," *Cryogenics,* vol. 31, no. 5, pp. 363-365, 1991.

[160] F. Weng, M. Zhang, T. Lan, Y. Wang, and W. Yuan, "Fully superconducting machine for electric aircraft propulsion: study of AC loss for HTS stator," *Superconductor Science and Technology,* vol. 33, no. 10, p. 104002, 2020 2020.

[161] M. D. Ainslie, W. Yuan, Z. Hong, R. Pei, T. J. Flack, and T. A. Coombs, "Modeling and electrical measurement of transport AC loss in HTS-based superconducting coils for electric machines," *IEEE Transactions on Applied Superconductivity,* vol. 21, pp. 3265-8, 2010.

[162] A. B. Abrahamsen *et al.*, "Superconducting wind turbine generators," *Superconductor Science and Technology,* vol. 23, no. 3, p. 034019, 2010.

[163] X. Song, N. Mijatovic, B. B. Jensen, and J. Holboll, "Design study of fully superconducting wind turbine generators," *IEEE Transactions on Applied Superconductivity,* vol. 25, 2015.

[164] N. Long *et al.*, "Narrow strand YBCO Roebel cable for lowered AC loss," in *Journal of Physics: Conference Series*, 2008, vol. 97, no. 1, p. 012280: IOP Publishing.

[165] W. Goldacker *et al.*, "Status of high transport current ROEBEL assembled coated conductor cables," *Superconductor Science and Technology,* vol. 22, no. 3, p. 034003, 2009.

[166] S. Terzieva *et al.*, "Investigation of the effect of striated strands on the AC losses of 2G Roebel cables," *Superconductor Science and Technology,* vol. 24, no. 4, p. 045001, 2011.

[167] Z. Li *et al.*, "Evaluation of electrical and mechanical characteristics for a twisted soldered-stacked-square (3S) HTS wire with 1 mm width," *IEEE Transactions on Applied Superconductivity,* vol. 28, no. 3, pp. 1-5, 2018.

[168] J. Miller, D. Santosusso, M. Uva, K. Woods, and B. Fitzpatrick, "Naval superconducting integrated power system (sips)," in *Proceedings of the 10th Intelligent Ship Symposium, Philadelphia, Pennsylvania*, 2013, pp. 22-23.

[169] L. Graber *et al.*, "Cryogenic power electronics at megawatt-scale using a new type of press-pack IGBT," in *IOP Conference Series: Materials Science and Engineering*, 2017, vol. 279, no. 1, p. 012011: IOP Publishing.

[170] K. Rajashekara and B. Akin, "A review of cryogenic power electronics-status and applications," in *2013 International Electric Machines and Drives Conference*, 2013, pp. 899-904: IEEE.

[171] P. Haldar *et al.*, "Improving performance of cryogenic power electronics," *IEEE Transactions on Applied Superconductivity,* vol. 15, no. 2, pp. 2370-2375, 2005.

[172] P. J. Masson and C. A. Luongo, "HTS machines for applications in all-electric aircraft," in *2007 IEEE Power Engineering Society General Meeting*, 2007, pp. 1-6: IEEE.

[173] S. Venuturumilli, F. Berg, L. Prisse, M. Zhang, and W. Yuan, "DC line to line short-circuit fault management in a turbo-electric aircraft propulsion system using superconducting devices," *IEEE Transactions on Applied Superconductivity,* vol. 29, no. 5, pp. 1-6, 2019.

[174] N. Magnusson, S. Hörnfeldt, J. Rabbers, B. ten Haken, and H. H. ten Kate, "Comparison between calorimetric and electromagnetic total ac loss measurement results on a BSCCO/Ag tape," *Superconductor Science & Technology,* vol. 13, no. 3, p. 291, 2000.

[175] N. Magnusson, N. Schönborg, A. Wolfbrandt, and S. Hörnfeldt, "Improved experimental set-up for calorimetric AC loss measurements on HTSs carrying transport currents in applied magnetic fields at variable temperatures," *Physica C: Superconductivity,* vol. 354, no. 1-4, pp. 197-201, 2001.